



Abdul Rahman, Muhammad Ghazali (2017) *1D photonic crystal nanocavities for optical sensing*. PhD thesis.

<http://theses.gla.ac.uk/8288/>

Copyright and moral rights for this work are retained by the author

A copy can be downloaded for personal non-commercial research or study, without prior permission or charge

This work cannot be reproduced or quoted extensively from without first obtaining permission in writing from the author

The content must not be changed in any way or sold commercially in any format or medium without the formal permission of the author

When referring to this work, full bibliographic details including the author, title, awarding institution and date of the thesis must be given

Enlighten:Theses  
<http://theses.gla.ac.uk/>  
theses@gla.ac.uk



# University of Glasgow

## **1D Photonic Crystal Nanocavities for Optical Sensing**

**Muhammad Ghazali Abdul Rahman**

This thesis is submitted in fulfilment of the requirement for  
The Degree of Doctor of Philosophy (PhD)

School of Engineering  
College of Science and Engineering  
University of Glasgow

## **Author Declaration**

“I declare that, except where explicit reference is made to the contribution of others, that this dissertation is the result of my own work and has not been submitted for any other degree at the University of Glasgow or any other institution”.

Signature: \_\_\_\_\_

Name: MUHAMMAD GHAZALI ABDUL RAHMAN

## Abstract

The ability to detect small refractive index changes in analytes is of uttermost importance since these index changes can be directly correlated to the presence of small amounts of chemicals of interest within analytes. Photonic devices such as 1D PhC nanocavities are one of the interesting structures to be used as optical sensors due to their capability to integrate with CMOS technology. We present in this study, a simple optical technique of detection based on 1D PhC nanocavities that gives good sensitivity for various types of chemicals. The work reported in this thesis concerned with the designed, fabrication, and characterisation of 1D PhC nanocavity devices based on silicon-on-insulator (SOI) material. The objective of this work is to provide an optical wave-guided sensing technology using 1D PhC nanocavity devices in the wavelengths region around 1550 nm. Firstly, the PhC nanocavities were designed and modelled using 2D and 3D Finite-difference time-domain (FDTD) computations to provide insight behaviour of the resonator waveguides. The designated PhC nanocavity devices were carefully fabricated via combination of electron beam lithography (EBL) and the dry and wet etching technology. The nanocavity devices were realised using optimised fabrication process to ensure the sensing chips are reproducible and reliable. This is done by careful control at nanometre scale of fabrication process of the PhC nanocavity devices and the microfluidic chip. Then, the devices were paired with the PDMS based microfluidic channel system. The nanocavity devices were characterised and the sensor system were tested for their optical sensing capabilities. The sensitivity of various Q factor values corresponds to the different cavity lengths are studied. The sensor system sensitivity,  $S$  were measured via refractive index sensing experiment varying from 135.78 to 245.72 nmRIU<sup>1</sup> with the detection limit,  $DL$  of  $8 \times 10^{-6}$  RIU. The sensing area estimated is  $2.35 \mu\text{m}^2$ . In addition, through the non-specific interaction experiment, bio molecular proteins BSA as low as 3.125  $\mu\text{g/ml}$  concentrations were detected. Finally, the sensor system thermal responses were measured.

## Acknowledgment

First and foremost, I would like to thank my supervisor, Dr Nigel Johnson for his guidance and patience throughout these years. I would also like to thank my co-supervisor, Dr Philippe Velha for his tremendous support since the beginning of the research.

Many thanks to my former supervisor, Prof Richard De La Rue for accepting me as his student. His advice and understanding are invaluable. Special gratitude goes to Dr Graham Sharp, Dr Michael Strain and Dr Basudev Lahiri for the scientific discussions.

This thesis would not be possible without the collaborative input of so many people. I would like to thank Dr Mohd Faizal Ghazali for providing and preparing the BSA protein concentrations, James Watt Nanofabrication Centre (JWNC) staffs, Mr. William aka. Bill Ward and the Optoelectronics Research Group staffs and students, both past and present, for the memorable experience, for sharing their ideas and for providing help during the project.

Last but not least, to my beloved wife, Dr Noor Akmar Nam, son, Amir Muqree, and daughters, Alya Mufeeda and Aysha Madeeha who have been my everlasting joy, providing emotional support and tolerating the hectic PhD student life, but most importantly, being there when I needed them the most.

This study was funded by Majlis Amanah Rakyat (MARA), Malaysia and Academic Staff Training Scheme from the University of Kuala Lumpur, Malaysia.

# Table of Contents

Abstract .....	i
Acknowledgment .....	ii
Table of Contents .....	iii
List of Publications .....	vii
List of Tables .....	viii
List of Figures .....	ix
Abbreviations .....	xiii
<b>Chapter 1: Introduction .....</b>	<b>1</b>
1.1 Introduction .....	2
1.2 Background & Motivation .....	2
1.2.1 Concepts of Photonic Crystal.....	6
1.2.2 Aims and Objectives .....	11
1.3 Merits of this work.....	12
1.4 Thesis Outline .....	12
References.....	14
<b>Chapter 2: Modelling of Photonic Structures .....</b>	<b>20</b>
2.1 Introduction .....	21
2.2 Photonic Modelling Method .....	21
2.3 The Finite-Difference Time-Domain Method (FDTD) .....	23
2.4 Lumerical FDTD.....	24
2.4.1 Sources and Boundary condition .....	24
2.4.2 Mesh Condition.....	25
2.5 Method of Extracting Quality Factor .....	26
2.6 Modelling 1-D PhC Nanocavities .....	29
2.7 Conclusions.....	32
References.....	33

<b>Chapter 3: Fabrication Process .....</b>	35
3.1 Introduction.....	36
3.2 Silicon-On-Insulator (SOI) Platform .....	36
3.3 Overview of the process flow .....	37
3.4 Wafer chip preparation .....	38
3.5 Device Patterning.....	39
3.5.1 Alignment Markers .....	40
3.5.2 Waveguide definition.....	42
3.5.2.1 CAD Layout .....	43
3.5.2.2 Fracturing & Proximity Effect Correction .....	44
3.5.2.3 E-beam Resist, EBL Exposure, Development .....	45
3.5.2.4 Silicon Dry Etching.....	48
3.5.3 Silicon Membrane.....	50
3.6 Waveguide Coupling .....	52
3.6.1 Adiabatically tapered coupling method .....	52
3.6.2 Planar inverted tapers with low index polymer block coupling method .....	53
3.7 Overall device design.....	56
3.8 Conclusions.....	58
References.....	59
<b>Chapter 4 Photonic Crystal Nanocavities.....</b>	62
4.1 Introduction.....	63
4.2 Photonic Crystal Nanocavities .....	63
4.3 The Design .....	64
4.3.1 Period and Cavity.....	66
4.3.2 Mode matching and optimization .....	67
4.3.3 Initial Results .....	68
4.4 1-D PhC nanocavities working at 1550 nm .....	71
4.4.1 Cavity length arrangement.....	72
4.4.2 Mirror strength .....	74
4.5 1-D PhC nanocavities membrane.....	75
4.6 Conclusions.....	77
References.....	78

<b>Chapter 5: Microfluidic Channel System .....</b>	82
5.1 Introduction.....	83
5.2 Optical sensing system.....	83
5.3 PDMS Microfluidic Channel System .....	84
5.3.1 Introduction.....	84
5.3.2 Fabrication of Microfluidic Channel .....	85
5.3.2.1 PDMS Master Mould .....	85
5.3.2.2 PDMS Microfluidic Channel Chip.....	87
5.4 Characterisation and System Setup.....	89
5.4.1 System Setup for Optical Sensing.....	92
5.5 Conclusions.....	94
References.....	95
<b>Chapter 6: Optical Guided-Wave Sensing .....</b>	97
6.1 Introduction.....	98
6.2 Optical Sensing Experiments .....	98
6.2.1 Introduction.....	98
6.3.2 Material & Method .....	98
6.3.3 Evaluating aqueous flow rate stability in the system.....	100
6.3.3.1 Results and Discussion.....	100
6.3.4 Reusability of the Sensor System .....	102
6.3.4.1 Results and Discussion .....	102
6.3.5 Refractive index sensing .....	104
6.3.5.1 Results and Discussion .....	105
6.3.6 Glucose Concentration Sensing Array.....	106
6.3.6.1 Results and Discussion .....	106
6.3.7 Protein BSA Sensing.....	109
6.3.7.1 Results & Discussion .....	110
6.3 Temperature dependence .....	111
6.3.1 Results and Discussion .....	112
6.4 Conclusions.....	114
References.....	115

<b>Chapter 7: Conclusion and Future Work.....</b>	118
7.1 Introduction.....	119
7.2 Summary and Conclusion.....	119
7.3 Future Work .....	121
References.....	123
Appendix .....	124

## List of Publications

M. Ghazali A. Rahman, P. Velha, Richard M. De La Rue, Nigel P. Johnson. "1-D Photonic Wire Microcavities for Refractive Index Sensing", EOS Topical Meeting on Micro- and Nano-Optoelectronic Systems, Bremen December 2011 (Best Student Presentation Award)

Johnson, Nigel P., Basudev Lahiri, Graham Sharp, Ghazali A. Rahman, Philippe Velha, Ali Khokhar, M. Richard, and Scott McMeekin. "Photonic sensors at the nanoscale." In *2012 14th International Conference on Transparent Optical Networks (ICTON)*, pp. 1-4. IEEE, 2012.

Rahman, M. Ghazali A., Philippe Velha, M. Richard, and Nigel P. Johnson. "Silicon-on-insulator (SOI) nanobeam optical cavities for refractive index based sensing." In *SPIE Photonics Europe*, pp. 84391Q-84391Q. International Society for Optics and Photonics, 2012.

Rahman, M. Ghazali A., Philippe Velha, M. Richard, and Nigel P. Johnson. "High-Q optical nanobeam cavities for label-free sensing." In *Proc. of SPIE Vol*, vol. 8774, pp. 87740G-1. 2013.

Rahman, M. Ghazali A., Philippe Velha, M. Richard, and Nigel P. Johnson. "Progress in high Q optical nanobeam cavities for label-free sensing." In *2015 17th International Conference on Transparent Optical Networks (ICTON)*, pp. 1-3. IEEE, 2015.

## List of Tables

Table 1.1: Comparison between configuration devices based on SOI material

Table 1.2: Commercially available integrated optics biosensors.

Table 3.1: Table presents the characteristics of negative tone e-beam resist of NEB 31 and HSQ.

Table 3.2: Parameters of silicon waveguide dry etch process using RIE ICP machine.

Table 3.3: Table shows the advantages and disadvantages of using SU-8 as polymer waveguides feed into and out of the device.

Table 6.1: Comparison with other type of devices for BSA protein detection.

Table 6.2: Absolute measurement data of resonance wavelengths correspond to different temperature medium.

## List of Figures

Figure 1.1: Basic transducer elements

Figure 1.2: The figures illustrate the simplest form of (a) one, (b) two, and (c) three-dimensional PhCs; while (d), (e) and (f) are the micrographs of their fabricated version of PhCs respectively.

Figure 1.3: Illustrate the 2D (top) and 1D PhC (bottom) waveguides.

Figure 1.4. Figures are the micrographs pictures of (a) L3 2D PhCs and (b) H1 2D PhCs.

Figure 1.5. Figure shows form of 1D PhC cavity with Bragg mirror in both sides.

Figure 2.1 Yee algorithm configurations

Figure 2.2: Diagram representing GUI of integrated mode solver used to find the range of frequencies to be excited into the structures

Figure 2.3: Picture illustrating the ‘staircasing’ approaches (a) a circle structures in grid resolution (b) and (c) depicts the circular shape in big and small resolution grid to accommodate the circle structures.

Figure 2.4: Graph describes the Q relation to its bandwidth.

Figure 2.5: Graph depicts the time decay of the E and H-field with their envelopes.

Figure 2.6: GUI of mode solver program to calculate the effective index approximation of PhC waveguide.

Figure 2.7: Result of the vertical distribution of TE mode in 0.22  $\mu\text{m}$  thick of the PhC waveguide from the mode solver approximation program. The x-direction represents the vertical cut through the PhC waveguide.

Figure 2.8: Picture illustrates the association between PhC waveguide period, A and the integer number of resolution grid. For example, each periods are divided into 6 x 6 cells.

Figure 3.1: Smart-Cut technology process for SOI fabrication from SOITEC [3.5].

Figure 3.2: Summarized process flow of the fabrication process of PhC nanocavities. (a), (b) and (c) are fabrication steps in order.

Figure 3.3: Schematic diagrams of positive and negative tone resist behaviour after development process.

Figure 3.4: Schematic diagram of 20 x 20 mm wafer chip with the alignment markers and the pattern area

Figure 3.5: Process flow for fabrication of alignment markers.

Figure 3.6: Process flows of pattern definition when using EBL.

Figure 3.7: Illustrate the relationship between beam spot size (BSS), resolution and spot size (SS).

Figure 3.8: Schematic illustrates the cross section of the resist and substrate during EBL process. ‘ $r$ ’ is the lateral distance that secondary electrons have scattered through the resist and the substrate.

Figure 3.9: HSQ structure

Figure 3.10: SEM pictures of a waveguide with stitching error in the horizontal direction (a) and combination of vertical and horizontal direction (b) during EBL writing.

Figure 3.11 SEM pictures of over etched silicon waveguide damages the resist mask and over-etches to the silica layer, however the surface roughness of the sidewall is smooth and acceptable (a), while (b) shows fully etched Bragg mirror holes in the silicon waveguide.

Figure 3.12: Optical micrograph of PMMA window mask (dark rectangles) on the chip for membrane definition.

Figure 3.13: SEM pictures of etched silica beneath the waveguide device. (a) Birds eye view and (b) shown from the end of the suspended waveguide.

Figure 3.14: Schematic design of coupling feeder and device waveguides.

Figure 3.15: Graph shows transmission spectrums versus wavelengths of SU-8 resist from 350 to 800 nm (visible light range) and 1200 to 1600 (mid infra red). [3.18]

Figure 3.16: Schematic of the waveguide with SU-8 polymer block for input and output coupling. The waveguide device was depicted in red and is planar inverse tapered down to a narrow tip. A transparent block of SU-8 polymer covered the input and output waveguides.

Figure 3.17: Optical micrographs of HSQ pattern after development with (a) and without (b) oxygen plasma ashing surface modification. Without the surface modification, HSQ suffers serious adhesion problem towards the end of the tip (c) SEM micrograph of silicon end tip after dry etching.

Figure 3.18: SEM pictures of the fabricated silicon waveguide.

Figure 3.19: Picture illustrated the design of complete feeder and device waveguide.

Figure 4.1: Images illustrating (a) light scattering loss inside the waveguide cavity region resulting in the poor Q factors while (b) less scattering effects when tapering mirrors holes were added inside the cavity. The light blue arrows show the light propagation directions.

Figure 4.2: Basic design of 1D PhC cavity structure consists of periodic mirrors

separated by a cavity.

Figure 4.3: 2D FDTD computations of pass and stop bands (a) varying the period length on the middle of the Bragg mirrors (b) Bandgap of 6 period Bragg mirrors ( $N = 6$ ) with various period length.

Figure 4.4: The tapering technique, (a) First tapering holes inside the cavity (b) 2D FDTD computed results of Q values of single tapering holes inside the cavity with various tapering hole displacement.

Figure 4.5: 2D FDTD computed results of Q values of 1D PhC nanocavity from single to four aperiodic tapering holes inside with various displacements. The cavity length was adjusted to suit the targeted location at  $1310\text{ nm}$ .

Figure 4.6: Computed 2D FDTD results show (a) significant increase of Q factor values when additional Bragg mirrors were added (5NT4 and 6NT4 are 5 and 6 Bragg mirrors with 4 tapering holes). 4N, 4NT1, 4NT2, 4NT3 and 4NT4 indicate 4 Bragg mirrors, 4 Bragg mirrors with 1,2,3 and 4 aperiodic tapering holes respectively. (b) Graph shows transmission spectrum is drastically decreased when additional mirror holes were introduced.

Figure 4.7: The measured transmission spectrum of device working at  $1330\text{ nm}$ . The transmission intensity was normalised to the unpatterned optical waveguide.

Figure 4.8: SEM micrograph of the fabricated device targeted working at  $1550\text{ nm}$  range.

Figure 4.9: Experimentally measured transmission spectra of PhC nanocavity devices for  $N = 2$  with different cavity lengths varying from  $390$  to  $550\text{ nm}$ .

Figure 4.10: Q factors and resonance wavelengths location for various cavity lengths from  $430$  to  $510\text{ nm}$ . The Q factor is estimated by a Lorentzian fitting of the peaks at the resonance wavelengths.

Figure 4.11: The  $Q$  of the measured devices corresponds with the specific cavity lengths ( $450$ ,  $470$  and  $490\text{ nm}$ ) for a given  $N$ .

Figure 4.12: Experimental results showing comparison of the PhC membrane with the non-suspended (Silica clad) PhC nanocavity. (a) Shifts of the resonant wavelengths peaks towards the shorter wavelengths when silica was removed and (b) Q factor comparison between the two devices.

Figure 5.1: Specification of PDMS microfluidic channel

Figure 5.2: Figure illustrating the simplified steps in the fabrication of the PDMS microfluidic channel system, (a)–(d) UV photolithography in SU-8, (e)–(f) PDMS casting and bonding.

Figure 5.3: Illustration of PDMS microfluidic channel attached to the PhC nanocavity devices chip. The diagram is not to scale.

Figure 5.4: Experimental setup used for characterisation of the fabricated devices. The blue square relates to the 40 X magnification lenses, sample and fibre tip in plane on the micro-positioner.

Figure 5.5: Optical response of transmission spectra (a) unpattern waveguides and (b) resonance wavelengths of PhC nanocavity device with the specification of  $N = 2$  and  $c = 470 \text{ nm}$ .

Figure 5.6: Schematic diagram of the partial experimental setup for the sensing applications incorporate with the microfluidic system.

Figure 5.7: Image of the actual experimental setup arrangement on the micro-positioner stage.

Figure 6.1: The sensor system setup arrangement for optical sensing experiments

Figure 6.2: The resonance wavelengths shifts with different flow rates continuously flowing through the sensor system

Figure 6.3: The resonance wavelengths peaks ( $\text{nm}$ ) according to the time ( $s$ ) at the continuous flow of DI water-Glucose concentration-DI water experiment.

Figure 6.4: Spectral transmission of resonance wavelength shifts from (a) DI water to glucose concentration solution (red shifts) and from (b) Glucose concentration solution to DI water (blue shifts).

Figure 6.5: Resonance wavelength peak shifts of DI water, Methanol and IPA.

Figure 6.6: Resonance wavelengths of glucose concentration solution at 0, 10 and 15 % correspond with various cavity lengths,  $c$ .

Figure 6.7: Q factor of 0 % of glucose concentration and resonance wavelengths shift from 0 to 10 % of glucose concentration solutions according to various cavity lengths,

Figure 6.8: Q factor of 10 % of glucose concentration and resonance wavelengths shift from 10 to 15 % of glucose concentration solutions according to various cavity lengths,

Figure 6.9: Resonance shift versus BSA concentrations

Figure 6.10: Resonance wavelengths response with different temperature medium.

Figure 7.1: Fabricated slotted 2D (left) and 1D (right) PhC nanocavities.

## Abbreviations

PhC	Photonic Crystal
SPR	Surface Plasmon Resonance
TIR	Total Internal Reflection
MRR	Micro Ring Resonator
MMI	Multimode Interference
MZI	Mach-Zehnder interferometer
PBG	photonic bandgap
1D, 2D, 3D	One-Dimensional, Two-Dimensional, Three-Dimensional
VCSELs	vertical cavity surface emitting lasers
Q	Quality factor
FWHM	full-width-half-maximum
SOI	Silicon-On-Insulator
FDTD	Finite-Difference Time-Domain
EBL	electron beam lithography
RIE	reactive ion etching
HF	Hydrofluoric acid
RAM	random access memory
FEM	Finite Element Method
MoM	Method of Moment
CW	Continuous Wave
GUI	graphic user interface
PML	Perfectly Matched Layer
CMT	conformal mesh technique
CMOS	Complementary metal–oxide–semiconductor
IPA	isopropyl alcohol
JWNC	James Watt Nanofabrication Centre
MA 6	SUSS Microtec Mask Aligner 6
VB 6	Leica Vector Beam 6
PMMA	Polymethyl methacrylate
MIBK	Methyl isobutyl ketone
TMAH	TetraMethyl Ammonium Hydroxide
HSQ	Hydrogen Silsesquioxane
GDSII	Graphic Database System II

RO	Reverse Osmosis
DI	De-ionized
SEM	Scanning Electron Microscope
FOS	fibre optic sensor
PDMS	Polydimethylsiloxane
PTFE	polytetrafluoroethylene
BSA	bovine serum albumin
PEG	poly (ethylene glycol)

# **Chapter 1: Introduction**

- 1.1 Introduction
  - 1.2 Background & Motivation
    - 1.2.1 Concepts of Photonic Crystal
    - 1.2.2 Aims and Objectives
  - 1.3 Merit of this work
  - 1.4 Outline of the thesis
- References

## 1.1 Introduction

This introduction provides a simplified history of photonic crystals and the time lines since the concept was first introduced. The section includes basic details of light confinement in slab waveguides and leads to the introduction of a photonic crystal. The basic principles of optical sensor using photonic crystals and other structures are also reviewed. The fundamental concepts and the uses of one and two-dimensional photonic crystal nanocavities are also discussed. Finally, the main contributions of this work are noted and the outline of the thesis content is given.

## 1.2 Background & Motivation

Over the last few decades, the control over material electrical properties has made many advances. Semiconductor technological breakthroughs have allowed us to better understand certain material behaviour via their electrical properties. This has led to the revolution of transistors and integrated circuits in electronics.

The massive technological development of electronics has enabled advances in optics or photonics. The optical properties of a material can be engineered to interact with light over desired frequencies. The light can be confined within a specific volume when it is perfectly reflected and allowing it to propagate in certain directions [1.1]. The breakthrough led to fibre-optic cables and later revolutionized the telecommunication industry. The innovation of optical fields includes laser engineering, spectroscopy and high speed computing.

The confinement of light and the control over the optical properties of materials on a chip are more difficult. Nevertheless, the concept of photonic crystal (PhC) where light propagates in a material with periodic refractive index has proven to be successful candidate. (The concept is given in Section 1.2.1). The most widely used material in electronics is silicon. The use of this material has crossed the boundaries into photonics, biology and chemistry.

In recent years, optical sensors have seen a enormous improvement because of the increasing demand of sensing applications in healthcare, defence, automotive, environment and many more. Although the electrical/electronics based sensors dominates the application market, optical or photonic domains for sensors has increased.

The optical sensor consists of transducer, the device that converts a signal in one form of energy to another form of energy. The transducer elements can either generate emission, phase or resonance shifts [1.2-1.4] optical absorption [1.5,1.6] or light scattering [1.7-1.9]. The optical sensor has many advantages over electrical/electronics based sensor. Optical sensor able to monitor the effective index of the analyte interaction and translates the modes to resonance wavelengths in real time; while, the electrical sensor in particular monitors the charges that interact with the surrounding medium. Moreover, optical sensor is immune to liquid and air environment. Furthermore, optical sensor provides low losses and are immune to the electrical and magnetic interference.

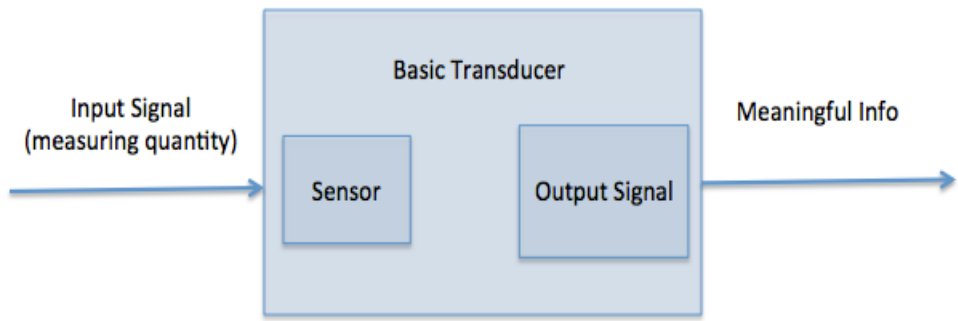


Figure 1.1: Basic transducer elements

There are several types of operating principles for optical sensors. The most common types of optical sensor are fibre optics [1.10-1.12], surface plasmon resonance (SPR) [1.13-1.15] and wave-guiding [1.16-1.19]. Fibre optic sensors are probed at the end of the tip. The tip acts as the sensing area and provides detection of the specific interaction of the medium. Another type of optical sensing operating principle commonly used is SPR. SPR measures the absorption of the material of interest onto planar metal (usually gold and silver) surfaces or onto the surface of metal

nanoparticles. Lastly, the wave-guiding operating principle provides promising concepts in optical sensors. Here the light is confined inside the waveguide by total internal reflection (TIR) with a medium surrounding the sensing area that has different refractive index. In general, the light is confined within the planar structures carries an evanescent field which exposed to surrounding medium. A crucial component is a cavity or other resonant structure, which changes frequency in response to the surrounding medium due to the evanescent field. The waveguides based sensors have greater potential to detect bulk refractive index change or specific bio or chemical analytes. This is because the waveguides sensor offers a greater degree of interaction with the sensing medium. The sensitivity of the devices depends on the interaction of evanescent field of the optical modes and the analyte. Furthermore, the waveguides based sensors are capable of being miniaturized into sub micrometre scale devices.

There are various configurations of fabricated waveguides formats for the optical sensors, for example micro ring resonator (MRR) [1.20-1.23], Multimode interference waveguide (MMI) [1.24,1.25] and Mach-Zehnder interferometer (MZI) [1.26-1.28]. In MRR, the light is confined inside the structure by TIR principle. The light then circulates inside the resonator structure either by ring or disk and is coupled to the output waveguide for detection. The longer the light is confined in the structures and interacts with the analyte, the more sensitive of the devices. The MMI consist of a section with a multi mode waveguide coupled with the single mode waveguides. The multimode waveguide is capable of multiplexing into a single mode waveguide to increase the sensitivity. The MZI is constructed with a single mode that splits into two waveguides to forms the reference and sensing arms. The reference arm is kept out of the analyte to provide a control waveguide while the sensing arm interacts with the analyte.

There are a few disadvantages of MRR, MMI and MZI structured devices in optical sensor configurations. One of them is the requirement of large footprint to interact with the analyte. For example, the MRR sensitivity will increase with a larger ring or disk and the MMI requires a longer dimensions of the multimode waveguide. The same case applies to the MZI, which requires longer sensing arms to increase sensitivity. However, there are many advantages of the waveguides based as an optical sensor. The larger footprints provide wider sensing area and enhance capability

for the multi layers or multiplexing of analyte detection. The ability of multiplexing of analyte detection can offer label-free bio sensing [1.28 - 1.29]. Therefore, more complex biological analyte detection is obtainable without any dyes or fluorescence labelling.

Another way to introduce single compact optical sensor is to integrate the waveguides with PhCs [1.17-1.18,1.30-1.31]. In this context, the PhC sensor have been widely investigated due to their potential of strong light confinement to a very small volume. This advanced feature enables PhC based sensors to detect nano metre scale of analyte [1.29]. Many arrangements of PhCs have been explored and proven to have high sensitivity i.e. 1D and 2D PhC micro cavity [1.30 - 1.31], slotted PhC [1.32 - 1.33] and PhC with PCF integration [1.34]. In all of the examples given, 1D PhC microcavities offers smallest footprint with high light confinement. These structures usually consist of Fabry-Perot geometry, with a cavity and PhC mirrors in a plane. The mirrors are typically in form of Bragg gratings consist of periodic structures in which refractive index varies.

Table 1.1 summarizes the comparison of the structures based on SOI waveguides for optical sensor. It also describes the device configurations and detection limit, *DL* of the sensor system. Although MRR is better in terms of detection limit, their foot print size are much larger than 1D PhC.

Device configuration	Detection Limit (RIU)	Device Structure
Micro Ring Resonator [1.35]	$2 \times 10^{-4}$	Slot
Micro Ring Resonator [1.36]	$8.3 \times 10^{-8}$	Planar
PhC [1.32]	$7 \times 10^{-6}$	Slot
PhC [this work]	$8 \times 10^{-6}$	Planar

Table 1.1: Comparison between configuration devices based on SOI material.

While the research is still flourish over the years, the small optical based sensors are already in the market to serve the demand. Table 1.2 shows the commercial solutions of biosensor available based on integrated optics.

---

Company	Technology	Website
Biacore [1.37]	Surface Plasmon Resonance	<a href="http://www.biacore.com">www.biacore.com</a>
Genalyte [1.38]	Micro Ring Resonator	<a href="http://www.genalyte.com">www.genalyte.com</a>
Axela [1.39]	Gratings	<a href="http://www.axelabiosensors.com">www.axelabiosensors.com</a>

Table 1.2: Commercially available integrated optics biosensors.

In this work, a detail review of 1D PhC nanocavities embedded in photonic wire waveguides is presented. The work is also describes the choice of materials, bio and chemical based sensing using microfluidic channels and their application in sensing. The motivations of this work are to design, fabricate and characterise the 1D PhC nanocavities based on SOI for the purpose of optical sensing.

### 1.2.1 Concepts of Photonic Crystal

As early in 1987, the first ideas of photonic crystal (PhC) material structures were introduced by Yablonovich [1.40] and John [1.41]. The idea covers the concepts behind the PhC design material structures. The PhCs material structures affect the properties of the photons in the similar behaviour to semiconductor affect the properties of electrons. The concept suggested that structures with periodic variations in dielectric constant might affect the photonic modes in a material.

In a semiconductor, the atomic lattice provides a periodic potential for the electrons to propagate through the electronics crystal. The potential creates a gap in the energy to forbid the electrons to propagate in any direction. In PhCs, the lattice periodicity variation in refractive index forms a photonic bandgap (PBG) in the crystal. For a full bandgap light is forbidden to propagate in any direction similar to carriers in a semiconductor. In PBG, the light propagation is prohibited and completely reflected inside the PhCs structure. The PBG is an important discovery that has led to various scientific engineering applications, i.e. the control of spontaneous emission [1.42], trapping of photons [1.43], and near zero-threshold lasing [1.44].

### *PhC basic forms (1D, 2D and 3D)*

PhCs can be generally divided into one-dimensional (1D), two-dimensional (2D) and three-dimension (3D) arrangements. In 1D PhCs, the light travels in periodic modulation of permittivity, which occurs only in one direction (i.e. x-direction). A good example of 1D PhC is Bragg gratings that are widely used in vertical cavity surface emitting lasers (VCSELs) [1.45]. While in 2D PhCs, the periodicity of the permittivity is along two directions with the third direction of the medium is uniform (i.e. x- and y-direction). In 3D PhCs, the permittivity modulation is along all three directions (i.e. x-, y- and z-directions). An example given for 1D, 2D and 3D PhCs are given in [1.46]. The ideas of the 3D PhCs were proposed by Yablonovich and John, promising to have an ultimate high Quality-Factors (Qs) and a complete photonic band gap. An example of a fabricated 3D PhCs structures are the ‘woodpile’ structure. Unfortunately, 3D PhCs structures are very challenging to fabricate.

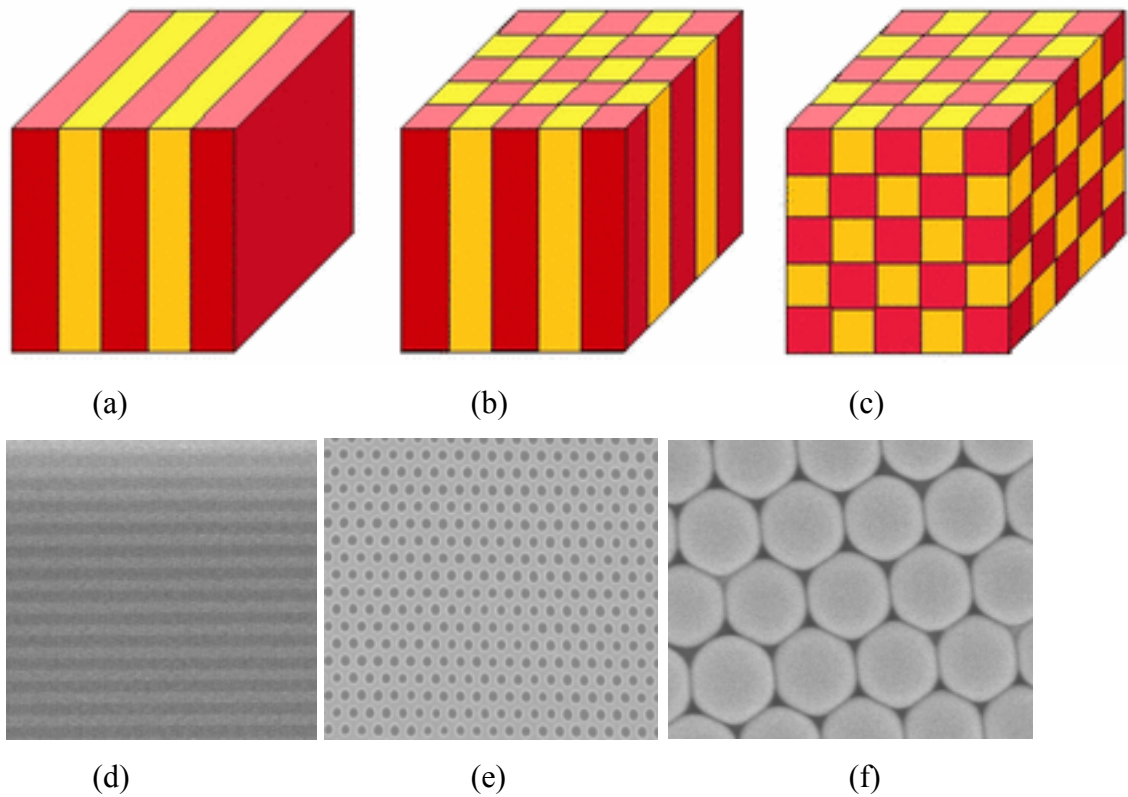


Figure 1.2: The figures illustrate the simplest form of (a) one, (b) two, and (c) three-dimensional PhCs; while (d), (e) and (f) are the micrographs of their fabricated version of PhCs respectively [1.46].

*Waveguides and Cavity in PhCs*

The most important optical functions in PhCs are guiding and trapping light using waveguides and resonant cavities. These functions enable ranges of all-optical devices to be made. Waveguide transferring light from one part of the circuit to another or even to other devices, similar to wires in electrical and electronics domains. Furthermore, the waveguides are mainly used in couplers, junctions and interferometers. In 2D PhCs, the removal of a line of periodic PhC structures creates waveguide. For 1D PhC vertical confinement solely depends on the Total Internal Reflection (TIR). TIR is explained in further in Section 4.3.1

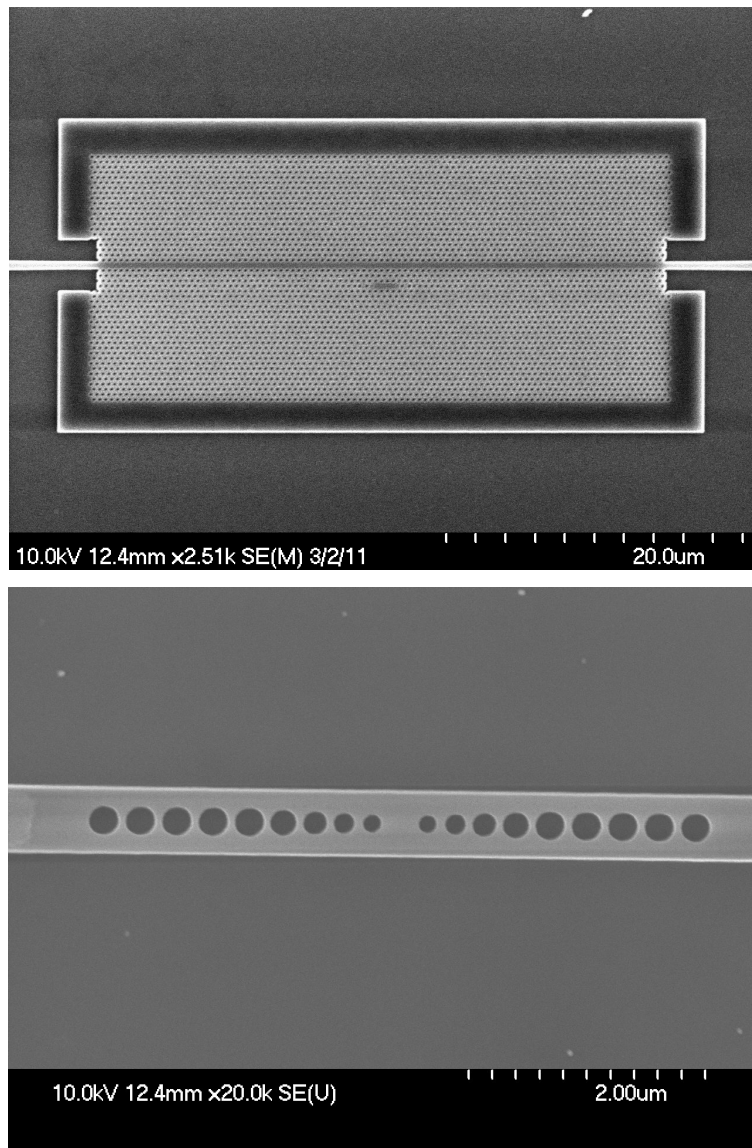


Figure 1.3: Illustrate the 2D (top) and 1D PhC (bottom) waveguides.

The key feature that has made PhCs significant is when a defect is introduced into photonic band gap structure and a cavity created. The cavity involves changing the dielectric constant in local region of the crystal and it is designed to trap light within the region [1.47]. In addition, the potential to store lights for many optical cycles make them advantageous for optical sensing and other photonic applications.

3D PhCs have the potential to trap light because of full band gap. The complexity of the lattice made it difficult to attain full 3D high ‘quality’ cavity. Generally, in order to create a 2D PhCs cavity, the simplest method is to remove a periodic pattern of PhCs. Usually, the strategy of removal of periodic pattern was used and named by number of missing holes or lines. In example, H1 cavity meaning 1 holes or if there is 3 holes removed and formed a line, the cavity is been named as an L3 cavity. The examples given are shown in Figure 1.4. The removal of a hole is designed to confine the travelling light at certain wavelengths within the photonic band gap. There are many other configurations in other to increase the 2D PhC cavity performance by modifying the holes radius, changing it to shape and sizes, or by removing it altogether. [1.48 – 1.49]

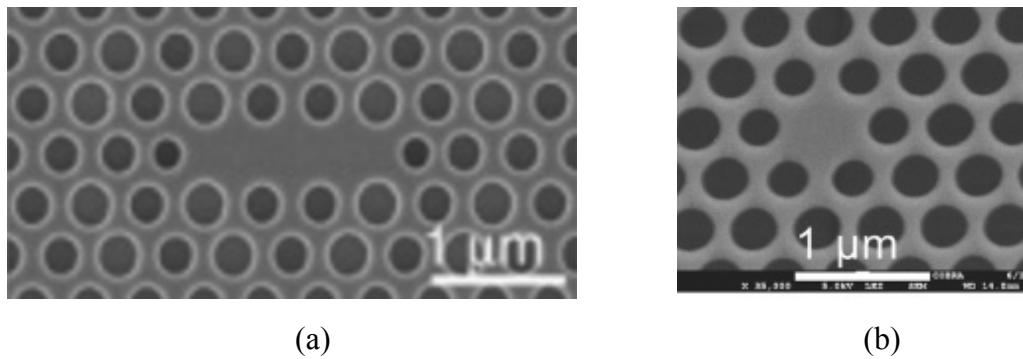


Figure 1.4. Figures are the micrographs pictures of (a) L3 2D PhCs [1.48] and (b) H1 2D PhCs [1.49].

For 1D PhCs, where the light is travelling in one direction, the cavity usually formed in the middle of the holes of the PBG structure. The configuration forms a Bragg mirrors at the ends of the cavity.

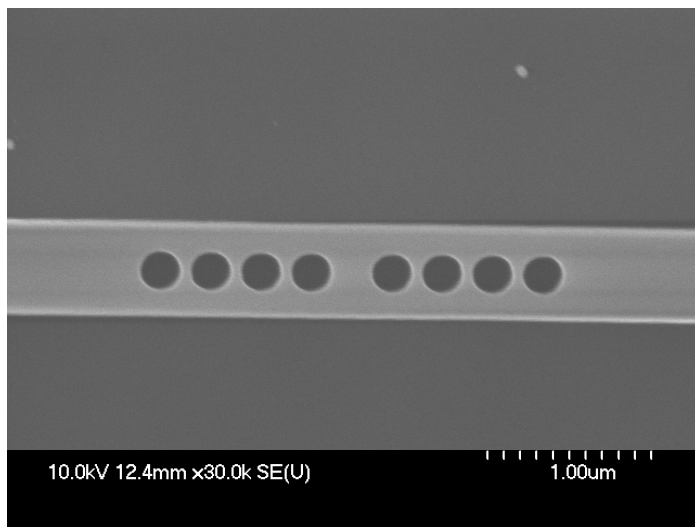


Figure 1.5. Figure shows form of 1D PhC cavity with Bragg mirror in both sides.

### *High Q<sub>s</sub> and its advantages*

The resonant behaviour of the PhC cavity or by means of other photonic devices are measured by their Quality Factors (Q<sub>s</sub>). Q is the ratio of the centre frequency intensity or resonant wavelengths to the full-width at half-maximum of the resonant peak confined within the PhC cavity. Q is dimensionless quality measurement used to characterise a resonator or PhC nanocavity. On the other hand, Q relates to the rate of loss of energy to the stored energy inside the resonator. Therefore, a high Q<sub>s</sub> PhCs nanocavities stores energy for longer period of time. The Q is proportional to the lifetime of the trapped light in the cavity;

$$Q = \omega_0 \frac{\text{stored energy}}{\text{power loss per cycle}}$$

(Eq. 1.1)

where  $\omega_0$  is the resonant frequency. An ideal PhC cavity will trap light forever and have infinite Q, however in reality, PhC cavity is limited by losses. The losses may come from the absorption and radiation of the material and the surroundings. The Q measurement in practical simulation and experimental PhC cavities structures, Q is proportional to the relative width of the resonant frequency in power spectrum;

---


$$Q = \frac{\omega_0}{\Delta\omega} \quad (\text{Eq. 1.2})$$

where  $\Delta\omega$  is the full-width-half-maximum (FWHM) of the resonant frequency power spectrum.

In 1D PhCs, the Qs rely on TIR for light confinement in vertical direction. Hence, their performance are dependant on out of plane losses. The total Q is contributions of in plane and out of plane effects of 1D PhCs;

$$\frac{1}{Q} = \frac{1}{Q \parallel} + \frac{1}{Q \perp} \quad (\text{Eq. 1.4})$$

where  $Q \parallel$  is in plane effects and  $Q \perp$  is out of plane effects. These effects depend on several factors. While the  $Q \parallel$  is depends on PhCs layer surrounding and scattering losses, the  $Q \perp$  is depends on out of plane radiation occurs when the light is reflected at the interfaces surrounding the cavity. [1.50]. Although the total Q factor values are limited by the smaller  $Q \parallel$  and  $Q \perp$ , the best PhCs optical sensors rely on the interface of analyte in the cavity region. Therefore, the  $Q \parallel$  must be kept small.

The high Q feature makes it ideal to use as an optical sensor. The trapped light is confined and cycled in the high Qs PhCs cavity. This phenomenon should enable the PhCs optical sensor to have more interaction with the analyte. During the light lifetime in the cavity, the light is bounces back and forth between the Bragg mirrors interface with the analyte.

## 1.2.2 Aims and Objectives

To summarize, the main objectives of the work for the project are to design, fabricate, characterize and utilize the 1D PhC nanocavities for optical bio and chemical sensors. 1D PhC nanocavities configuration explored includes 1D PhC nanocavities on silica and air cladding, and PhCs nanocavties membrane that have air-and-air cladding.

Given the advancement of silicon technology, and potential to integrate with the

CMOS environment, the transducer of the optical sensor devices were fabricated based on the Silicon-On-Insulator (SOI) material. Keeping it low cost, compact, photonic Lab-on-a-chip and fluidic integration design compatible, we used the PDMS material based to realize the microfluidic channel system. The plan is to use variation of glucose concentration solutions, different refractive index material, BSA concentration for biological elements sensing.

### 1.3 Merits of this work

The main contributions of the work described in this thesis are as follows;

- a) An analytically investigation in to the cavity behaviour for a 1D PhC using tapering inside and outside cavity in a standard  $220\text{ nm}$  thickness of silicon from Silicon-On-Insulator (SOI). Methods for obtaining high Q factor values on 1D PhC nanocavities have been suggested and explored.
- b) A systematic investigation in to the nanocavities behaviour at different cavity lengths to tune the resonance wavelengths.
- c) The study PhC nanocavities for bio-chemical sensing based on different refractive index of analytes is investigated.
- d) Bulk refractive index sensing methods are proposed to determine bio and chemical resonance wavelengths.

### 1.4 Thesis Outline

The introduction has covered the basic concept of PhC cavities. The important parameters have been introduced. In the latter chapter this thesis presents the progress of 1D PhC nanocavities based on SOI towards the application for optical sensing.

Chapter 2 (Modelling of Photonic Structures) discusses the fundamentals of the computational method used to investigate the photonic structures. This describes in

detail Finite-Difference Time-Domain (FDTD) approach and the parameters for the PhC nanocavity structures. In addition, method of extracting high Q factor of simulated resonances is discussed.

Chapter 3 (Fabrication Processes) presents fabrication process used to develop PhC nanocavity structures. The fabrication process includes global markers, waveguides, membrane and block polymer coupler patterning using Vistec VB6 electron beam lithography (EBL) tool. The patterns were defined by dry-etch using reactive ion etching (RIE) for the waveguide slab and wet chemical etch using Hydrofluoric acid (HF) for the membrane. Also, block polymer coupling method is discussed for further improve the coupling efficiency and to reduce high Fabry-Perot effects on the measurement.

Chapter 4 (Photonic Crystal Nanocavities) focus on the design of photonic crystal structure using the tapering inside and outside cavities method and the effect of cavities length variation. This also includes the observation of lower to higher Q-factor on the PhC nanocavities. Consideration for 1D PhC nanocavities membrane is also discussed.

Chapter 5 (Microfluidic Channel System) reviews the background of microfluidic channel and its fabrication processes. The chapter discuss the measurement set up and instruments to perform optical characteristic of the fabricated structures. Fabricated structures measurement with microfluidic channel is analysed. Fabrication limitations on the device performance are discussed.

Chapter 6 (Optical Wave-Guiding Sensing) concerns the system setup and measurements results based on experiments carried out such as refractive index sensing, and device repeatability. The effect of different cavity length corresponds to high/low Q factor structures for refractive index sensing is discussed. The experiment on various analyte temperatures were carried out and the concerns about thermo-optic effects is given.

Chapter 7 (Conclusion and Future Work) summarize the work in this thesis and outlines possible future work.

## References

- [1.1] Vahala, Kerry J. "Optical microcavities." *Nature* 424, no. 6950 (2003): 839-846.
- [1.2] Carlborg, Carl Fredrik, Kristinn Björgvin Gylfason, A. Kaźmierczak, Fabian Dortu, MJ Banuls Polo, A. Maquieira Catala, G. M. Kresbach et al. "A packaged optical slot-waveguide ring resonator sensor array for multiplex label-free assays in labs-on-chips." *Lab on a Chip* 10, no. 3 (2010): 281-290.
- [1.3] Wang, Xiao-Ling, Guo-Fan Jin, and Jun Zhu. "Refractive index sensor." U.S. Patent 7,777,873, issued August 17, (2010).
- [1.4] Vollmer, Fea, D. Braun, A. Libchaber, M. Khoshima, I. Teraoka, and S. Arnold. "Protein detection by optical shift of a resonant microcavity." *Applied Physics Letters* 80, no. 21 (2002): 4057-4059.
- [1.5] Lai, Wei-Cheng, Swapnajit Chakravarty, Xiaolong Wang, Cheyun Lin, and Ray T. Chen. "On-chip methane sensing by near-IR absorption signatures in a photonic crystal slot waveguide." *Optics Letters* 36, no. 6 (2011): 984-986
- [1.6] Sloan, Courtney D. Kuhnline, Michael T. Marty, Stephen G. Sligar, and Ryan C. Bailey. "Interfacing lipid bilayer nanodiscs and silicon photonic sensor arrays for multiplexed protein–lipid and protein–membrane protein interaction screening." *Analytical Chemistry* 85, no. 5 (2013): 2970-2976
- [1.7] Aslan, Kadir, Joseph R. Lakowicz, and Chris D. Geddes. "Plasmon light scattering in biology and medicine: new sensing approaches, visions and perspectives." *Current opinion in chemical biology* 9, no. 5 (2005): 538-544
- [1.8] Seow, Nianjia, Yen Nee Tan, Lin-Yue Lanry Yung, and Xiaodi Su. "DNA-Directed Assembly of Nanogold Dimers: A Unique Dynamic Light Scattering Sensing Probe for Transcription Factor Detection." *Scientific Reports* 5 (2015).

- [1.9] Banada, Padmapriya P., Karleigh Huff, Euiwon Bae, Bartek Rajwa, Amornrat Aroonnual, Bulent Bayraktar, Abrar Adil, J. Paul Robinson, E. Daniel Hirleman, and Arun K. Bhunia. "Label-free detection of multiple bacterial pathogens using light-scattering sensor." *Biosensors and Bioelectronics* 24, no. 6 (2009): 1685-1692.
- [1.10] Cubillas, Ana M., Sarah Unterkofler, Tijmen G. Euser, Bastian JM Etzold, Anita C. Jones, Peter J. Sadler, Peter Wasserscheid, and Philip St J. Russell. "Photonic crystal fibres for chemical sensing and photochemistry." *Chemical Society Reviews* 42, no. 22 (2013): 8629-8648.
- [1.11] Chong, Su Sin, A. R. Aziz, and Sulaiman W. Harun. "Fibre optic sensors for selected wastewater characteristics." *Sensors* 13, no. 7 (2013): 8640-8668.
- [1.12] Singh, Sarika, Satyendra K. Mishra, and Banshi D. Gupta. "Sensitivity enhancement of a surface plasmon resonance based fibre optic refractive index sensor utilizing an additional layer of oxides." *Sensors and Actuators A: Physical* 193 (2013): 136-140.
- [1.13] Najiminaini, Mohamadreza, Erden Ertorer, Hao Jiang, Bozena Kaminska, Silvia Mittler, and Jeffrey JL Carson. "Three dimensional metallic nanostructures for bulk and bio-SPR sensing applications." In *SPIE BiOS*, pp. 89570I-89570I. International Society for Optics and Photonics, (2014).
- [1.14] Zeng, Shuwen, Dominique Baillargeat, Ho-Pui Ho, and Ken-Tye Yong. "Nanomaterials enhanced surface plasmon resonance for biological and chemical sensing applications." *Chemical Society Reviews* 43, no. 10 (2014): 3426-3452.
- [1.15] Šípová, Hana, and Jiří Homola. "Surface plasmon resonance sensing of nucleic acids: a review." *Analytica Chimica Acta* 773 (2013): 9-23.
- [1.16] Scullion, M. G., A. Di Falco, and T. F. Krauss. "Slotted photonic crystal cavities with integrated microfluidics for biosensing applications." *Biosensors*

and *Bioelectronics* 27, no. 1 (2011): 101-105.

- [1.17] De Vos, Katrien, Peter Debackere, Tom Claes, Jordi Girones, Wout De Cort, Etienne Schacht, Roel G. Baets, and Peter Bienstman. "Label-free biosensors on silicon-on-insulator optical chips." In *SPIE NanoScience+ Engineering*, pp. 739710-739710. International Society for Optics and Photonics, (2009).
- [1.18] Liang, Feng, Nigel Clarke, Parth Patel, Marko Loncar, and Qimin Quan. "Scalable photonic crystal chips for high sensitivity protein detection." *Optics Express* 21, no. 26 (2013): 32306-32312.
- [1.19] Li, Tingyu, Dingshan Gao, Daming Zhang, and Eric Cassan. "High-Q and High-Sensitivity One-Dimensional Photonic Crystal Slot Nanobeam Cavity Sensors." *IEEE Photonics Technology Letters* 28, no. 6 (2016): 689-692.
- [1.20] Luchansky, Matthew S., and Ryan C. Bailey. "High-Q optical sensors for chemical and biological analysis." *Analytical Chemistry* 84, no. 2 (2011): 793-821.
- [1.21] Ciminelli, C., F. Dell'Olio, D. Conteduca, C. M. Campanella, and M. N. Armenise. "High performance SOI microring resonator for biochemical sensing." *Optics & Laser Technology* 59 (2014): 60-67.
- [1.22] Park, Mi Kyoung, Jack Sheng Kee, Jessie Yiyi Quah, Vivian Netto, Junfeng Song, Qing Fang, Eric Mouchel La Fosse, and Guo-Qiang Lo. "Label-free aptamer sensor based on silicon microring resonators." *Sensors and Actuators B: Chemical* 176 (2013): 552-559.
- [1.23] Ullien, Daniela, Peter J. Harmsma, Shahina MC Abdulla, Bart M. de Boer, Duco Bosma, Ernst JR Sudhölter, Louis CPM de Smet, and Wolter F. Jager. "Protein detection on biotin-derivatized polyallylamine by optical microring resonators." *Optics Express* 22, no. 13 (2014): 16585-16594.
- [1.24] Silva, Susana, Edwin GP Pachon, Marcos AR Franco, Juliano G. Hayashi, F.

- Xavier Malcata, Orlando Frazão, Pedro Jorge, and Cristiano MB Cordeiro. "Ultrahigh-sensitivity temperature fiber sensor based on multimode interference." *Applied Optics* 51, no. 16 (2012): 3236-3242.
- [1.25] Biazoli, Claudcir R., Susana Silva, Marcos AR Franco, Orlando Frazão, and Cristiano MB Cordeiro. "Multimode interference tapered fiber refractive index sensors." *Applied Optics* 51, no. 24 (2012): 5941-5945.
- [1.26] Zinoviev, Kirill, Laura G. Carrascosa, José Sánchez del Río, Borja Sepúlveda, Carlos Domínguez, and Laura M. Lechuga. "Silicon photonic biosensors for lab-on-a-chip applications." *Advances in Optical Technologies* (2008).
- [1.27] Lee, Byeong Ha, Young Ho Kim, Kwan Seob Park, Joo Beom Eom, Myoung Jin Kim, Byung Sup Rho, and Hae Young Choi. "Interferometric fiber optic sensors." *Sensors* 12, no. 3 (2012): 2467-2486.
- [1.28] Liu, Qing, Yong Shin, Jack Sheng Kee, Kyoung Woo Kim, Siti Rafeah Mohamed Rafei, Agampodi Promoda Perera, Xiaoguang Tu et al. "Mach-Zehnder interferometer (MZI) point-of-care system for rapid multiplexed detection of microRNAs in human urine specimens." *Biosensors and Bioelectronics* 71 (2015): 365-372.
- [1.29] Yan, Hai, Yi Zou, Swapnajit Chakravarty, Chun-Ju Yang, Zheng Wang, Naimei Tang, Donglei Fan, and Ray T. Chen. "Silicon on-chip bandpass filters for the multiplexing of high sensitivity photonic crystal microcavity biosensors." *Applied Physics Letters* 106, no. 12 (2015): 121103.
- [1.30] Fenzl, Christoph, Thomas Hirsch, and Otto S. Wolfbeis. "Photonic crystals for chemical sensing and biosensing." *Angewandte Chemie International Edition* 53, no. 13 (2014): 3318-3335.
- [1.31] Baker, James E., Rashmi Sriram, and Benjamin L. Miller. "Two-dimensional photonic crystals for sensitive microscale chemical and biochemical sensing." *Lab on a Chip* 15, no. 4 (2015): 971-990.

- [1.32] Di Falco, A.; O'Faolain, L.; Krauss, T.F. Chemical sensing in slotted photonic crystal heterostructure cavities. *Applied Physics Letters*. (2009) 94.
- [1.33] Li, Tingyu, Dingshan Gao, Daming Zhang, and Eric Cassan. "High-and High-Sensitivity One-Dimensional Photonic Crystal Slot Nanobeam Cavity Sensors." *IEEE Photonics Technology Letters* 28, no. 6 (2016): 689-692.
- [1.34] Yang, Daquan, Huiping Tian, and Yuefeng Ji. "Optical Fiber Tips Integrated with High-Q Fano-Resonance Pillar-Array Photonic-Crystals for High Sensitive Remote Sensing." In *Asia Communications and Photonics Conference*, pp. AS4I-5. Optical Society of America, (2015).
- [1.35] Barrios, Carlos A., Kristinn B. Gylfason, Benito Sánchez, Amadeu Griol, Hans Sohlström, Miquel Holgado, and Raphael Casquel. "Slot-waveguide biochemical sensor." *Optics Letters* 32, no. 21 (2007): 3080-3082.
- [1.36] Claes, Tom, Wim Bogaerts, and Peter Bienstman. "Experimental characterization of a silicon photonic biosensor consisting of two cascaded ring resonators based on the Vernier-effect and introduction of a curve fitting method for an improved detection limit." *Optics Express* 18, no. 22 (2010): 22747-22761.
- [1.37] Biacore (online) [www.biacore.com](http://www.biacore.com)
- [1.38] Genalyte (online) [www.genalyte.com](http://www.genalyte.com)
- [1.39] Axela (online) [acelabiosensor.com](http://acelabiosensor.com)
- [1.40] Yablonovitch, Eli. "Inhibited spontaneous emission in solid-state physics and electronics." *Physical Review Letters* 58.20 (1987): 2059.
- [1.41] John S, "Strong localization of photons in certain disordered dielectric superlattices" *Physics Review Letters*. (1987), 53 2186-2189.

- [1.42] Noda, Susumu, Masayuki Fujita, and Takashi Asano. "Spontaneous-emission control by photonic crystals and nanocavities." *Nature Photonics* 1, no. 8 (2007): 449-458.
- [1.43] Lukin, M. D. "Colloquium: Trapping and manipulating photon states in atomic ensembles." *Reviews of Modern Physics* 75, no. 2 (2003): 457.
- [1.44] Prieto, I., J. M. Llorens, Luis Enrique Muñoz-Camúñez, A. G. Taboada, J. Canet-Ferrer, José María Ripalda, C. Robles, G. Muñoz-Matutano, Juan Pascual Martínez-Pastor, and Pablo Aitor Postigo. "Near thresholdless laser operation at room temperature." *Optica* 2, no. 1 (2015): 66-69.
- [1.45] Koyama, Fumio. "Recent advances of VCSEL photonics." *Lightwave Technology, Journal of* 24, no. 12 (2006): 4502-4513.
- [1.46] Lai, Chun-Feng. "Luminescence-Spectrum Modification of White Light-Emitting Diodes by Using 3D Colloidal Photonic Crystals." In *Photonic Crystals*. InTech, (2015).
- [1.47] K. J. Valaha “Optical microcavities” *Nature*, 424(6950):839-846. (2003).
- [1.48] Portalupi, Simone L., Matteo Galli, Christopher Reardon, T. F. Krauss, Liam O’Faolain, Lucio C. Andreani, and Dario Gerace. "Planar photonic crystal cavities with far-field optimization for high coupling efficiency and quality factor." *Optics Express* 18, no. 15 (2010), 16064-16073.
- [1.49] Dündar, Mehmet A., Bowen Wang, Richard Nötzel, Fouad Karouta, and Rob W. van der Heijden. "Optothermal tuning of liquid crystal infiltrated InGaAsP photonic crystal nanocavities." *JOSA B* 28, no. 6 (2011): 1514-1517.
- [1.50] P. Lalanne, S. Milas, and J. P. Hugonin, “Two physical mechanisms for boosting the quality factor to cavity volume ratio of photonic crystal microcavities,” *Optics Express* 12, (2004), 458–467.

## Chapter 2: Modelling of Photonic Structures

- 2.1 Introduction
- 2.2 Photonic Modelling Method
- 2.3 The Finite-Difference Time-Domain Method
- 2.4 Lumerical FDTD
  - 2.4.1 Source and Boundary Condition
  - 2.4.2 Mesh Condition
- 2.5 Method of Extracting Quality Factor
- 2.6 Modeling 1-D PhC Nanocavities
- 2.7 Conclusions
- References

## 2.1 Introduction

In this chapter, an overview of computational photonics structures is given. The Finite-Difference Time-Domain (FDTD) method is described with explanation of its operation, excitation, and boundary conditions. The photonics band gaps for 1-D photonics crystals structures are discussed. In addition, technique of extracting the Q factor of simulated resonances is also explained. The requirements for modelling 1D PhC using 2D and 3D FDTD are also discussed.

## 2.2 Photonic Modelling Method

There are two approaches to optimise the design of wave-guiding structures available, one is to fabricate variations of designed structures and then optimise them by experiment and another is to simulate the theoretical model and investigate the structures analytically and computationally. The fabrication of designed structures has the advantage of being fast for simple cases. Nonetheless, it can be costly and time consuming to fabricate various designed structures. With recent advances in computing technology, faster processors and larger amount of random access memory (RAM) available; simulating designated structures computationally has advantages of both speed and cost. However, the simulated structures must be verified by the fabrication and experiment.

In 1865, James Clerk Maxwell developed the theoretical laws of classic electrodynamics [2.1, 2.2]. He claimed that light itself was an electromagnetic phenomenon, and postulated electric and magnetic fields are related to each other and their enclosing media in space and time. The combinations of several laws in a unified notation are collectively known as Maxwell's equations. Time-dependent Maxwell's equations are given in differential form as Faraday's Law (Eq. 2.1), Ampere's Law (Eq. 2.2), Gauss's Law for electric field (Eq. 2.3) and Gauss's Law for magnetic field (Eq. 2.4).

$$\frac{\partial \vec{B}}{\partial t} = -\nabla \times \vec{E} - \vec{M}$$

(Eq. 2.1)

$$\frac{\partial \vec{D}}{\partial t} = \nabla \times \vec{H} - \vec{J}$$

(Eq. 2.2)

$$\nabla \cdot \vec{D} = 0$$

(Eq. 2.3)

$$\nabla \cdot \vec{B} = 0$$

(Eq. 2.4)

Where are (all in MKS unit);

- $\vec{E}$  : Electric field (volts/m)
- $\vec{D}$  : Electric flux density (coulombs/m<sup>2</sup>)
- $\vec{H}$  : Magnetic field (amperes/m)
- $\vec{B}$  : Magnetic flux density (webers/m)
- $\vec{M}$  : Magnetic current density (volts/m<sup>2</sup>)
- $\vec{J}$  : Electric current density (amperes/m<sup>2</sup>)

In modelling the designed structures, the modeller implements and solves the Maxwell's equations computationally. There are various techniques for solving Maxwell's equations [2.3]. Some common techniques are Finite Element Method (FEM) [2.4], Method of Moment (MoM) [2.5] and Finite -Difference Time-Domain (FDTD) [2.6, 2.7, and 2.9].

The modeller can simulate the propagation of electric and magnetic fields of a system using FDTD, a time-domain technique. FDTD uses the source (i.e. broadband pulse) and boundary condition approximation. The response of the system can be obtained over wide range of frequencies using a single simulation. This is very convenient to simulate nanophotonics structures because of their small geometry [2.7].

Therefore, this method suits in the case of photonics structures such as 1-D PhC nanocavities, when the light is trapped within the small volume.

## 2.3 The Finite-Difference Time-Domain Method (FDTD)

The FDTD method is commonly used to simulate nanophotonic structures because the method is able to implements and solves Maxwell's equations for wave-guiding structures with very small volume or space domain. The method was based on volume sampling of electric field, E-field and magnetic field, H-field within the specified grid over a period of time. Yee introduced the initial method in 1966 [2.8].

An outline is given in Appendix A, the Yee algorithm configuration centres the E-field and H-field in three-dimensional space. Therefore, the E-field is circulated by four H-field and vice versa. Based on Yee algorithm configuration, the Maxwell's differential equations calculation of E-field in time is dependent on the changes in the H-field across space. Subsequently, the updated value of E-field in time is dependent to the value of E-field and the numerical curl distribution of H-field in space. In similar approach, H-field is calculated. Both E-field and H-field in space are in time-stepped. This is basic fundamental of FDTD calculation relation to Maxwell's equations.

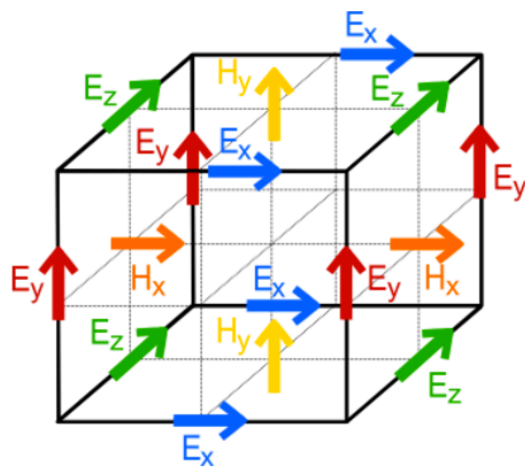


Figure 2.1 Yee algorithm configurations [2.20]

As in the computational domain, mentioned earlier, Yee algorithm computes all

the E-field then the H-field in time stepped in a ‘leapfrog’ manner. Poynting vector in Yee algorithm configurations specifies the magnitude and direction of the rate of electromagnetic energy transfer. All the computed E-fields are stored in memory at particular time point arise from the previous stored H-field. These cycles will continuously be computed based on iteration defined by the user. Taflove and Hagness has discussed this in further detail in their book regarding on the FDTD method [2.9].

## 2.4 Lumerical FDTD

There are several commercial software packages that have been used during this work. Initially, RSoft FullWAVE from Synopsys [2.10] was used to model the structures. It is able to calculate 2D and 3D FDTD computations. However, in order to extract the Q factor values the more efficient, FDTD Solutions from Lumerical was used [2.11]. This is because RSoft FullWAVE uses longer time and more computing power in 3D FDTD computations while, Lumerical FDTD enables the user to specify how many nodes in the cluster solely working on calculating FDTD. In addition, Lumerical FDTD is able to calculate and extract the Q values more easily, which will be explained later in this chapter.

### 2.4.1 Sources and Boundary Condition

There are several types of common source when exciting the nanophotonic structures in FDTD numerical modelling. The most common types of source were used are the Plane Wave, the Continuous Wave (CW) and the Gaussian modulated sinusoid.

In this work, a Plane wave with integrated mode solver built by Lumerical FDTD was used to excite the structures. The graphic user interface (GUI) of integrated mode solver was used to find the steady state field pattern at a certain frequencies. A range of frequencies can be produced and the broadband response of the structure can be obtained.

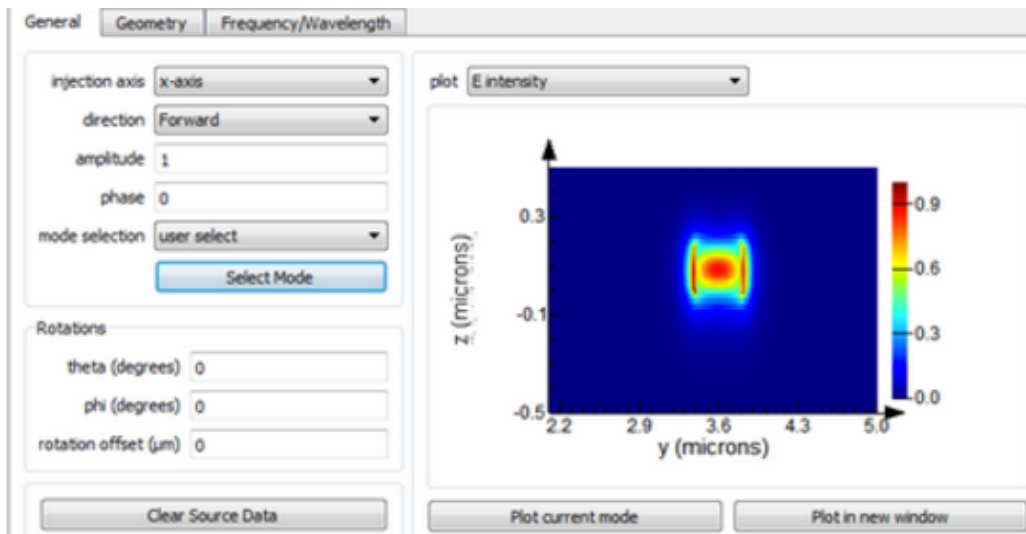


Figure 2.2: Diagram representing GUI of integrated mode solver used to find the range of frequencies to be excited into the structures [2.11].

Another consideration when implementing the FDTD algorithm is to understand the active domain of the modelling. The active domain must be large enough to enclose the structure specifically at the area of interest. The computation domain must remain ‘open’, however, the FDTD modelling must be kept valid. Hence, the boundary condition must be made to absorb and suppress the reflection of the outgoing waves. The most common absorbing boundary condition used that has extremely small local reflection is the Perfectly Matched Layer (PML) boundary [2.12, 2.13]. The PML is a region where the plane waves of reflection, polarised, at certain frequencies are matched at the boundary. The PML is designed to absorb the outgoing waves from the active computation domain without reflecting them back to the area of interest.

## 2.4.2 Mesh Condition

In recent years, nanometre structures in optical devices become crucial to operate at broad wavelengths ranges. The ‘staircasing’ approach (example shown in Figure 2.3) solved the FDTD algorithm for larger structures. However, for smaller

structures, this staircasing approach modelling appears to have higher required greater computing power in order to compute each mesh cell. For example, as shown in Figure 2.3, a circle does not align with rectangular grid; therefore a smaller grid must be made. The grid resolution is increased to make the approximation and therefore creates longer computation time.

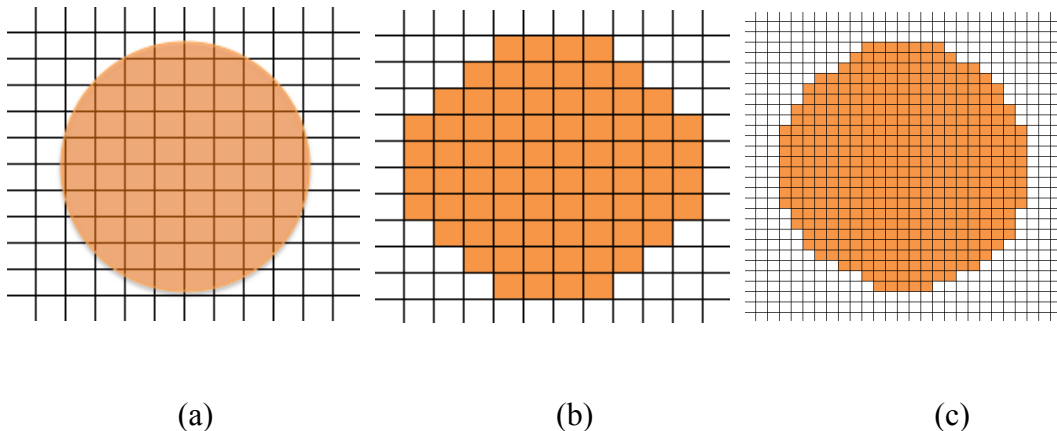


Figure 2.3: Schematic diagrams illustrating the ‘staircasing’ approaches (a) a circle structures in grid resolution (b) and (c) depicts the circular shape in big and small resolution grid to accommodate the circle structures.

To accommodate the smaller design in the FDTD algorithm, the conformal mesh technique (CMT) was introduced [2.14]. The CMT helps to adjust the mesh cell features by solving FDTD computation near the structures boundary. With these features, CMT can enhance the modelling accuracy for a given mesh size. Therefore the mesh size and location must be carefully placed. Further explanation about the technology is described in [2.15].

## 2.5 Method of Extracting Quality Factor

There are several ways to extract the Q factor when using the numerical calculation software or in this case, Lumerical FDTD. Commonly, there are probes of

---

the E and H-fields, a detector of the frequency response, or calculation script that can be used in the GUI of the software to calculate the Q. Nonetheless, choosing the suitable extraction method can eliminate extra work and time needed when modelling the structures.

A general definition of Q is;

$$Q = 2\pi \frac{\text{Stored Energy}}{\text{Energy lost per cycle}}$$

(Eq. 2.5)

To use the ratio of stored energy and energy lost per cycle method, the E and H-fields were probed at the cavity point in the structures. In the modelling, the mode is launched to the structure and was allowed to decay away. Then, for the FDTD calculation, each of the E and H-fields at each time step were stored. This made the method of extraction the Q values is time consuming and computationally expensive.

Another way to extract the Q value is by using the detector frequency response. The Q can also be defined as ratio of resonant frequency of the mode and full width at half maximum (at -3dB bandwidth) of the response intensity;

$$Q = \frac{\lambda o}{\Delta\lambda FWHM} = \frac{f o}{\Delta f FWHM}$$

(Eq. 2.6)

Can be translated to;

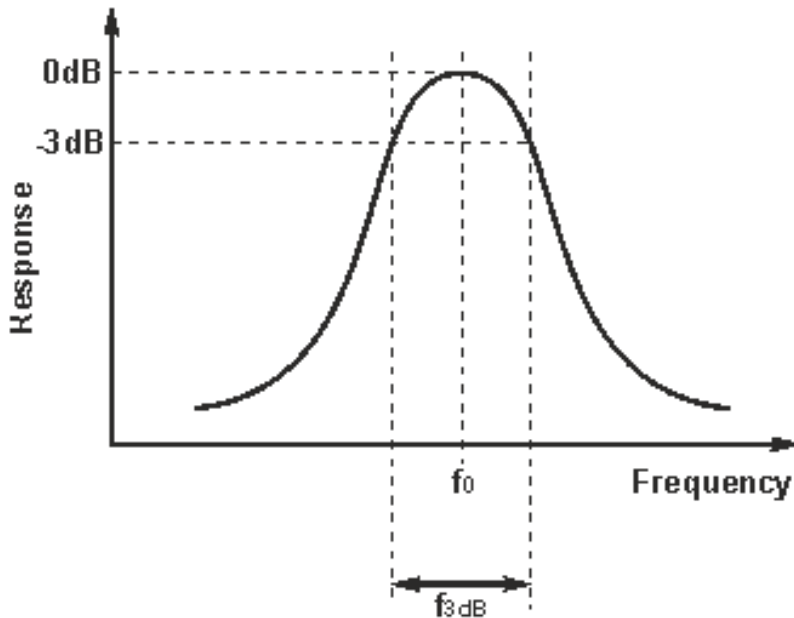


Figure 2.4: Graph describes the Q relation to its bandwidth.

Where  $\lambda_o$  and  $f_o$  are the resonant wavelengths and the resonant frequencies respectively.

During the modelling step, the detector was used to collect the frequency response of the system. This method is suitable to calculate low Q values. The frequency response of the system can only be calculated after the time step is done. The minimum time step is set long enough to have the entire mode decayed away. For the high Q calculations, the time step is longer, hence, the computational cost is higher and it is time consuming.

The alternative method of extracting the Q is using script embedded in the modelling. In Lumerical FDTD, the script allows the modelling to calculate the Q with less time steps. The script determines the Q by the slope of the envelope of the decaying mode using the equation below;

$$Q = \frac{-2\pi f_o \log(e)}{2m}$$

Where  $f_o$  is resonant frequency of the mode and m is the slope of the decay. The derivation of the equation above can be found in [2.16].

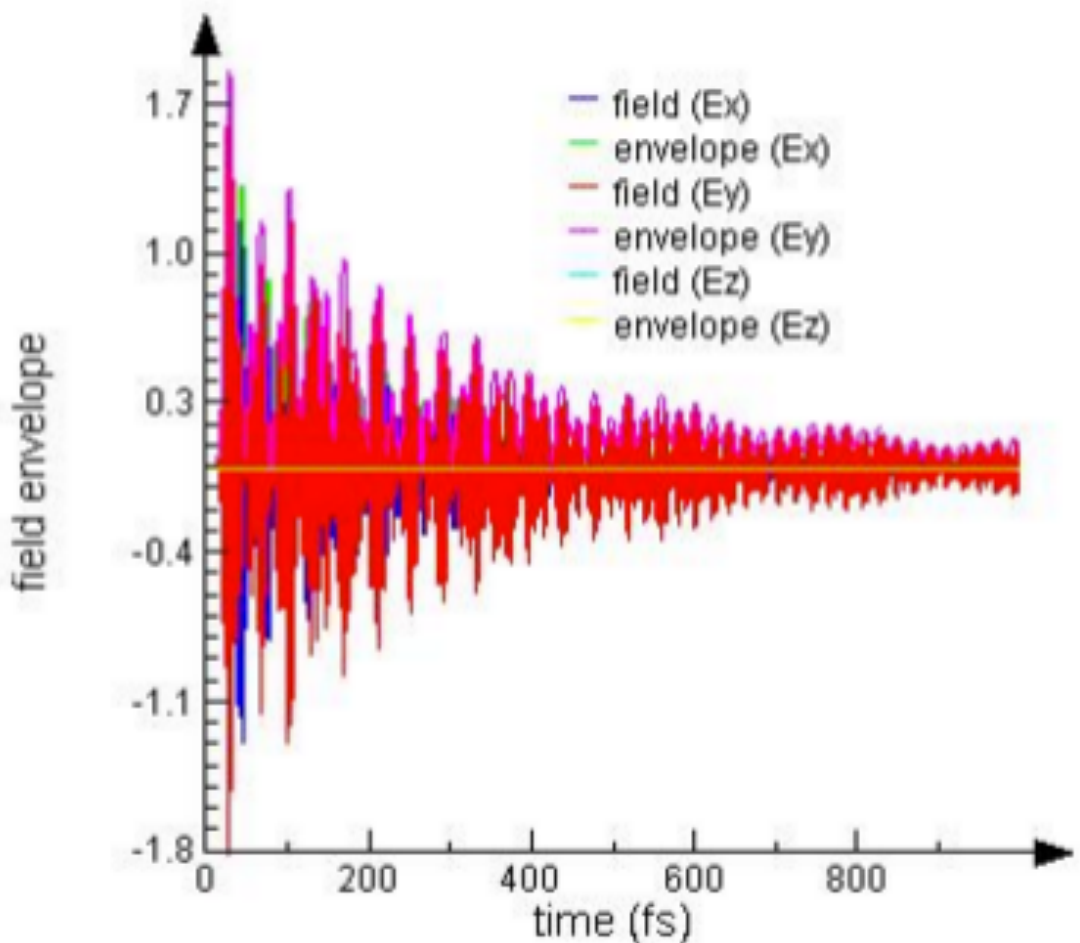


Figure 2.5: Graph depicts the time decay of the E and H-field with their envelopes [2.11].

## 2.6 Modelling 1-D PhC Nanocavities

As discussed earlier, the main aspects that are needed to model the nanophotonic structures are structure's refractive index,  $n_{\text{eff}}$  distribution, source or excitation mode, computational area with PML boundary layer, modelling time and mesh size through the resolution grid.

In 2D FDTD modelling, the effective index,  $n_{\text{eff}}$  of the PhC planar waveguide was used. The  $n_{\text{eff}}$  is obtained using mode solver for effective index approximation available online [2.17].

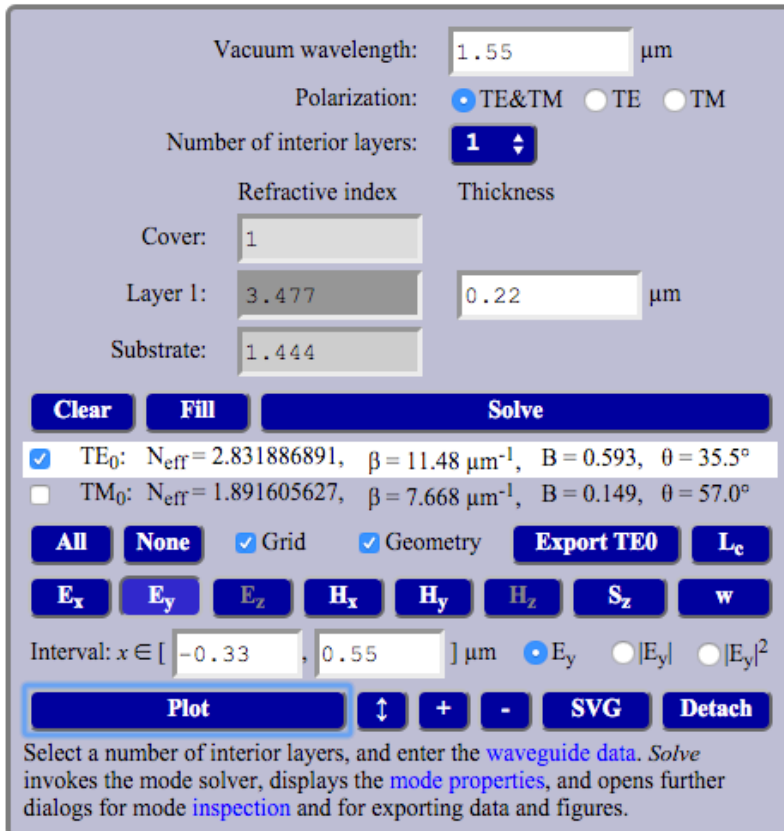


Figure 2.6: GUI of mode solver program to calculate the effective index approximation of PhC waveguide [2.17].

The effective index of SOI PhC waveguide,  $n_w$  given as 2.83. Next, the plane wave was used for this modelling and was set at the wavelengths ranges from 1.3 – 1.8  $\mu\text{m}$  for the full spectrum inspection. Later, it was set at smaller wavelength range to obtained reliable Q values. Based on the effective index approximation calculation, the evanescent tail of the mode decays at 0.5  $\mu\text{m}$ . The modelling area must proportional to the PhC waveguide. Therefore, the PML area was set at 5  $\mu\text{m}$  (x-direction) x 10  $\mu\text{m}$   $\mu\text{m}$  (y-direction) and 5  $\mu\text{m}$  (z-direction) for 3D FDTD computation. This would provide sufficient space for the mode to reflect within the internal FDTD computation area and, or absorbed by the PML.

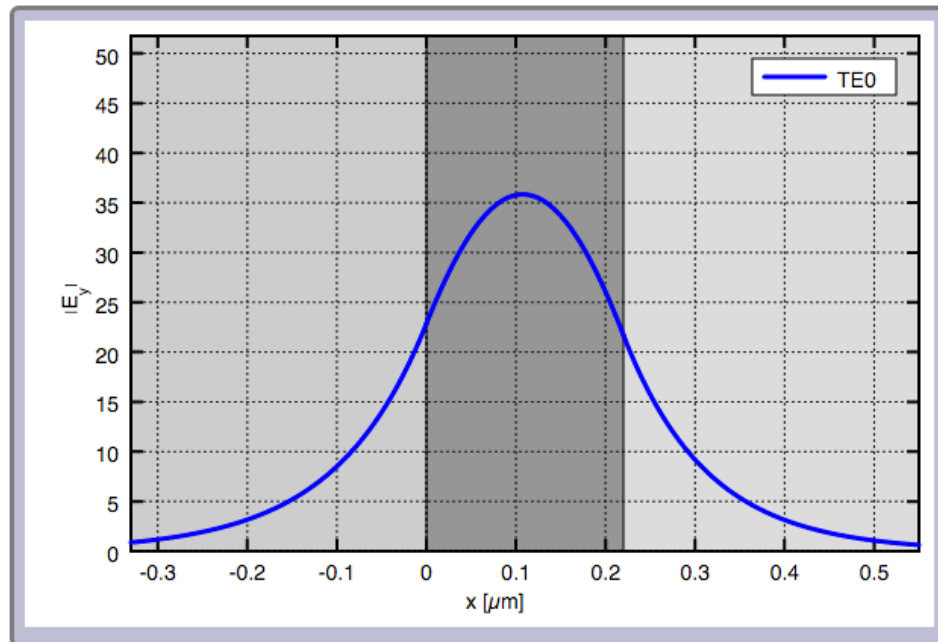


Figure 2.7: Result of the vertical distribution of TE mode in  $0.22 \mu\text{m}$  thick of the PhC waveguide from the mode solver approximation program. The x-direction represents the vertical cut through the PhC waveguide [2.17].

One of the crucial parameters that contribute to the modelling accuracy is the mesh size or the resolution grid and where it is located. The period of the Bragg mirror holes in the PhC waveguides must aligned with the integer of the resolution grid [2.18]. The alignment reflects the periodicity in the PhC structures. The overall resolution grid was set at  $10 \text{ nm}$  and the overlap mesh size at the PhC period was set at  $5 \text{ nm}$ .

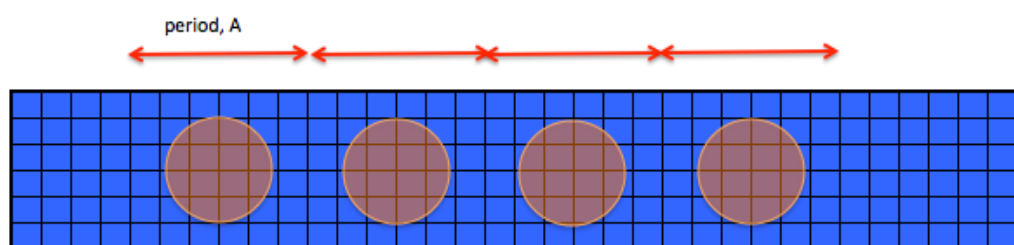


Figure 2.8: Picture illustrates the association between PhC waveguide period,  $A$  and the integer number of resolution grid. For example, each periods are divided into  $6 \times 6$  cells.

Later, the 3D FDTD computation approach has been used to model the PhC waveguide structures. Apart from the additional PML area, most of the parameters in the 2D FDTD calculation remain the same. The modelling results were compared with Md Zain's [2.19] previous experimental results. The results only show a slight different from the experimental with a lower Q values. Nonetheless, the modelling is to show better understanding of the PhC waveguide based on SOI. This helped to fabricate the sensor device for later experiments. The fabrication of the PhC waveguide is shown in Chapter 3 and the design of the PhC waveguide is given in Chapter 4.

## 2.7 Conclusions

This chapter outlined the modelling technique for the photonic structures. In general, the theories of the modelling have been discussed. The FDTD computation method was chosen because of its capability to model the high Q 1D PhC waveguides. In addition, by using Lumerical FDTD, the computations were faster with less computation cost. The parameters such as the source, boundary area and the mesh conditions play important roles to obtain accuracy of the modelling. 2D and 3D FDTD computation approaches have been used to model the structures to gain an overview of the device behaviours. Chapter 2 explains the method used to extract effective index and the FDTD computation; meanwhile the design and simulation results are discussed in Chapter 4.

## References

- [2.1] Maxwell J C, "A dynamic theory of the electromagnetic field" Proc. of the Royal Soc. 13 (1864), 531-536.
- [2.2] Maxwell J C, "A Treatise on Electricity and Magnetism" Dover Publications, (1954).
- [2.3] Davidson, David B. *Computational electromagnetics for RF and microwave engineering*. Cambridge University Press, (2010).
- [2.4] Desai, Chandrakant S., and John F. Abel. *Introduction to the finite element method: A numerical method for engineering analysis*. Van Nostrand Reinhold, (1972).
- [2.5] Harrington, Roger F., and Jan L. Harrington. *Field computation by moment methods*. Oxford University Press, (1996).
- [2.6] Xiao, S., Vahldieck, R. and Jin, H., Full-wave analysis of guided wave structures using a novel 2-D FDTD. *Microwave and Guided Wave Letters, IEEE*, 2(5), pp.165-167 (1992).
- [2.7] Burr, Geoffrey W. "FDTD as a nanophotonics design optimization tool." In *Int. Symp. Photonic Electromagn. Crystal Structures V, Kyoto, Japan*. (2004).
- [2.8] Kane Yee, "Numerical solution of initial boundary value problems involving Maxwell's equations in isotropic media". *IEEE Transactions on Antennas and Propagation* 14 (3): (1966), 302–307
- [2.9] Hagness, S., and Allen Taflove. "Computational electrodynamics: The finite-difference time-domain method." *Norwood, MA: Artech House* (2000).
- [2.10] RSoft FullWAVE (online) <https://optics.synopsys.com/rsoft/>

- [2.11] Lumerical FDTD (online) <https://www.lumerical.com/>
- [2.12] Bérenger, Jean-Pierre. "Perfectly matched layer (PML) for computational electromagnetics." *Synthesis Lectures on Computational Electromagnetics 2*, no. 1 (2007): 1-117.
- [2.13] Gedney, Stephen D., and Bo Zhao. "An auxiliary differential equation formulation for the complex-frequency shifted PML." *Antennas and Propagation, IEEE Transactions on* 58, no. 3 (2010): 838-847.
- [2.14] Yu, Wenhua, and Raj Mittra. "A conformal finite difference time domain technique for modeling curved dielectric surfaces." *Microwave and Wireless Components Letters, IEEE* 11, no. 1 (2001): 25-27.
- [2.15] Conformal Mesh Technology by Lumerical (online)  
[https://kb.lumerical.com/en/ref\\_sim\\_obj\\_mesh\\_refinement\\_options.html](https://kb.lumerical.com/en/ref_sim_obj_mesh_refinement_options.html)
- [2.16] Lumerical FDTD Q calculation (online)  
[https://kb.lumerical.com/en/diffractive\\_optics\\_cavity\\_q\\_calculation.html](https://kb.lumerical.com/en/diffractive_optics_cavity_q_calculation.html)
- [2.17] Hammer M., 2D Multilayer waveguide mode solver variational effective index approximation (online) <http://wwwhome.math.utwente.nl/~hammer/eims.html>
- [2.18] Lavrinenko, A., Borel, P., Frandsen, L., Thorhauge, M., Harpøth, A., Kristensen, M., Niemi, T. and Chong, H., Comprehensive FDTD modelling of photonic crystal waveguide components. *Optics Express*, 12(2), pp.234-248, (2004).
- [2.19] Zain, A.R.M., Johnson, N.P., Sorel, M. and Richard, M., Ultra high quality factor one dimensional photonic crystal/photonic wire micro-cavities in silicon-on-insulator (SOI). *Optics express*, 16(16), pp.12084-12089 (2008).
- [2.20] FDTD (online) [https://www.feko.info/product-detail/numerical\\_methods/fdtd/finite-difference-time-domain](https://www.feko.info/product-detail/numerical_methods/fdtd/finite-difference-time-domain)

# Chapter 3: Fabrication Process

3.1 Introduction

3.2 Silicon-On-Insulator (SOI) Platform

3.3 Overview of the process flow

3.4 Wafer chip preparation

3.5 Device Patterning

    3.5.1 Alignment Markers

    3.5.2 Silicon waveguide definition

        3.5.2.1 CAD Layout

        3.5.2.2 Fracturing & Proximity Effect Correction

        3.5.2.3 E-beam Resist, Dose Test & EBL Exposure

        3.5.2.4 Silicon Dry Etching

    3.5.3 Silicon Membrane

3.6 Waveguide Coupling

    3.6.1 Adiabatically tapered coupling method

    3.6.2 Planar inverted tapers with low index polymer block coupling method

3.7 Overall Device Design

3.8 Conclusions

3.9 References

## 3.1 Introduction

In this chapter, fabrication processes involved in developing PhC nanocavities structures are described. First, a brief introduction of material used in this work is presented, followed by an overview concerning the fabrication process flow. The fabrication process includes alignment markers, Silicon waveguides, membrane and block polymer coupler patterning using the Vistec VB6 electron beam lithography tool. The patterns were defined by dry-etch process using reactive ion etching for the waveguide slab while for the membrane definition, wet chemical etch using Hydrofluoric acid was used. In addition, block polymer coupling with inversed tapers method is discussed. The block polymer couplings improve the coupling efficiency and reduce strong Fabry-Perot oscillations effects during device measurement.

## 3.2 Silicon-On-Insulator (SOI) Platform

Sub-micron silicon strip waveguides on silicon dioxide insulation layer embedded on silicon substrates (SOI) have attracted a lot of interest to various research groups (IMEC, IBM, Cornell, NTT, Yokohama, MIT, JWNC.) [3.1–3.4]. SOI waveguides allow for the fabrication of extremely compact photonic circuits based on standard CMOS processing.

The geometry of the SOI chosen for this work is silicon of  $220\text{ nm}$  thick,  $2\text{ }\mu\text{m}$  of embedded silicon dioxide, with a thick silicon substrate. The SOI from SOITEC was used for this work an outline of their ‘Smart-Cut’ technology [3.5] is shown in figure 3.1.

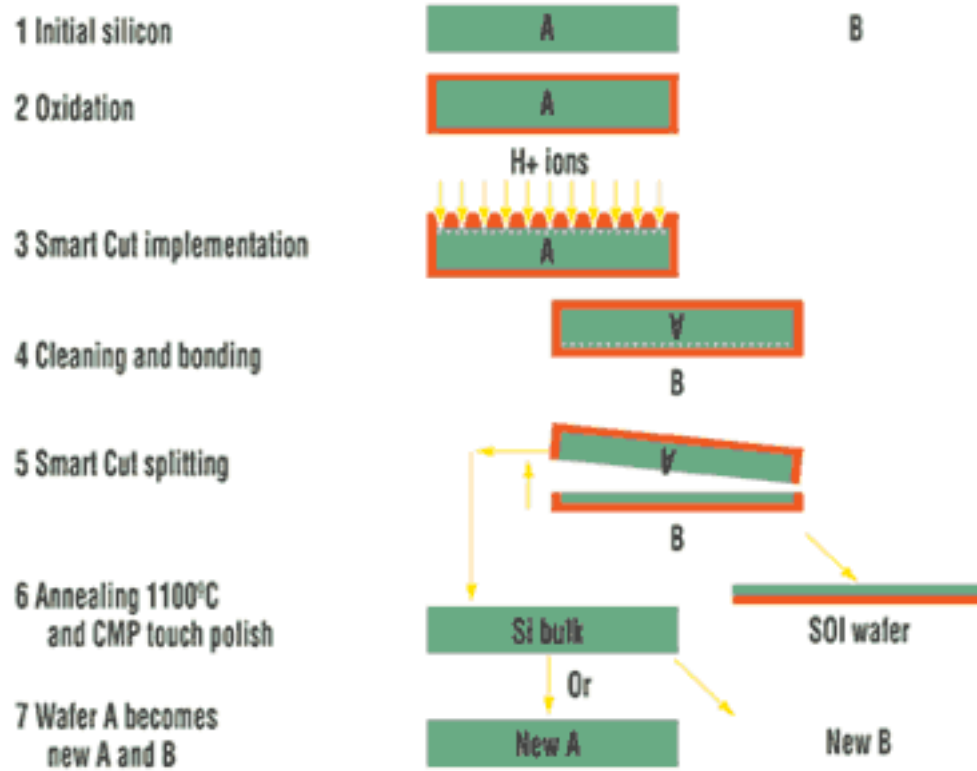


Figure 3.1: Smart-Cut technology process for SOI fabrication from SOITEC [3.5].

### 3.3 Overview of the process flow

The main processes involved in fabricating PhC nanocavities are summarized in the process flow as shown in Figure 3.2. Some of the process flows are routinely used in the James Watt Nanofabrication Centre (JWNC) cleanroom to fabricate devices. For example, multiple EBL jobs require markers for alignment. The process flow is divided into three main sections. These are fabrication of alignment markers for multiple EBL jobs (Figure 3.2 (a)), fabrication of the waveguide devices (Figure 3.2 (b)) and the fabrication of the coupling feeder waveguides (Figure 3.2 (c)). Thorough inspections and measurement are required after all EBL jobs and some repeated steps maybe needed (e.g. longer etching time).

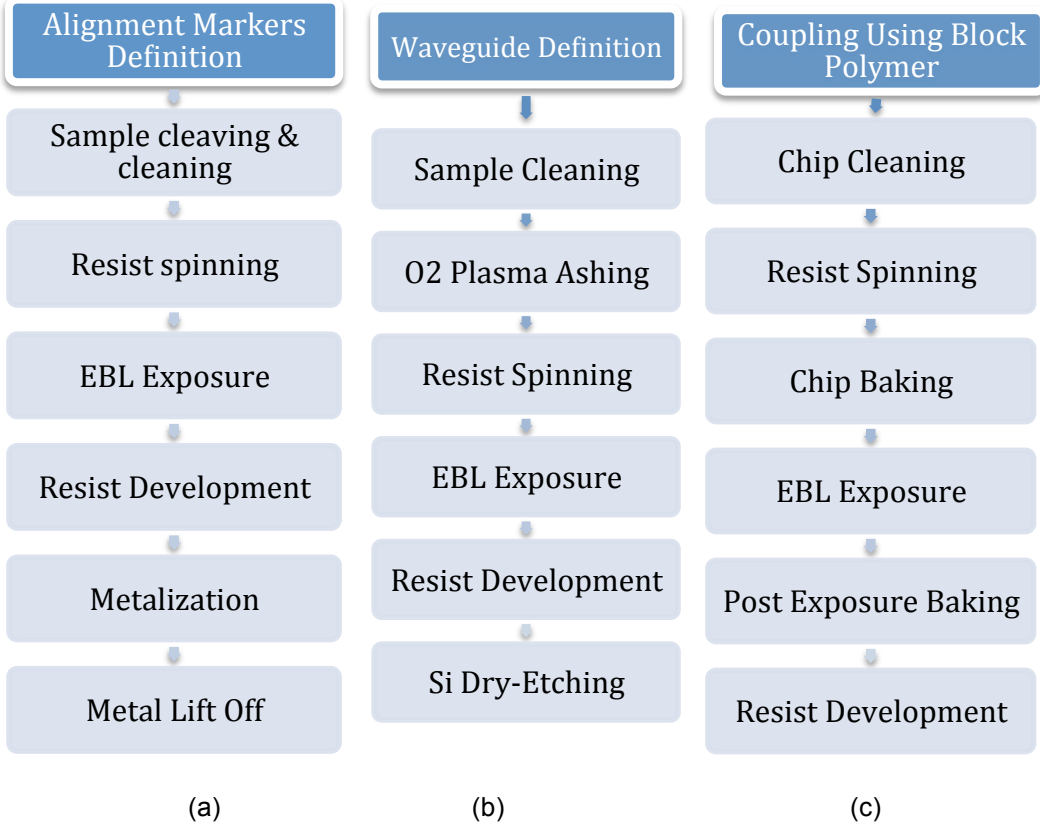


Figure 3.2: Summarized process flow of the fabrication process of PhC nanocavities. (a), (b) and (c) are fabrication steps in order.

### 3.4 Wafer chip preparation

In the fabrication process, Silicon-On-Insulator (SOI) was chosen to fabricate the optical waveguide structure. The SOI comes in 8 inches wafer and then was cleaved into 20 x 20 mm sized chip. The cleaving was carried out in a semi-clean environment and sample was thoroughly cleaned before further process. An acetone and isopropyl alcohol (IPA) from Fisher Scientific and Sigma-Aldrich respectively were used for the substrate cleaning routine. The wafer chip was immersed into an ultrasonic bath in plastic beakers for 5 minutes each. The chip was not allowed to self-dry after each cleaning step and the excess of the IPA was blown away from the chip using a nitrogen gun. IPA has lower surface tension than water, and is not easily self-dried it is the preferred final cleaning step for high aspect ratio structures. Most of the wafer chip preparation processes were performed under the laminar flow hood condition in JWNC cleanroom except for cleaving.

## 3.5 Device Patterning

Lithography is a common technique to transfer the designed pattern onto the surface material. During lithography, an energy source is used to modify the thin polymer layer called resist. There are a few types of lithography such as photolithography (light) [3.6], x-ray lithography [3.7], electron beam lithography [3.8], and focus ion beam lithography [3.9].

Photolithography is common to CMOS technology. It is capable to mass-produce patterns using reusable mask plate, thus gives lower cost per unit device. A SUSS Microtec Mask Aligner 6 (MA 6), a photolithography tool was used to fabricate pattern for the master mould on microfluidic channel.

The most crucial step in fabrication process is patterning of sub-micron structure with an accurate alignment. In this work, state-of-the-art, Leica Vector Beam 6 (VB 6) UHR-EWF electron beam lithography tool was used to fabricate device pattern. EBL provides high electron beam resolution and large depth of field for patterning. It is highly flexible to modify the design when necessary, therefore suitable for prototyping. EBL does not need a mask since it can write directly on the surface material. EBL tool uses 50 or 100 *keV* electrons beam and able to produce a spot at the size of 4 *nm* widths and - resolution of 0.5 *nm* [3.10]. However the ultimate resolution is determined by the resist and backscattered electrons that also expose the resist.

In this work, both positive tone and negative tone resists were used during the fabrication process. Positive tone resists develop away at exposed regions, whereas in the case of negative tone resist, the developed region remains behind after development.

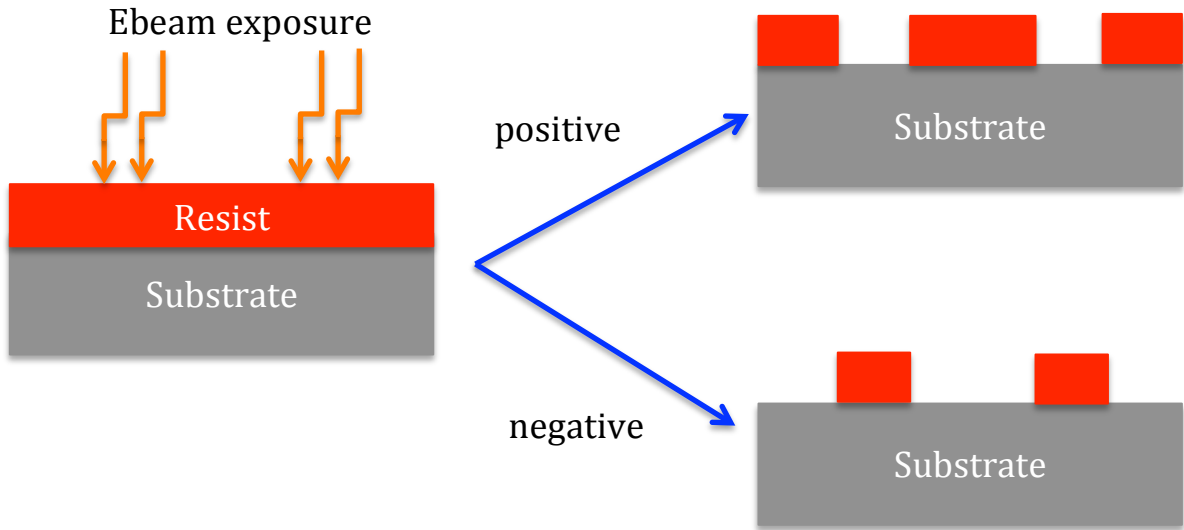


Figure 3.3: Schematic diagrams of positive and negative tone resist behaviour after development process.

### 3.5.1 Alignment Markers

The precision of the device patterning primarily depends on the relationship between the pre-existing alignments markers and planned patterns. In this work, the alignments markers were designed to align the EBL tools for each patterning jobs. The markers consist of a cross markers on the bottom and nine square blocks on each corner of the chip as shown in Figure 3.4.

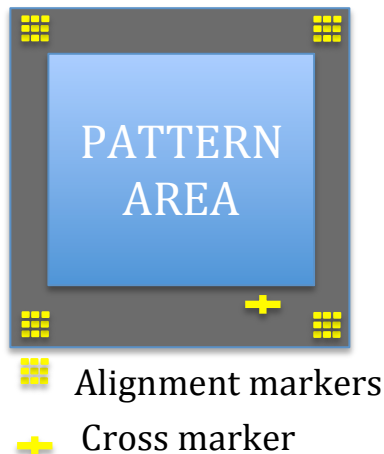


Figure 3.4: Schematic diagram of  $20 \times 20 \text{ mm}$  wafer chip with the alignment markers and the pattern area

The alignment markers (sized  $50 \mu m \times 50 \mu m$  each) on the wafer chip were patterned using double layer high-resolution positive tone resist of Polymethyl methacrylate (PMMA) from MicroChem Corp. Both layers of 12 % 2010 and 4 % 2041 PMMA were spun onto the wafer chip at 5000 rpm for 1 minute. After each resist layer was spun, the wafer chip was placed into  $180^{\circ}C$  oven for at least 2 hours before the next process. This step resulted in evaporation of any residual solvents from the resist and generates stronger adhesion with the substrate. Commonly, e-beam exposure dose for PMMA ranges from 100 to  $500 \mu C/cm^2$ . In this process, the alignment markers were patterned onto wafer chip used a dose of  $500 \mu C/cm^2$ . The higher (12 % 2010) and lower (4 % 2041) sensitivity layers of PMMA, give  $535 nm$  and  $100 nm$  respectively. These two layers created an undercut profile, which prevents metallization at resist ledges; hence better metal lift off can be achieved. An undercut profile was realized after resist development process. The developer solution used is Methyl isobutyl ketone (MIBK) and IPA with a 1:1 ratio.

Next, the wafer chip was placed into Plasma Oxygen Asher for 2 minutes at  $20 W$  to give the surface stronger adhesion before metallization. A bi-layer of Nickel (Ni) and Gold (Au) were deposited onto the patterned wafer chip with the thickness of  $20 nm$  and  $150 nm$  respectively. The metal lift-off process is attained by immersing the wafer chip into the acetone inside the temperature controlled of  $40^{\circ}C$  hot water bath. The length of time for metal lift-off usually depends on the resist mask quality. For this work, wafer chip was left overnight in the immersed hot acetone. The metal layers were lifted off by air blown into the hot acetone using plastic pipet. The simplified process flow of fabricating the alignment markers is shown in Figure 3.5.

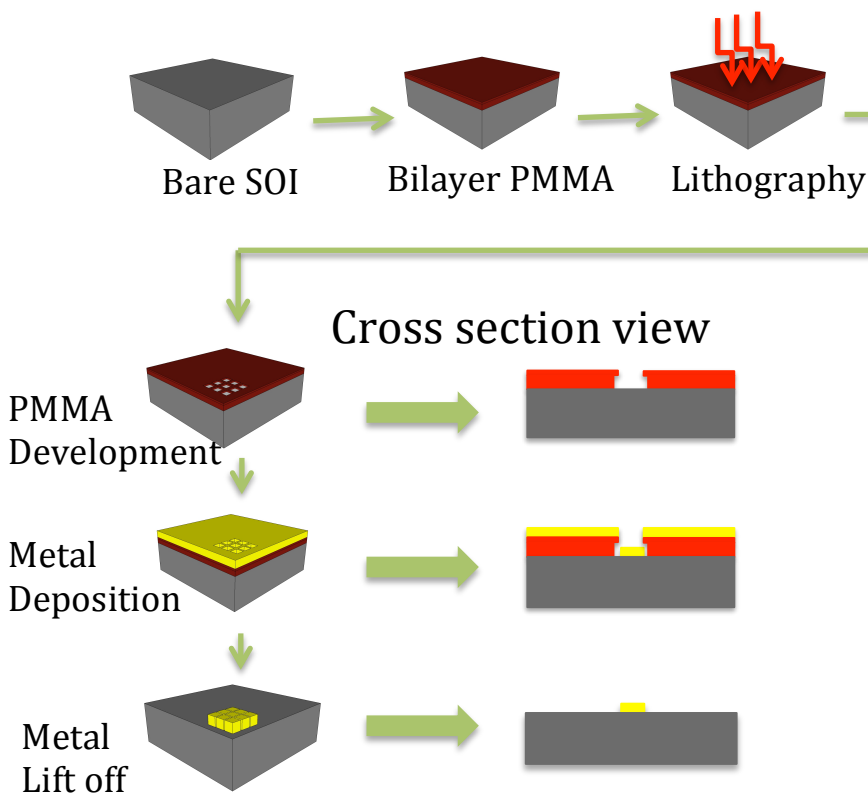


Figure 3.5: Process flow for fabrication of alignment markers.

### 3.5.2 Waveguide definition

The waveguide has been designed using optimized modelling specifications in Chapter 2. It is crucial for the device waveguide to have very stringent specification at nanometre scale precision. In the following sub-section, further thorough processes are presented due to its essential elements to realize the functional device. Figure 3.6 shows simplified preparation processes during device fabrication.

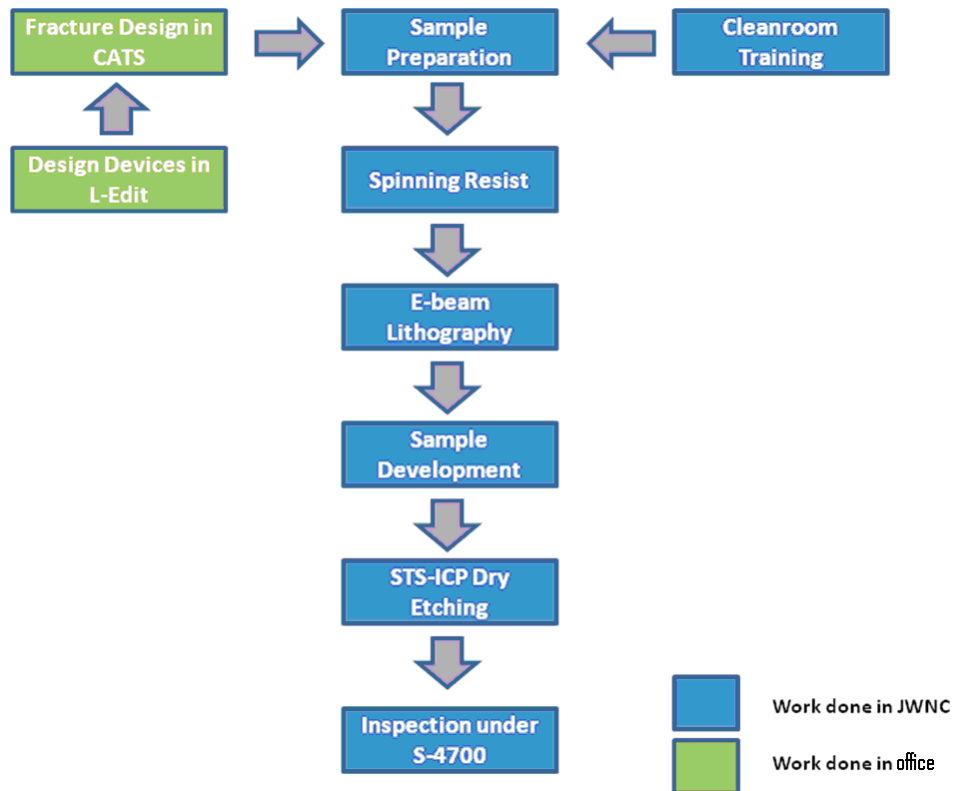


Figure 3.6: Process flows of pattern definition when using EBL.

### 3.5.2.1 CAD Layout

The device was designed using Tanner EDA L-Edit software, a layout editor commonly used for lithography. This is due to its capabilities to define different layers corresponding to different materials on the same layout during the fracturing stage. The VB6 is calibrated to operate at resolutions of  $0.5\text{ nm}$ ,  $1\text{ nm}$  and  $1.25\text{ nm}$ . The minimum grid size is set to  $1.25\text{ nm}$  to give maximum writing field [3.10].

Although the grid size or resolution was set to  $1.25\text{ nm}$ , the minimum EBL spot size (SS) is 3 to  $4\text{ nm}$ . The patterned was written in the set of circular points and the distance the two circular points is defined as beam step size (BSS). The relationship between these three factors can be illustrated in Figure 3.7.



Figure 3.7: Illustrate the relationship between beam spot size (BSS), resolution and spot size (SS).

### 3.5.2.2 Fracturing & Proximity Effect Correction

The pattern was designed using a well-known commercial layout design editor software, L-Edit from Tanner EDA. The design file then was exported to Graphic Database System II (GDSII) file format. Next, the EBL layout editor Layout Beamer software from GenISys was used to fracture the GDSII file. The design pattern that consists of exposed regions was ‘fractured’ into small trapezia in a period grid that corresponds to the  $1.25\text{ nm}$  resolution set earlier.

During EBL process, the electron gun generates a high energy beam at a suitable current density. The lenses are used to sharply focus the beam and scanned over the surface material. The electron beam energy for the VB6 was set at either 50 or 100 eV. These high-energy electrons causes electron to scatter through the resist and substrate as shown in Figure 3.8. The scattered high-energy electrons affect the exposure dose distribution where the developed pattern is wider than the scanned pattern. The interaction between the resist and the substrate cause the primary beam electrons scattered outside the scanned pattern. This occurrence is known as the proximity effect and limits the size of exposed regions and in particular their proximity to other patterns. [3.20] In Layout Beamer, the proximity effect correction function was chosen to decrease this effect by adjusting the dose in the patterns.

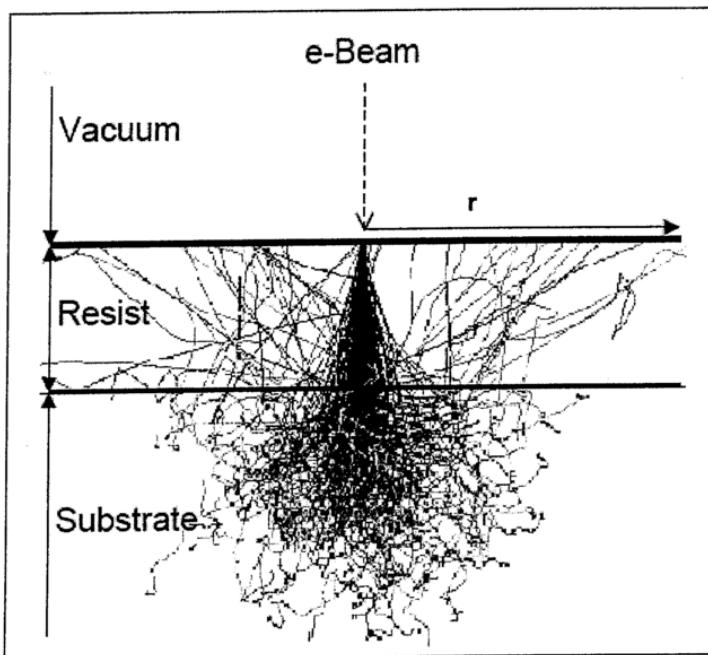


Figure 3.8: Schematic illustrates the cross section of the resist and substrate during EBL process. 'r' is the lateral distance that secondary electrons have scattered through the resist and the substrate [3.21].

### 3.5.2.3 E-beam Resist, EBL Exposure, Development

As mentioned earlier, there are positive and negative tone resists. It is important to select the proper tone as the wrong tone can drastically increase the writing time. In this case, positive tone resist contribute to long writing time due to the larger features to be patterned. Therefore, negative tone resist is preferred. In the JWNC, option of negative e-beam resist includes NEB31 from Sumitomo and Hydrogen Silsesquioxane FOX16 (HSQ) from Dow Corning. Characteristics of both NEB31 and HSQ are presented in Table 3.1 for comparison.

E-Beam Resist	NEB31	HSQ
Dose Level	Low Dose	High Dose
Resolution	High resolution for 30 nm features	Ultra high resolution for sub 10 nm features
Dry Etch process	Normal negative tone	Hard negative tone (good for dry etch resistance)
Issues	Chemical-amplified resist, temperature is CRITICAL	Development creates bubbles could cause under-develop
Cost GBP (£) per litre	5000	3564

Table 3.1: Table presents the characteristics of negative tone e-beam resist of NEB 31 and HSQ.

HSQ was chosen due to its ultra high resolution and high dry etching resistance [3.11]. HSQ molecules arranged in a cage structure structures that consist of hydrogen, silicon and oxygen bonds (H-Si-O). EBL exposure breaks Si-H bonds and leaves Si-O bonds causing crosslinking similar to silica structures.

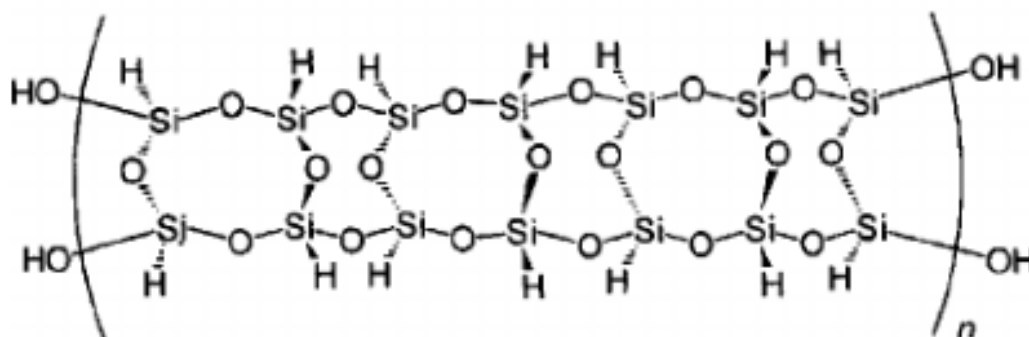


Figure 3.9: HSQ structure [3.22].

HSQ was initially diluted with Methyl isobutyl ketone (MIBK) at 1:1 ratio in a vial. The dilution was prepared fresh and used on the same day. It is noted that day old HSQ dilution can affect device features, which could hinder reproducibility [3.11]. HSQ

was spun on the chip at  $3000 \text{ rpm}$  for  $60 \text{ seconds}$ , which yields resist thickness of  $220 \text{ nm}$  [8]. The chip was baked at  $90^\circ\text{C}$  in a vacuum hotplate for 2 minutes. Several dose tests were carried out to find best EBL exposure specifications. EBL exposure parameters used for the device waveguides were;  $1500 \mu\text{C}/\text{cm}^2$ , Variable Resolution unit (VRU) 4 and spot size of  $9 \text{ nm}$ . During the dose test, the cutoff dose for such structures ranged from  $1300$  to  $1500 \mu\text{C}/\text{cm}^2$ , with the same parameters used.

The development process was carried out in a laminar fume cabinet with TetraMethyl Ammonium Hydroxide (TMAH) at  $25\%$  concentration in water used as a resist developer. The temperature was set to  $23^\circ\text{C}$  at all times to remove the unexposed resist. To reduce bubbles during the development process, the wafer chip was agitated and rinsed twice with RO water in two different beakers. Next it was further cleaned with IPA. The development with TMAH, the double rinsing with RO water and IPA are performed for  $30 \text{ seconds}$  each.

For large structures, the pattern usually is divided into several writing fields. Stitching errors can occur for such structures if different resolutions were used for writing large or small structures. This results from the accuracy of the line scanned during EBL. In addition, stitching errors also depends on the resist and doses used, which affect the back-scattered electrons during EBL. The stitching errors can be eliminated or reduced by maintaining the same resolution and dose for the same structure. Moreover, the backside of the chip must be cleaned to ensure there is no dried residual resist. This is to ensure the flatness of the chip during writing. In addition, double clamps can be useful to further improve the flatness of the chip.

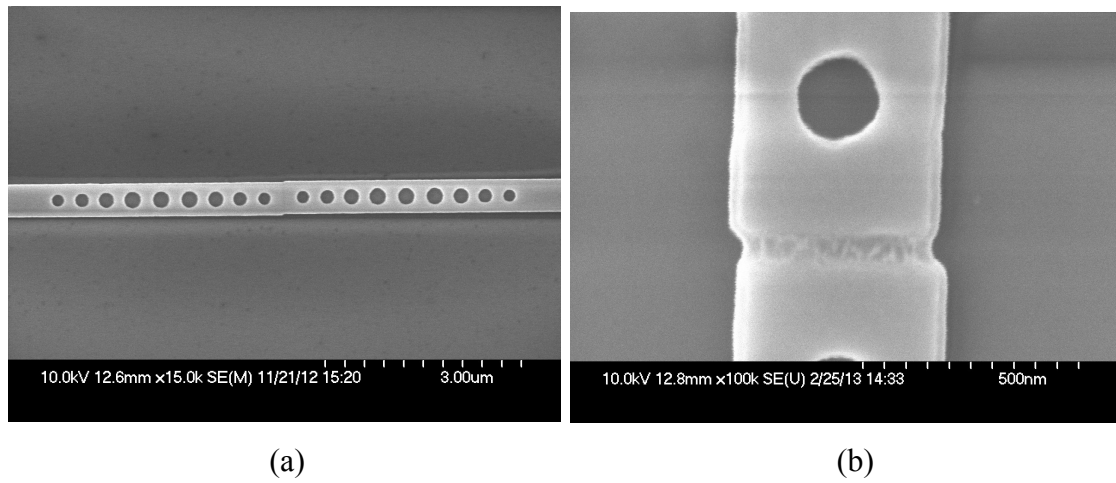


Figure 3.10: SEM pictures of a waveguide with stitching error in the horizontal direction (a) and combination of vertical and horizontal direction (b) during EBL writing.

### 3.5.2.4 Silicon Dry Etching

The next fundamental step after the resist pattern has been transferred onto the chip is to transfer the pattern into the core (silicon) layer. This is achieved using dry etching where the unmasked area is removed by physical and chemical attack. Dry etching is preferable to wet etching due to uniformity of the structures and vertical sidewalls (anisotropic etch).

Once the pattern of resist has been transferred onto the silicon layer, the chip is dry-etched using Reactive Ion Etching – Inductive Couple Plasma (STS-ICP) machine from Surface Technology System available in JWNC. The reactive plasma chemically generates high-energy ions under vacuum condition. These high-energy ions attack the surface of the material forming volatile products, therefore removing the patterned areas.

The dry etching of the silicon layer using STS-ICP machine consists of combination gases of SF<sub>6</sub> – C<sub>4</sub>F<sub>8</sub>. In this process, the vertical sidewalls are produced by non-reactive mask film, and the horizontal surface is exposed. In the machine's chamber, alternating gases produce an alternating etching and passivation process. The silicon etching gas is SF<sub>6</sub> while the passivation gas is C<sub>4</sub>F<sub>8</sub>. The C<sub>4</sub>F<sub>8</sub> gas in the plasma was deposited on the silicon surface prevent the fluorine from the SF<sub>6</sub> to further etching the silicon. The etching and passivation gas alternate every 5 seconds during the cycle. The

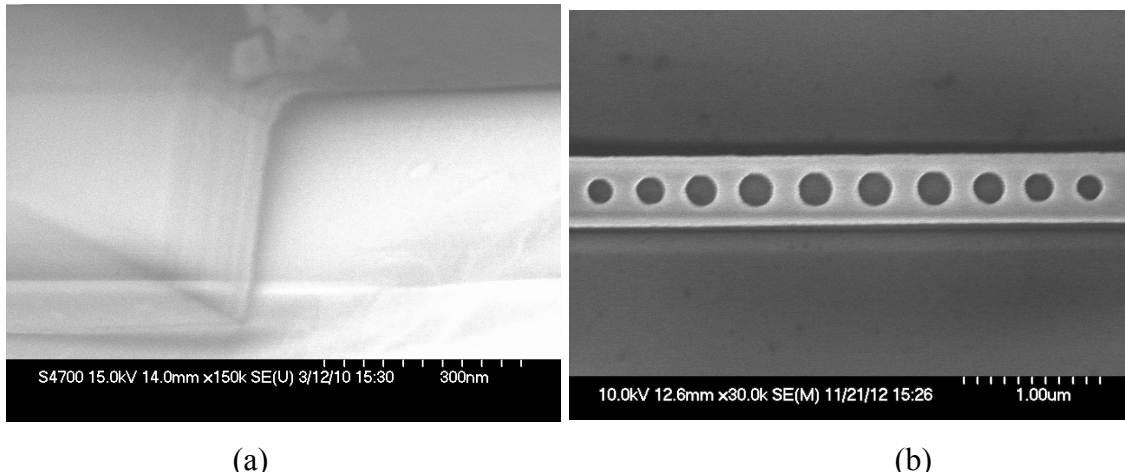
combination of alternating cycles prevent the ions from sputtering the etched the silicon sidewalls [3.13].

The above process has been previously described [3.14], however, further improvement are needed to fabricate the Bragg mirror holes according to specification.. The Bragg mirror holes in the waveguides must have smooth sidewalls to prevent variation of the effective index, which can change the mode distribution of the guided light. The parameters used in this work are listed in Table 3.2.

Parameter	Value	
Gas	SF <sub>6</sub>	C <sub>4</sub> F <sub>8</sub>
Flow (SCCM)	30	80
Platen Power (W)	12	
Coil Power (W)	600	
Pressure (mT)	10	
Etch Rate (nm/min)	120	

Table 3.2: Parameters of silicon waveguide dry etch process using RIE ICP machine.

The etch time of the process to define the silicon waveguide was tested at one, two, and three minutes. It is known that increasing the etching time will increase the etch depth. At the shortest time (*1 minute*), the holes may not be fully etched since it is difficult for the ions to penetrate through the small gap. Meanwhile, at the longest etching time (*3 minutes*), the holes have been fully etched [3.14], but longer etching time may result in damage of the mask edges, thereby changing the geometry of the waveguides. Therefore the etching time for defining the silicon waveguide layer was set to two minutes.



(a)

(b)

Figure 3.11 SEM pictures of over etched silicon waveguide damages the resist mask and over-etches to the silica layer, however the surface roughness of the sidewall is smooth and acceptable (a), while (b) shows fully etched Bragg mirror holes in the silicon waveguide.

### 3.5.3 Silicon Membrane

By removing the silica cladding on SOI, it is possible to increase Q factor of the cavity and its sensitivity to refractive index change [3.15]. This is because the confined mode in the silicon waveguide will be surrounded by air providing a high index contrast thereby increasing the confinement and Q factor. In addition, the active areas on both top and bottom side are exposed to the analyte.

In order to remove silica cladding, a 15 % PMMA 2010 resist was spun on the chip to a thickness of 1200 nm. An EBL exposure and development was carried out to create a window for membrane definition (Figure 3.12).



Figure 3.12: Optical micrograph of PMMA window mask (dark rectangles) on the chip for membrane definition.

The chip was immersed in Hydrofluoric Acid (HF) 5:1 ( $\text{H}_2\text{O:HF}$ ) ratio for 1 minute. The wet etching rate was measured at 10-13 nm/s. Because HF can easily etch silica and wet the surface therefore, the chip must be placed under running RO water for at least 5 minutes to remove the remaining HF. Finally, the chip was thoroughly blown dry using nitrogen gun.

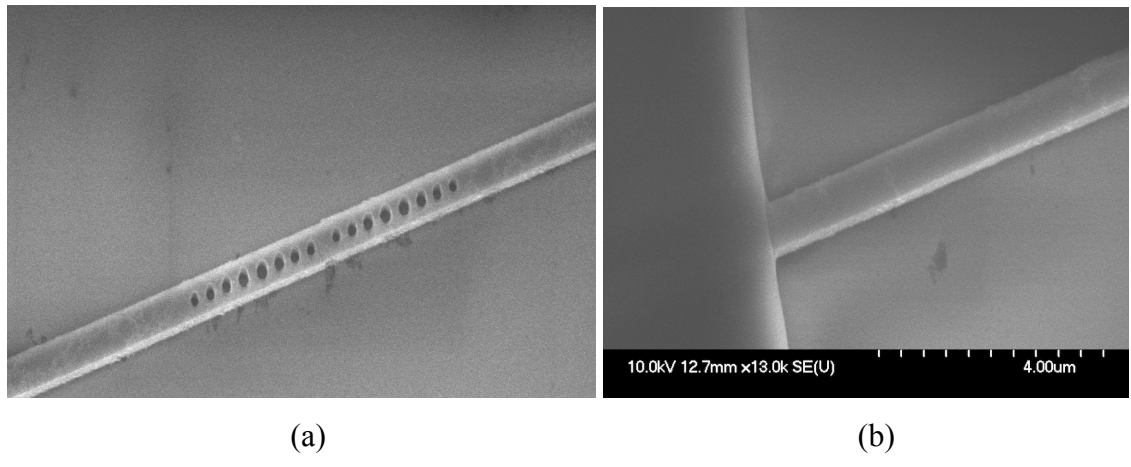


Figure 3.13: SEM pictures of etched silica beneath the waveguide device. (a) Birds eye view and (b) shown from the end of the suspended waveguide.

## 3.6 Waveguide Coupling

Among the features that need to be considered when using silicon based waveguides are input and output light coupling into the device. This includes coupling efficiency, planar geometry of the end facets, noise per dB and equipment available in the lab. In this work, we explored two different approaches to couple light into the devices.

### 3.6.1 Adiabatically tapered coupling method

To attain single mode profile in a  $500\text{ nm}$  width device waveguide, the coupling feeder waveguide is adiabatically tapered along  $600\text{ }\mu\text{m}$  at  $7^\circ$  angle connected to the input waveguides of  $2\text{ }\mu\text{m}$  width at both ends as shown in Figure 3.15. Since the feeder coupling waveguides have larger features than the device waveguides, it was written in different layer in L-Edit in order to reduce the writing time. However, this can induce misalignment, due to stitching errors during e-beam writing.

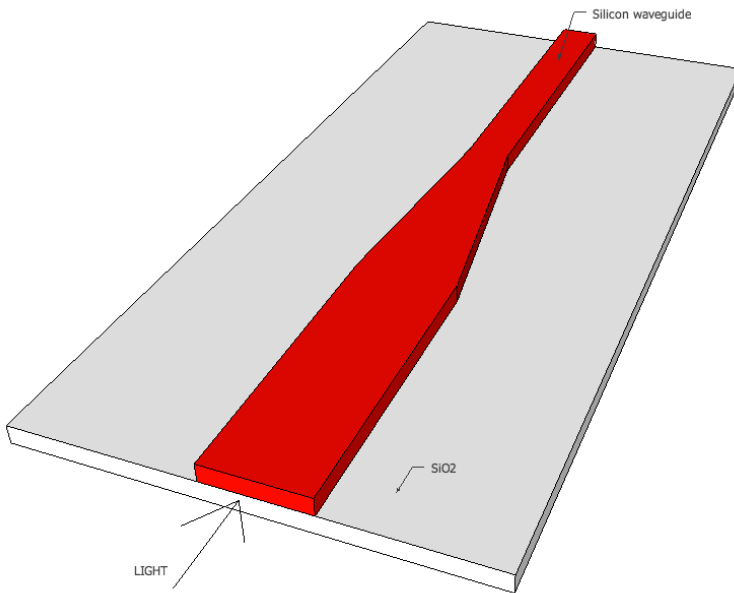


Figure 3.14: Schematic design of coupling feeder and device waveguides.

The advantage of having the adiabatically tapered coupling waveguide technique is that it can be written and etched with the device waveguide using the same process while maintaining the single mode operation. In addition, it is easier to do characterization and measurement on the device without the need of alignment markers. Nonetheless, characterization measurements suffer from Fabry-Perot effects. The presence of strong Fabry-Perot oscillations is due to reflectivity of the end facets forming a cavity.

### 3.5.2 Planar inverted tapers with low index polymer block coupling method

The adiabatically tapered coupling method resulted in strong Fabry-Perot oscillation effects. This strong oscillation can affect the resonance wavelength result. To reduce the strong oscillations we explore another option. The method of coupling light using the block polymers and inversely tapered the device waveguides has been used elsewhere [3.16, 3.17].

The material used must have a lower refractive index than silicon. SU-8 resist is suitable because it can be directly written and beyond a wavelength of 400 nm, the transmission is greater than 95 %, indicating that SU-8 is optically transparent at the telecommunications wavelengths of 1330 nm and 1550 nm. This shows that SU-8 is a suitable material for optical waveguides [3.18].

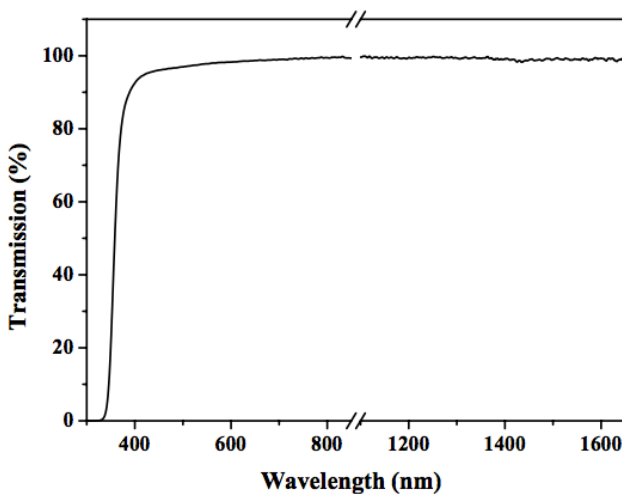


Figure 3.15: Graph shows transmission spectrums versus wavelengths of SU-8 resist from 350 to 800 nm (visible light range) and 1200 to 1600 nm (mid infra red). [3.18]

The idea is to cover the silicon waveguide narrow tip with the relatively larger waveguide of SU-8 polymer. Silicon (index of 3.49) has comparatively higher index than SU-8 (index of 1.52) waveguide. The light from the fibre travels to the large cross-section of low index SU-8 waveguide. The narrow silicon tip creates a gradual change of low to high effective index. Once the mode fully converted to higher index waveguide (silicon), the SU-8 waveguide can be neglected. The transformation of the mode from lower to higher or vice versa is bi-directionally efficient [3.19]. Hence, the coupling method is also applied to an output region. Ideally, the end tip would be zero width, however, we set the cross-section of the tip to 50 nm and a taper length of 300  $\mu$ m. The SU-8 polymer waveguides dimension are 1 x 1 x 20  $\mu$ m (W x H x L).

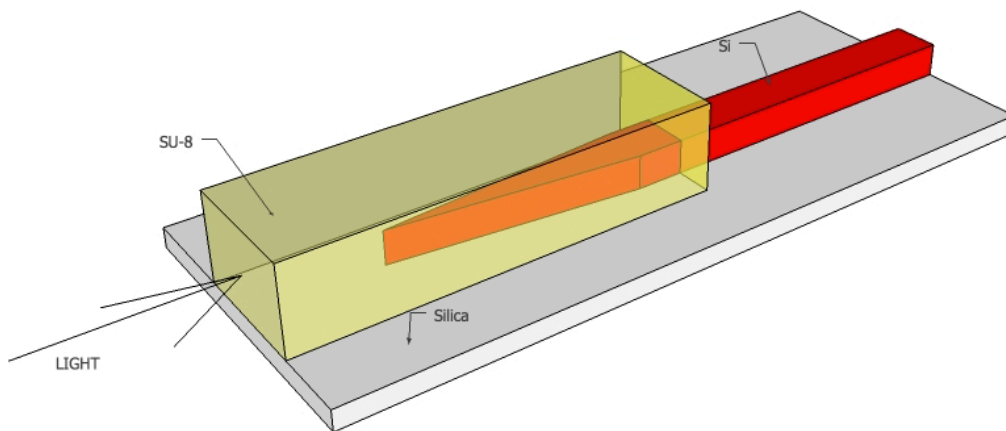


Figure 3.16: Schematic of the waveguide with SU-8 polymer block for input and output coupling. The waveguide device was depicted in red and is planar inverse tapered down to a narrow tip. A transparent block of SU-8 polymer covered the input and output waveguides.

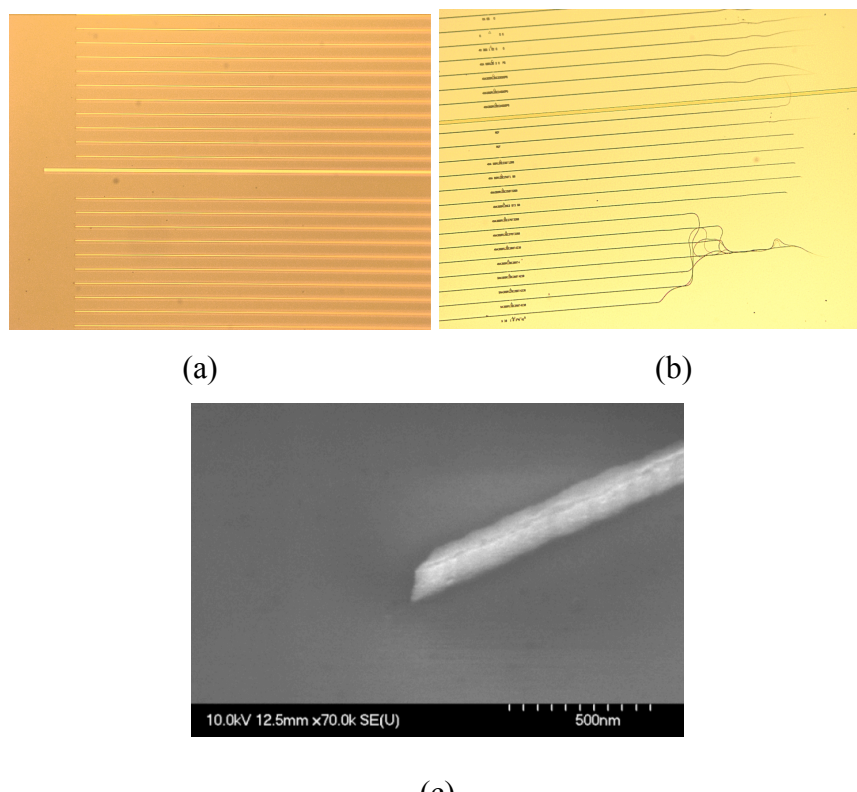


Figure 3.17: Optical micrographs of HSQ pattern after development with (a) and without (b) oxygen plasma ashing surface modification. Without the surface modification, HSQ suffers serious adhesion problem towards the end of the tip (c) SEM micrograph of silicon end tip after dry etching.

The SU-8 polymer waveguide is fabricated as follows: The SU-8 2002 (Microchem Corp) resist is pipetted out on top of the device chip and is spun at 2000 rpm for 30 *seconds*. The chip is placed on the hot plate for 1 *minute* at 95 °C. Next, the chip went through an EBL job for patterning. The chip is developed using EC Solvent for 1 *minute* and rinsed with a fresh EC Solvent for 20 *seconds* and IPA for 2 *seconds* to remove the development debris.

Although the fabrication of the polymer waveguide is straightforward, a test sample is need for the dose test and device inspection measurement. At high dosage, the SU-8 may cause additional cross-linkaging causing surface roughness. The advantages and the disadvantages using SU-8 as coupling method are shown in the table 3.3 in below.

Advantages	Disadvantages
The material is optically transparent at the targeted wavelengths. The polymer waveguides improve coupling efficiency, lower power usage; hence two photons absorption is avoided.	The SU-8 polymer feeder waveguide is temperature dependent. The material cannot withstand to elevated temperature for period of time.

Table 3.3: Table shows the advantages and disadvantages of using SU-8 as polymer waveguides feed into and out of the device.

### 3.7 Overall device design

Generally, the device and the coupling feeder waveguides are designed and cleaved at 3 to 4 mm in length, however, microfluidic channel system must be considered. Therefore, the chip is cleaved at 8 to 12 mm width to accommodate the microfluidic channel.

Finally, the device chip is ready to be characterized and analysed. Fabrication of the microfluidic channels will be further review in Chapter 5.

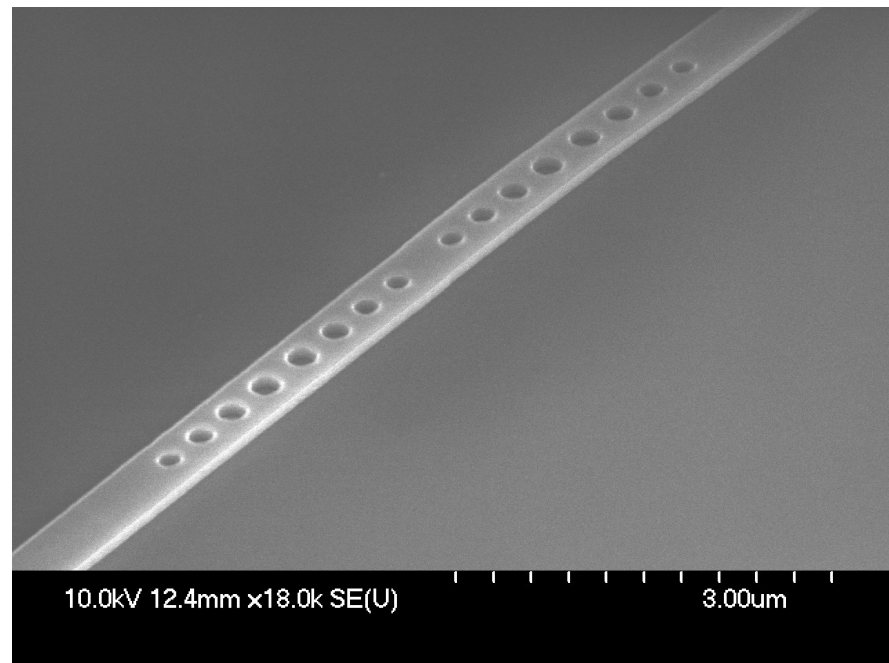


Figure 3.18: SEM pictures of the fabricated silicon waveguide.

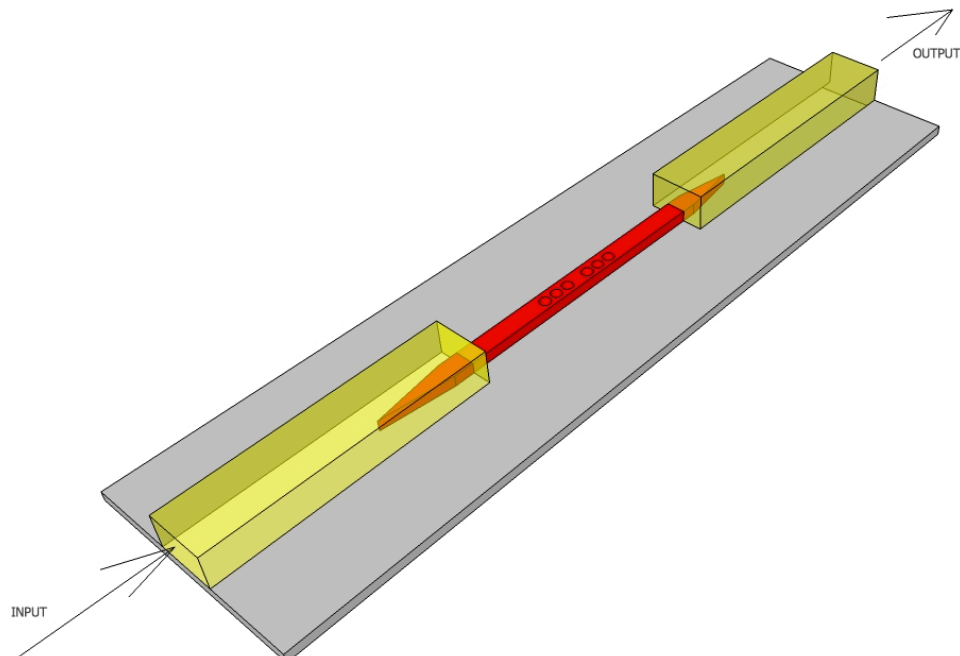


Figure 3.19: Picture illustrated the design of complete feeder and device waveguide.

## 3.8 Conclusions

To ensure the high quality of the device chip, all fabricated structures must be inspected thoroughly either by using optical microscope or SEM machine after each critical steps during fabrication. These critical steps include the work during EBL, development and etching process.

The device was fabricated using both positive and negative tone e-beam resists for the planned specification. Hence, alignment marks were used to attain multiple step e-beam jobs. Defining the silicon waveguide devices is considered very crucial; hence the work must be done cautiously. This is due to presence of mirror holes and waveguides sidewalls that determine the effective index of the travelling mode. Slight changes on the dimensions would compromise the resonance wavelengths specification.

The waveguides devices are coupled either by adiabatically tapered waveguides or using inverse taper waveguide with polymer block. However, the later method is preferable due to many advantages. The main reason is to avoid the strong Fabry-Perot oscillations on the measurement data.

Fabrication tolerances are about 1-2 nm based on the mirror size measured. Although this may affect the wavelengths resonance location, however most of the measurements are based on the resonance shifts. To optimize the fabrication process, time and effort must be devoted to explore better techniques. All the apparent factors such as machine, environment and human factors must be considered. In the next chapter, the chip device is characterized and analysed.

## References

- [3.1] Muneeb, Muhammad, Xiaohui Chen, Eva Ryckeboer, Aditya Malik, Goran Z. Mashanovich, and Günther Roelkens. "Silicon-on-insulator mid-infrared planar concave grating based (de) multiplexer." In *IEEE Photonics Conference (IPC-2013)*, pp. 100-101. (2013).
- [3.2] Song, Jong Hyun, Russell A. Budd, Byeong Lee, Clint L. Schow, and Frank R. Libsch. "Focusing grating couplers in unmodified 180-nm Silicon-on-Insulator CMOS." *Photonics Technology Letters, IEEE* 26, no. 8 (2014): 825-828.
- [3.3] Sumikura, Hisashi, Eiichi Kuramochi, Hideaki Taniyama, and Masaya Notomi. "Enhanced electron-hole droplet emission from surface-oxidized silicon photonic crystal nanocavities." *Optics Express* 24, no. 2 (2016): 1072-1081.
- [3.4] Mirza, M. M., P. Velha, G. Ternent, H. P. Zhou, K. E. Docherty, and D. J. Paul. "Silicon nanowire devices with widths below 5 nm." In *Nanotechnology (IEEE-NANO), 2012 12th IEEE Conference on*, pp. 1-4. IEEE, (2012).
- [3.5] SOITEC Smart-Cut technology (online)  
<http://www.soitec.com/en/technologies/smart-cut/>
- [3.6] Adrega, T., and S. P. Lacour. "Stretchable gold conductors embedded in PDMS and patterned by photolithography: fabrication and electromechanical characterization." *Journal of Micromechanics and Microengineering* 20, no. 5 (2010): 055025.
- [3.7] Heuberger, A. "X-ray lithography." *Journal of Vacuum Science & Technology B* 6, no. 1 (1988): 107-121.
- [3.8] Cheng, Wen-Hao, and Jeff Farnsworth. "Fundamental limit of ebeam lithography." In *Photomask and Next-Generation Lithography Mask Technology XIV*, pp. 660724-660724. International Society for Optics and Photonics, (2007).

- [3.9] Watt, F., A. A. Bettoli, J. A. Van Kan, E. J. Teo, and M. B. H. Breese. "Ion beam lithography and nanofabrication: a review." *International Journal of Nanoscience* 4, no. 03 (2005): 269-286.
- [3.10] Stephen Thoms, e-beam course note (2009).
- [3.11] O'Faolain, Liam, M. V. Kotlyar, N. Tripathi, R. Wilson, and T. F. Krauss. "Fabrication of photonic crystals using a spin-coated hydrogen silsesquioxane hard mask." *Journal of Vacuum Science & Technology B24*, no. 1 (2006): 336-339.
- [3.12] Henschel, W., Y. M. Georgiev, and H. Kurz. "Study of a high contrast process for hydrogen silsesquioxane as a negative tone electron beam resist." *Journal of Vacuum Science & Technology B* 21, no. 5 (2003): 2018-2025.
- [3.13] Nojiri, Kazuo. *Dry etching technology for semiconductors*. Springer, (2015).
- [3.14] Marco Gnan, "Photonic Wire Devices in Silicon-on-Insulator," Ph.D.dissertation, University of Glasgow, (2007).
- [3.15] A. R. Zain , N. P. Johnson , M. Sorel and R. M. De La Rue, "High quality-factor 1-D-suspended photonic crystal/photonic wire silicon waveguide microcavities", *IEEE Photon. Technol. Lett.*, vol. 21, no. 24, pp. 1789-1791, (2009).
- [3.16] Wahlbrink, Thorsten, Wan Shao Tsai, Michael Waldow, Michael Först, Jens Bolten, Thomas Mollenhauer, and Heinrich Kurz. "Fabrication of high efficiency SOI taper structures." *Microelectronic Engineering* 86, no. 4 (2009): 1117-1119.
- [3.17] Shoji, T., T. Tsuchizawa, T. Watanabe, K. Yamada, and H. Morita. "Low loss mode size converter from 0.3  $\mu\text{m}$  square Si wire waveguides to single mode fibres." *Electronics Letters* 38, no. 25 (2002): 1669-1670.

[3.18] Microchem Corp (online)

<http://www.microchem.com/Appl-IIIVs-Waveguides.htm>

- [3.19] Roelkens, Günther, Pieter Dumon, Wim Bogaerts, Dries Van Thourhout, and Roel Baets. "Efficient fiber to SOI photonic wire coupler fabricated using standard CMOS technology." In *Proceedings of the 18th Annual Meeting of the IEEE Lasers & Electro-Optics Society (LEOS 2005)*. (2005).
- [3.20] Chang, T. H. P. "Proximity effect in electron-beam lithography." *Journal of Vacuum Science & Technology* 12, no. 6 (1975): 1271-1275.
- [3.21] Belic, Nikola, and Hans Eisenmann. "Method for electron beam proximity effect correction." U.S. Patent 7,638,247, issued December 29, (2009).
- [3.22] Shih, W-Y., J-H. Zhao, A. J. McKerrow, E. T. Ryan, K. J. Taylor, and P. S. Ho. "Thermomechanical Properties of Hydrogen Silsesquioxanes." In *MRS Proceedings*, vol. 476, p. 173. Cambridge University Press, (1997).

# Chapter 4 Photonic Crystal Nanocavities

- 4.1 Introduction
  - 4.2 Photonic Crystal nanocavities
  - 4.3 The design
    - 4.3.1 Period and cavity
    - 4.3.2 Mode matching and optimization
    - 4.3.3 Earlier results
  - 4.4 1-D PhC nanocavity working at 1550 nm
    - 4.4.1 Cavity length arrangement
    - 4.4.2 Mirror strength
  - 4.5 1-D PhC nanocavities membrane
  - 4.6 Conclusion
- References

## 4.1 Introduction

This chapter starts with a brief historical review on the discovery of photonic crystal followed by discussion on the basic building block of the PhC nanocavities with regards to the properties of the material used, the design and device measurements. Highlights of the design, the modal adaptation principles, the limitation during the project and the solutions adopted are also explained.

## 4.2 Photonic Crystal Nanocavities

As mentioned in Chapter 1, Photonic Crystals (PhCs) have been widely used in the research of photonics. Since their first discovery in 1987 by Yablonovitch [4.1] and John [4.2], the Bragg mirror concept of periodic variation of refractive index has been intensely explored. They proposed the 3D photonic crystal as the platform for a complete bandgap. In addition, high Q cavities over the mode volumes are desirable to confine for a variety of devices including sensors. However, to date the fabrication of the 3D PhC with high Q structures are extremely challenging [4.3]. This leads researchers to opt for different approaches using less complicated structural properties such as 2D or 1D PhC structures.

Initially, 2D PhCs became more of interest because of their relative ease of fabrication and compatibility to the current CMOS technology. 2D PhC cavities with Q factors of  $> 10^6$  have been achieved by Noda's group [4.4]. More research were conducted using numerous optical applications based on 2D PhC cavities [4.5 - 4.7]. Nevertheless, the 1D PhCs cavity structure is also relevant due to its capability to exhibits the same high Q factor values, with smaller geometric footprint than 2D and 3D PhCs. The idea of 1D PhC cavity was introduced by Foresi et al [4.8] in 1997. They used an approach of drilling periodic holes in a silicon optical waveguide with an extra spacer in the middle that acts as the cavity. However, the quality of the 1D PhC microcavities was poor and only been perfected in 2007 by Velha et al [4.9] and subsequently by Md Zain et al [4.10] whereby their devices able to reach the Q factors  $> 10^6$ . With this breakthrough, many optical applications and features such as optical switching [4.11],

bistability [4.12] and more were accomplished.

The high Q 1D PhC nanocavity also makes it an ideal candidate to be used as an optical sensor. The trapped light is confined and cycled in the high Q PhC nanocavity. This phenomenon enables the optical sensor to have more interaction with the analyte in the cavity region. During the light lifetime in the cavity, the light is bounce back and forth between the Bragg mirrors interface and interacts with the analyte.

## 4.3 The Design

One of the key elements in the design of 1D PhC nanocavities for optical sensing is the capability to tune the position of the resonance of the devices while still producing the high Q values. The shifts of the resonance wavelengths peak is achieved by taking advantage of the ability to change the effective indices of the PhC optical waveguides at the cavity region. Therefore, the design of an effective high Q PhC waveguide device is crucial for developing an efficient optical sensor.

The material of the devices, SOI has been briefly discussed in section 3.2. The SOI consist of silicon layer as the guiding layer with a nominal thickness of  $220\text{ nm}$  sits on the silica buffer layer of  $2\text{ }\mu\text{m}$  thickness. The working optical waveguide confines light at the guiding layer. The basic building block of the optical waveguide is to support single mode propagation. It has been noticed that the width of the optical waveguide can be varied, however, a  $500\text{ nm}$  width is preferable because of the low loss feature while still supporting single mode propagation at a wavelength of  $1.55\text{ }\mu\text{m}$  [4.13].

In this project, the design of the 1D PhC nanocavities initially was adapted from the design of Foresi et al [4.8]. The devices consist of drilled periodic holes that act as Bragg mirrors. Light trapping was achieved using Bragg scattering and Total Internal Reflection (TIR). This resulted in an optical resonance when a spacer (cavity) is introduced between the Bragg mirrors. The Q value was very low because of the huge scattering losses. When dealing with scattering losses in PhC cavity, it is important to consider that the fields do not abruptly terminate at the mirror boundary [4.14]. In

addition, the mismatch in the effective index mode of the pattern (mirror holes) and unpatterned (optical waveguide) resulted in the low Q values.

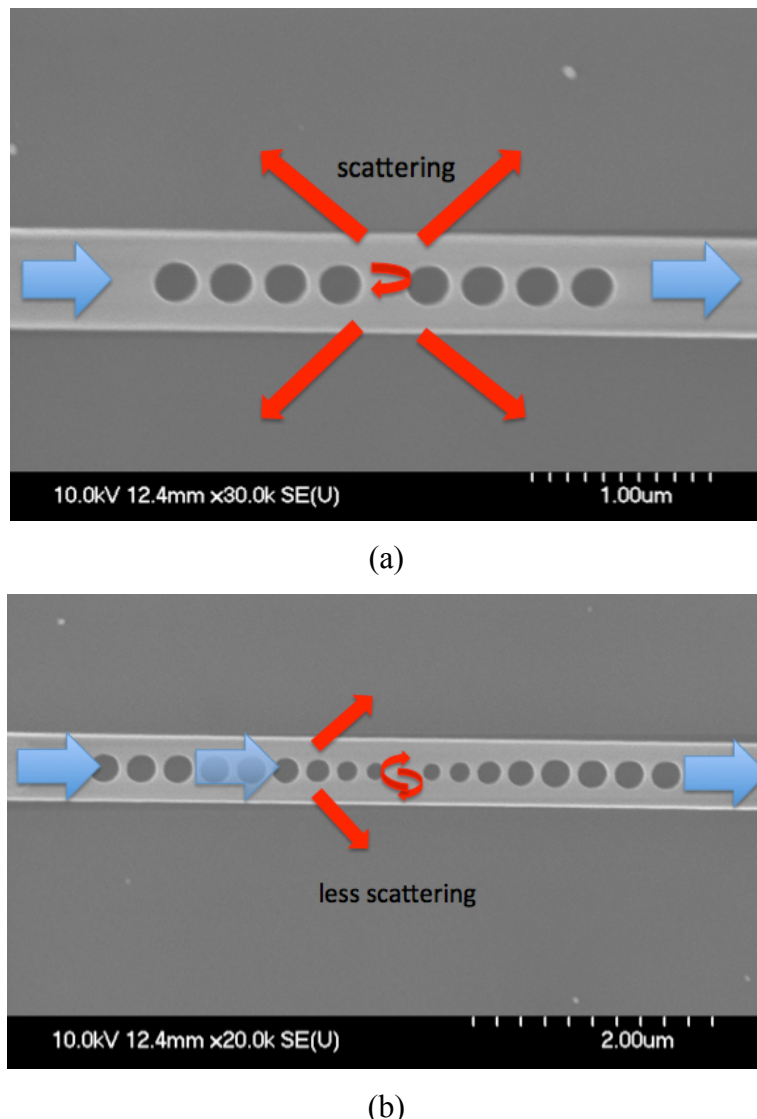


Figure 4.1: Images illustrating (a) light scattering loss inside the waveguide cavity region resulting in the poor Q factors while (b) less scattering effects when tapering mirrors holes were added inside the cavity. The light blue arrows show the light propagation directions.

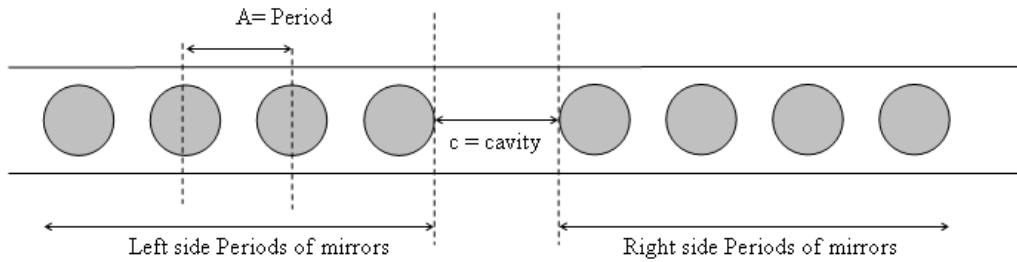


Figure 4.2: Basic design of 1D PhC cavity structure consists of periodic mirrors separated by a cavity.

### 4.3.1 Period and Cavity

Similar to 2D PhC cavity structures, the period,  $A$  is realised with a combination of photonic bandgap (PBG) and TIR. For 1D PhC structures, the periodic pattern of the lattice constant of high (silicon) and low (mirror holes) index material. The period is determined in one dimension only, for example; the x direction is the direction of light propagation while the width and thickness are in y and z directions respectively. The wavelength of the Bragg mirror or PBG is dependent to the refractive index and the period,  $A$ . While increasing the numbers of period,  $N$  will increase the reflection of light at the stop band [4.15].

$$\lambda = 2 n_{\text{eff}} A \quad (\text{Eq. 4.1})$$

Another essential of the PhC optical sensor is the creation of a point of defect or cavity. This is the area where most of the active region of the sensor interacts with the analyte. It is reported in the literature that cavity can be created by simply changing the spacing between a pair of holes [4.16]. This basically creates two sets of Bragg mirrors from one shown in Figure 4.2. The spacing between the pair of holes creates a cavity region, which then alters the effective index of the waveguides. The cavity is affecting the mode to be pulled into the PBG. It is also noted that the spacer or cavity length is important in determining the quality factor of the PhCs. Variation in the cavity length allows the formulation of the high Q values. This is based on mode matching in the cavity length area. In Figure 4.3, 2D FDTD computations were simulated based on 6 periods of Bragg mirrors ( $N=6$ ), mirror radius,  $r$  of 100 nm and variation of period length,  $A$

between 300 and 360 nm.

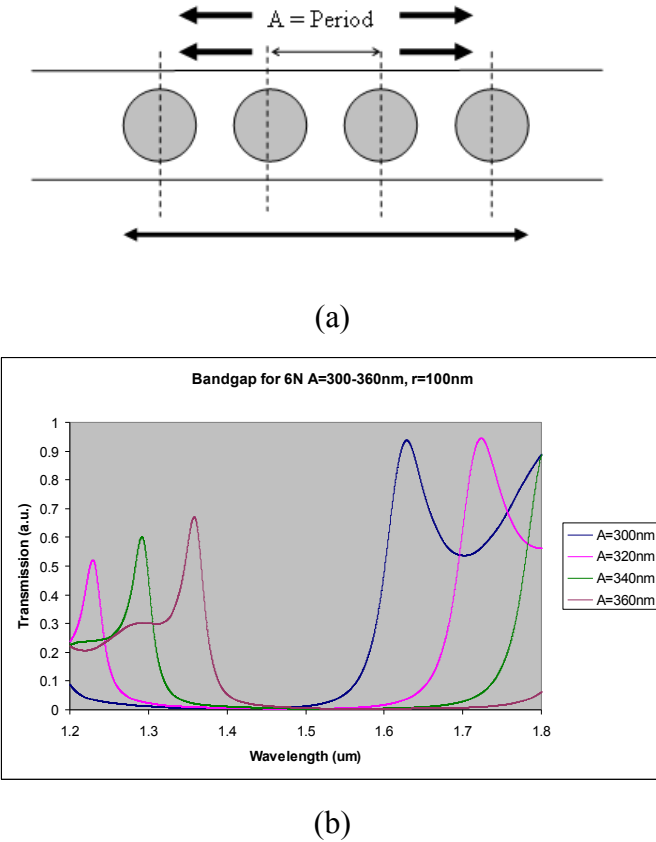


Figure 4.3: 2D FDTD computations of pass and stop bands (a) varying the period length on the middle of the Bragg mirrors (b) Bandgap of 6 period Bragg mirrors ( $N = 6$ ) with various period length.

### 4.3.2 Mode matching and optimization

It is crucial to keep the scattering losses and mode mismatch in the cavity to bare minimum when designing 1D PhC nanocavity devices. The mode matching for the propagating mode is similar to the impedance matching problem in electronics. The idea was to introduce tapering holes inside the cavity. The tapering holes help a smooth transition mode between the unpatterned cavity and Bragg mirror holes. The tapering technique is necessary for the propagating mode of the cavity to create exponential decay into the Bragg mirrors. This can be achieved with multiple tapering holes. The Bragg mirror mode is slowly matched with the cavity mode [4.17]. This will increase the life cycle of the energy stored in the cavity. Therefore, the scattering losses are significantly

reduced while the Q value is exponentially increased (refer to Figure 4.4 (b)).

### 4.3.3 Initial Results

The designed structure was given  $A = 3.2r$  where  $r$ , radius is  $100\text{ nm}$ . The cavity was set at  $220\text{ nm}$ . The device was targeted to be centred at a wavelength of  $1310\text{ nm}$ . Using 2-D FDTD computation, first taper holes were introduced with various displacements. The displacement was measured from the furthest (e.g. the period length) to the nearest possible Bragg mirror. The highest Q factor values were noted at an optimum tapering displacement.

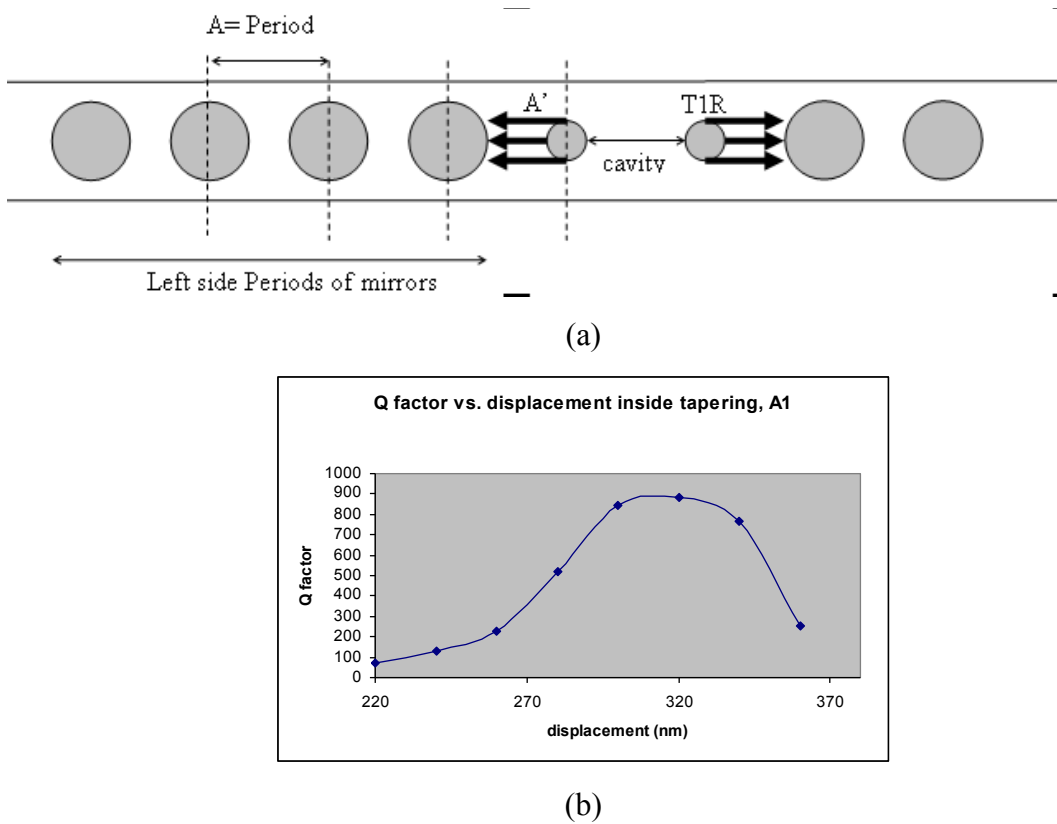


Figure 4.4: The tapering technique, (a) First tapering holes inside the cavity (b) 2D FDTD computed results of Q values of single tapering holes inside the cavity with various tapering hole displacement.

Next, using the same technique, multiple tapering holes were introduced to creates an adiabatically conversion of the propagating modes. The high Q factor is achieved by increasing the number of tapering holes with optimum tapering displacements [4.18]. After forth-tapering holes, the Q values were increased significantly (refer Figure 4.5).

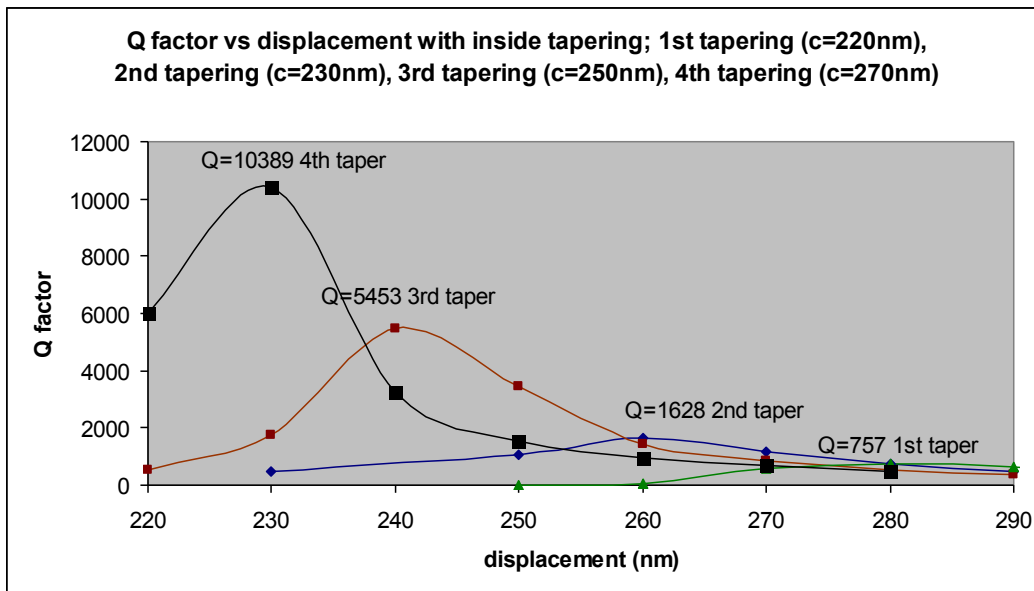


Figure 4.5: 2D FDTD computed results of Q values of 1D PhC nanocavity from single to four aperiodic tapering holes inside with various displacements. The cavity length was adjusted to suit the targeted location at 1310 nm.

In order to realise a higher Qs, extra mirrors in the period section were added. However, the transmission spectrum was reduced when additional Bragg mirrors were introduced. Refer Figure 4.6 (a) and (b). This is due to imperfect modal mismatching within the tapering design. One of the methods to increase the transmission spectrum is by introducing the periodic Bragg mirrors inside the cavity [4.19]. This method however shows a significant reduction in the Q values and the resonant wavelength was split. Nevertheless, this design is more suitable for telecom applications.

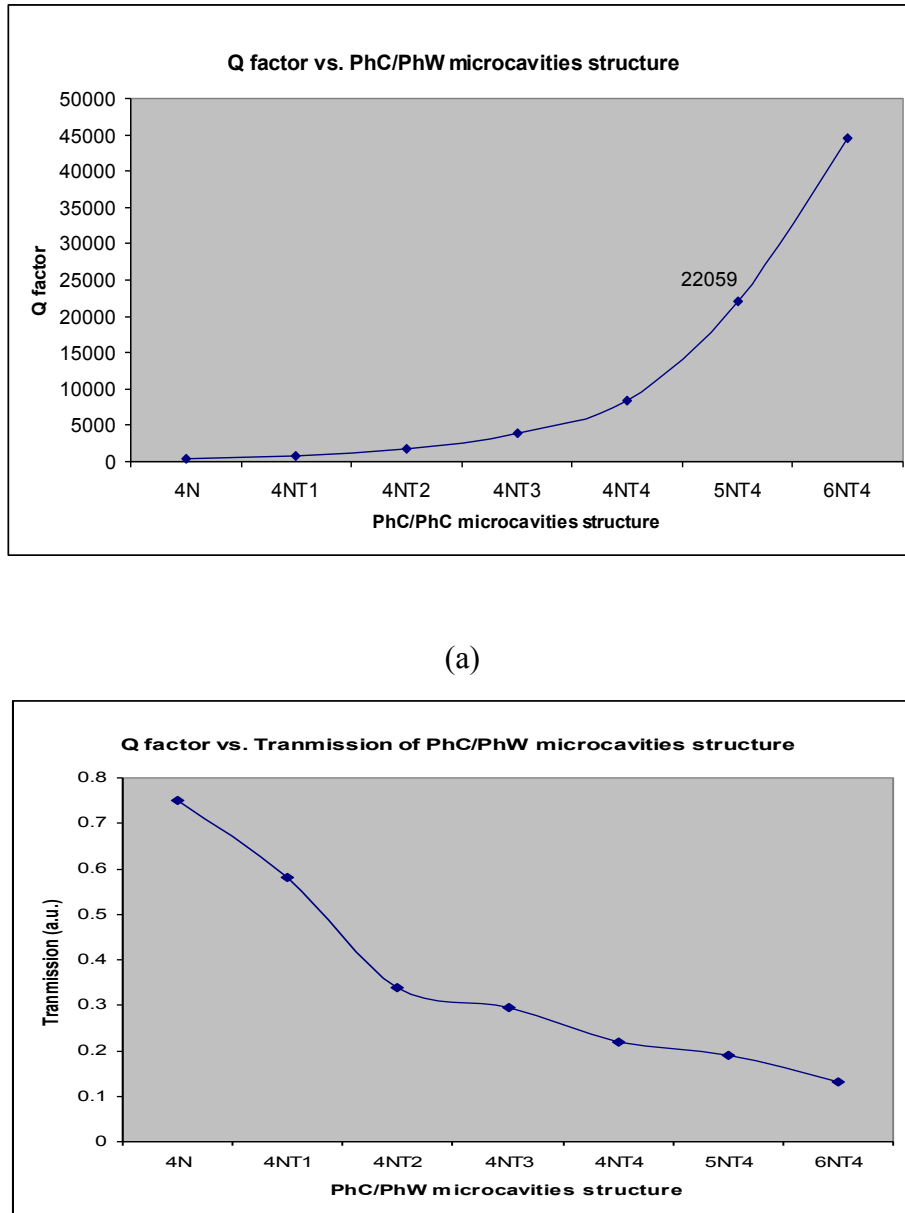


Figure 4.6: Computed 2D FDTD results show (a) significant increase of Q factor values when additional Bragg mirrors were added (5NT4 and 6NT4 are 5 and 6 Bragg mirrors with 4 tapering holes). 4N, 4NT1, 4NT2, 4NT3 and 4NT4 indicate 4 Bragg mirrors, 4 Bragg mirrors with 1,2,3 and 4 aperiodic tapering holes respectively. (b) Graph shows transmission spectrum is drastically decreased when additional mirror holes were introduced.

The designed devices were fabricated and measured using end-fire coupling technique for characterisation. From the measured spectrum transmission of the device, no resonant wavelength was detected near the simulated result, which is at 1290 nm. It is

possible that the resonant wavelength was undetected due to poor transmission. The next resonant wavelength peak was located at  $1479.56\text{ nm}$ . The Q factor of the resonant is close to 500 and the transmission was barely 30 %. It is concluded that the resonance was impractical due to poor Q factors and low transmission. Moreover, the location is towards the end of the equipment detection range.

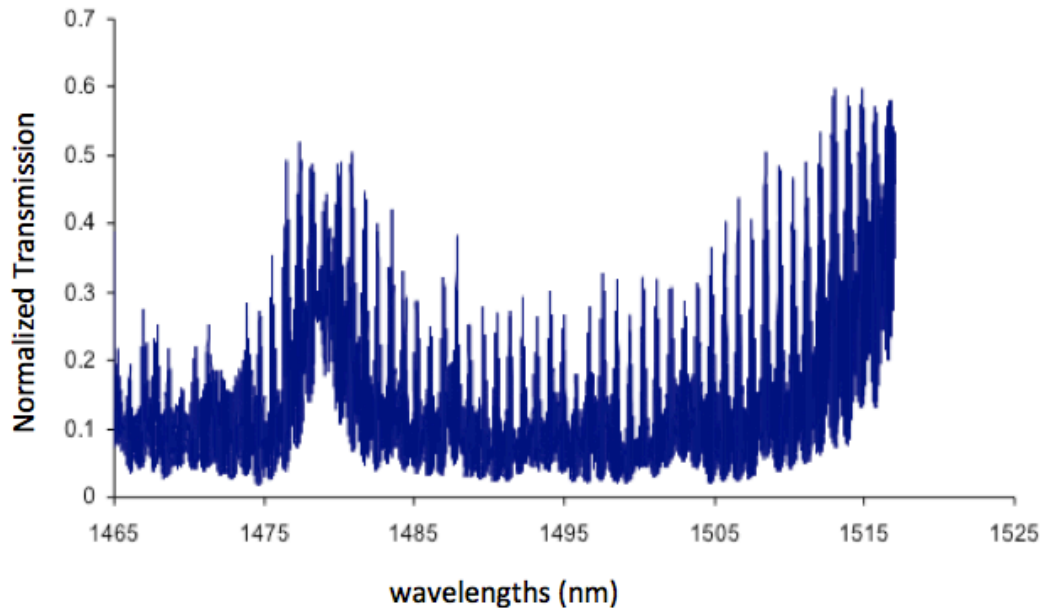


Figure 4.7: The measured transmission spectrum of device working at  $1330\text{ nm}$ . The transmission intensity was normalised to the unpatterned optical waveguide.

#### 4.4 1-D PhC nanocavities working at $1550\text{ nm}$

During the later part of this work, the design of the 1D PhC nanocavity was changed to suit the standard optical fibre wavelength of  $1550\text{ nm}$ . It is known that  $1550\text{ nm}$  range offers lower dispersion and absorption characteristics for the silica cladding on SOI [4.20]. The structures were redesigned using the same method based in the  $1550\text{ nm}$  range. In addition, the Bragg mirrors were tapered from outside and within the cavity. This creates a smooth conversion of the travelling mode from the optical waveguide through the cavity region. However, the tapering mirror holes were limited to three in order to reduce the losses in transmission spectrum. It was observed that the design of 1D PhC nanocavity is based on three elements; namely the Bragg mirrors, the tapering sequence, and the cavity lengths. [4.10]. In the new design shown in Figure 4.8, the

period,  $A$  from centre to centre of the Bragg mirrors was set at  $420\text{ nm}$  and the radius,  $r$  is  $115\text{ nm}$ . The three tapering holes on the inside and outside of the Bragg mirrors are located from centre to centre of holes are  $385$ ,  $355$  and  $355\text{ nm}$  and the radius are  $105$ ,  $95$  and  $85\text{ nm}$  respectively. The function of outside tapers are similar to the inside tapers. They are used to reduce the mode mismatch between the patterned and unpattern waveguide.

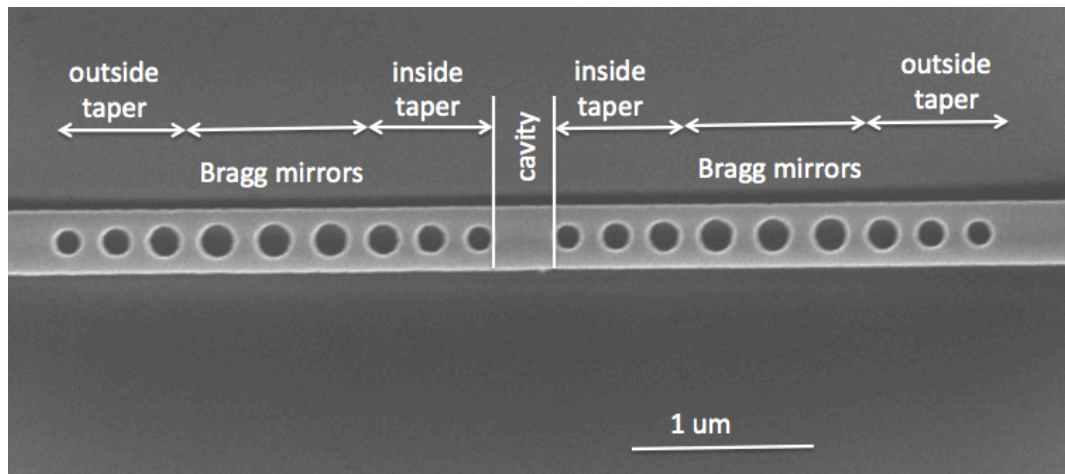


Figure 4.8: SEM micrograph of the fabricated device targeted working at  $1550\text{ nm}$  range.

The devices were fabricated using Vistec VB6, electron beam lithography and dry etch technology. They were characterised using the tunable laser covering the range between  $1457\text{ nm}$  and  $1580\text{ nm}$ . The devices were end-fire coupled from input to output of the optical waveguides with TE polarised light and were detected using germanium photo-detector.

#### 4.4.1 Cavity length arrangement

The high Q factor strongly depends on the optimum length of the cavity. Therefore, on the devices, the cavity lengths,  $c$  were varied between  $390$  and  $550\text{ nm}$ . Refer Figure 4.9 for the device experimental measurements of PhC nanocavity for  $N = 2$ . From the observation, the resonant wavelengths started to appear at  $c = 430$  to  $510\text{ nm}$  lengths. For the  $c = 390$  and  $410\text{ nm}$ , the resonance are not available because the cavity length is smaller than the period,  $A$ . On the longer side, ( $c = 530$  and  $550$ ), the resonance

have reached the stop band and can compromised the end results.

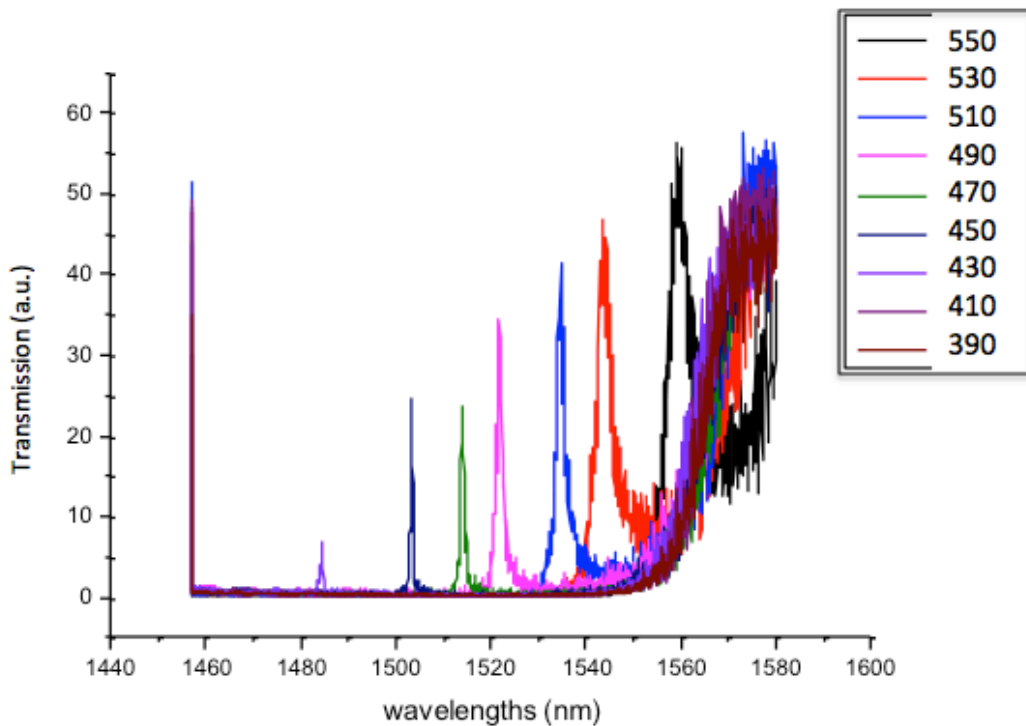


Figure 4.9: Experimentally measured transmission spectra of PhC nanocavity devices for  $N = 2$  with different cavity lengths displacement varying from 390 to 550 nm (legend).

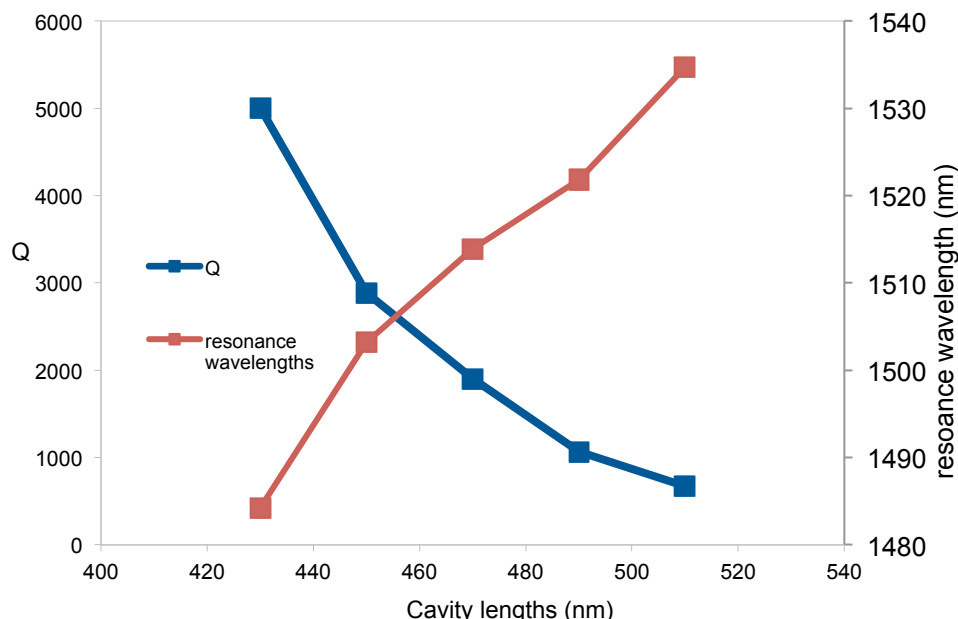


Figure 4.10: Q factors and resonance wavelengths location for various cavity lengths from 430 to 510 nm. The Q factor is estimated by a Lorentzian fitting of the peaks at the resonance wavelengths.

From the experimental results of the device with  $N = 2$  (Refer Figure 4.10), the resonant wavelengths locations varied with their cavity lengths. Longer cavity lengths correspond to longer resonance wavelengths. This is because of the incremental increase of effective index at the cavity region. However, the Q factors are at a maximum value for the shorter cavity lengths corresponding to a smaller mode volume.

## 4.4.2 Mirror strength

Another important property to boost the Q factor on such devices is to increase of the number of periods,  $N$  at specific cavity lengths. This is because when the Bragg mirrors strengthened, the field penetrates lesser into the mirrors [4.21]. An optimum  $Q$  depends on the specific cavity length for a given  $N$  (Refer Figure 4.11). However, when the number of mirrors increase, the transmission become more critical than with devices with less mirror holes. The losses,  $L_m$  are not dependent on  $N$ , but correspond to the mode profile mismatch at the taper section. In the literature,  $Q$  factors saturate as  $N$  increase over 4-5 due to losses located at the tapered section [4.9]. The mirror strength is determined by three parameters, all linked to relation;

$$R_m + T_m + L_m = 1 \quad (\text{Eq. 4.2})$$

Where  $R_m$ ,  $T_m$  and  $L_m$  are modal reflectivity, modal transmittance and modal losses respectively.

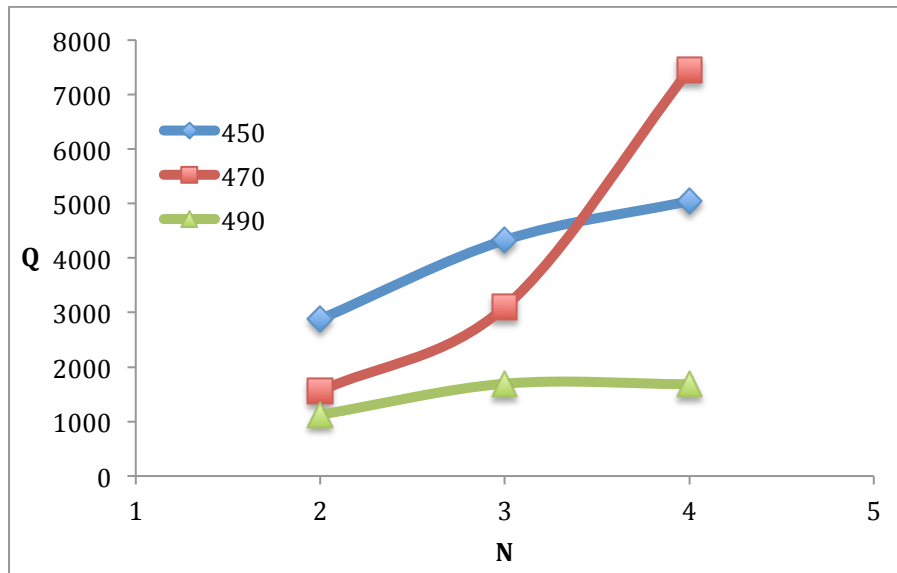


Figure 4.11: The  $Q$  of the measured devices corresponds with the specific cavity lengths (450, 470 and 490 nm) for a given  $N$ .

## 4.5 1-D PhC nanocavities membrane

The cavity region plays significant roles when designing the PhC optical sensor. This is due to the fact that at the cavity, the travelling mode is bounced back and forth within the Bragg mirrors and interacts with the analytes. Therefore, one of the concepts to increase the sensitivity is by increasing the surface interactions [4.22]. This can be realized by removing the silica buffer layer cladding underneath the silicon-guiding layer. Hence, the field interacts with the analyte between the top and the bottom of the cavity. Moreover, it is noted that a suspended PhC nanocavity, or PhC nanocavity membrane can increase the  $Q$  factor [4.23].

The PhC nanocavity membrane devices were fabricated using similar methods described earlier with additional wet etching technology to remove the silica buffer layer underneath. The experimental measurement results were compared to the one with the silica cladding underneath (see Figure 4.12 (a) and (b)). For the comparison purposes, both devices were measured with specification of cavity length,  $c = 450, 470$  and  $490\text{ nm}$  and periodic mirrors,  $N = 3$ . From the observation, the resonant wavelengths peaks of the PhC nanocavity membrane were shifted towards the shorter wavelengths by approximately  $15\text{ nm}$ . The shifts are particularly due to the reduction in the effective

index of the devices.

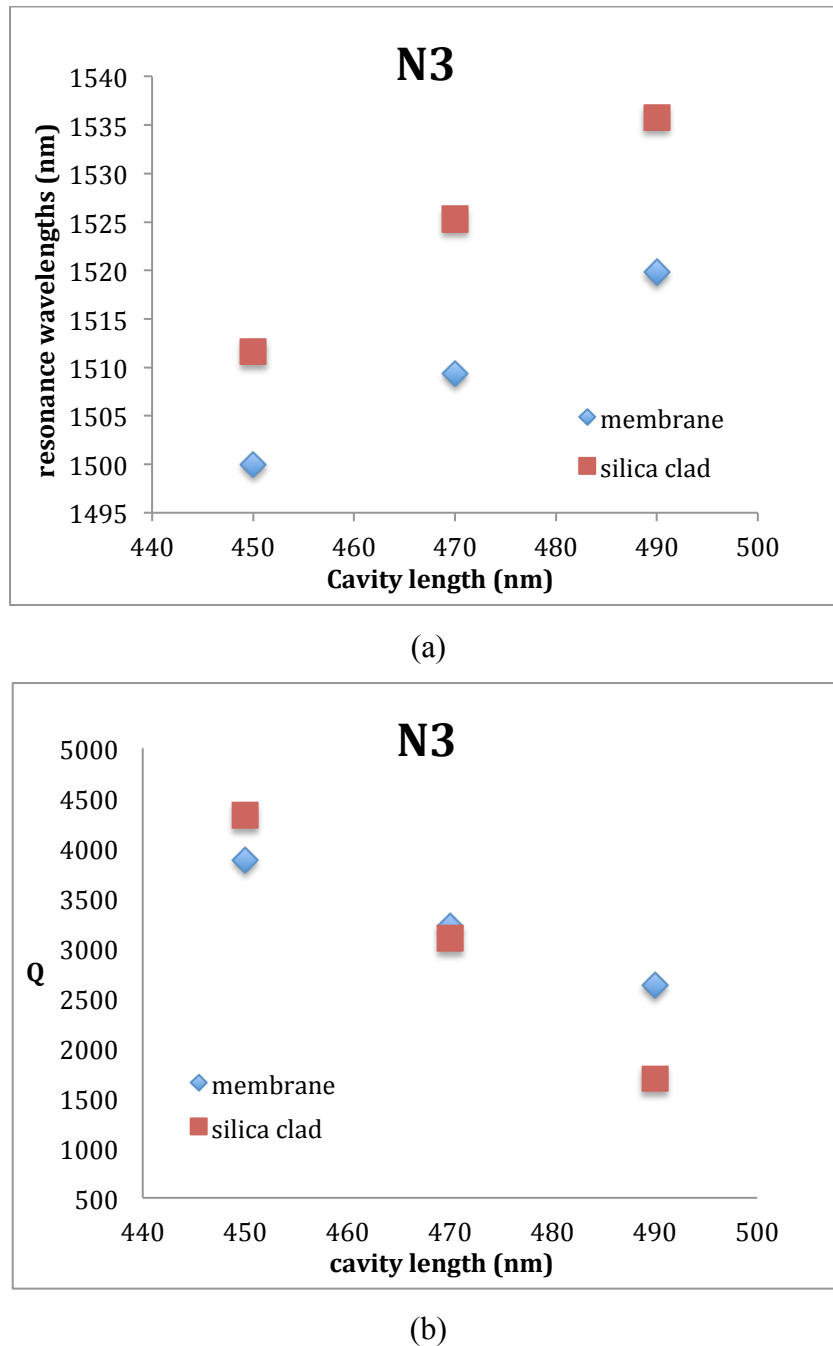


Figure 4.12: Experimental results showing comparison of the PhC membrane with the non-suspended (Silica clad) PhC nanocavity. (a) Shifts of the resonant wavelengths peaks towards the shorter wavelengths when silica was removed and (b) Q factor comparison between the two devices.

Meanwhile, the  $Q$  factor value of the device with silica cladding are slight higher

for  $c = 450 \text{ nm}$ . However, on the longer cavity length ( $c = 470$  and  $490 \text{ nm}$ ), the  $Q$  factor values are increase by 120 and 900 respectively. In other words, the  $Q$  factor value of PhC membrane started to show improvements for  $c = 470$  and  $490 \text{ nm}$  compared to PhC with silica buffer cladding.

Many attempts have been made to produce the high  $Q$  of PhC cavities with air cladding structures [4.24 - 4.25], but there are several arising issues for such devices. These include its mechanical stability, fabrication complexity and thermal dilation. In conclusion, even if the air membrane devices produce higher  $Q$  factor values compared to the silica cladding at a certain cavity length, the risk of having the membrane collapse or broken is not worthwhile for optical sensing purposes.

## 4.6 Conclusions

In this chapter, the work has reviewed the promising earlier results on PhC nanocavities devices with the silicon thickness of  $260 \text{ nm}$ . Initially, the devices were designed to work at  $1310 \text{ nm}$  wavelength range. However, the devices were redesigned to work in the  $1550 \text{ nm}$  wavelength range. This mainly because the  $1550 \text{ nm}$  wavelengths range offers lower dispersion and absorption characteristics for silicon. There are three main elements to consider when designing the efficient PhC nanocavities, which are the modal adaptation (tapering holes technique), the number of periods,  $N$  and the cavity length,  $c$ . In order to increase the surface interaction for higher sensitivity, PhC nanocavity membranes approach have been explored. However, although the devices provide the slight increment of the  $Q$  factor values, this is offset with issues of mechanical stability and fabrication complexity.

## References

- [4.1] Yablonovitch, Eli. "Inhibited spontaneous emission in solid-state physics and electronics." *Physical Review Letters* 58, no. 20 (1987): 2059.
- [4.2] John, Sajeev. "Strong localization of photons in certain disordered dielectric superlattices." *Physical Review Letters* 58, no. 23 (1987): 2486.
- [4.3] Tandaechanurat, A., S. Ishida, K. Aoki, D. Guimard, M. Nomura, S. Iwamoto, and Y. Arakawa. "Demonstration of high-Q ( $> 8600$ ) three-dimensional photonic crystal nanocavity embedding quantum dots." *Applied Physics Letters* 94, no. 17 (2009).
- [4.4] Akahane, Yoshihiro, Takashi Asano, Bong-Shik Song, and Susumu Noda. "High-Q photonic nanocavity in a two-dimensional photonic crystal." *Nature* 425, no. 6961 (2003): 944-947.
- [4.5] Soljačić, Marin, and John D. Joannopoulos. "Enhancement of nonlinear effects using photonic crystals." *Nature materials* 3, no. 4 (2004): 211-219.
- [4.6] Bog, Uwe, Cameron LC Smith, Michael W. Lee, Snjezana Tomljenovic-Hanic, Christian Grillet, Christelle Monat, Liam O'Faolain et al. "High-Q microfluidic cavities in silicon-based two-dimensional photonic crystal structures." *Optics Letters* 33, no. 19 (2008): 2206-2208.
- [4.7] Bog, Uwe, Cameron LC Smith, Michael W. Lee, Snjezana Tomljenovic-Hanic, Christian Grillet, Christelle Monat, Liam O'Faolain et al. "High-Q microfluidic cavities in silicon-based two-dimensional photonic crystal structures." *Optics Letters* 33, no. 19 (2008): 2206-2208.
- [4.8] Foresi, J. S., Pierre R. Villeneuve, J. Ferrera, E. R. Thoen, G. Steinmeyer, S. Fan, J. D. Joannopoulos, L. C. Kimerling, Henry I. Smith, and E. P. Ippen. "Photonic-bandgap microcavities in optical waveguides." *Nature* 390, no. 6656 (1997): 143-145.

- [4.9] Velha, P., Picard, E., Charvolin, T., Hadji, E., Rodier, J.C., Lalanne, P. and Peyrade, D.. Ultra-high Q/V Fabry-Perot microcavity on SOI substrate. *Optics express*, 15(24), pp.16090-16096 (2007).
- [4.10] Zain, Ahmad Rifqi Md, Nigel P. Johnson, Marc Sorel, and M. Richard. "Ultra high quality factor one dimensional photonic crystal/photonic wire microcavities in silicon-on-insulator (SOI)." *Optics express* 16, no. 16 (2008): 12084-12089.
- [4.10] Notomi, Masaya, E. Kuramochi, and H. Taniyama. "Ultrahigh-Q nanocavity with 1D photonic gap." *Optics Express* 16, no. 15 (2008): 11095-11102.
- [4.11] Schönenberger, Sophie, Marcus S. Dahlem, Thilo Stöferle, Nikolaj Moll, Rainer F. Mahrt, Bert J. Offrein, Erich P. Ippen et al. "Silicon photonic microcavities for optical switching." In *Lasers and Electro-Optics 2009 and the European Quantum Electronics Conference. CLEO Europe-EQEC 2009. European Conference on*, pp. 1-1. IEEE, (2009).
- [4.12] Haret, Laurent-Daniel, Takasumi Tanabe, Eiichi Kuramochi, and Masaya Notomi. "Extremely low power optical bistability in silicon demonstrated using 1D photonic crystal nanocavity." *Optics Express* 17, no. 23 (2009): 21108-21117.
- [4.13] Gnan, M., S. Thoms, D. S. Macintyre, Richard M. De La Rue, and M. Sorel. "Fabrication of low-loss photonic wires in silicon-on-insulator using hydrogen silsesquioxane electron-beam resist." *Electronics Letters* 44, no. 2 (2008): 115-116.
- [4.14] Eichenfield, Matt, Ryan Camacho, Jasper Chan, Kerry J. Vahala, and Oskar Painter. "A picogram-and nanometre-scale photonic-crystal optomechanical cavity." *Nature* 459, no. 7246 (2009): 550-555.
- [4.15] Joannopoulos, John D., Steven G. Johnson, Joshua N. Winn, and Robert D.

- Meade. *Photonic crystals: molding the flow of light*. Princeton university press, (2011).
- [4.16] Villeneuve, Pierre R., Shanhui Fan, J. D. Joannopoulos, Kuo-Yi Lim, G. S. Petrich, L. A. Kolodziejski, and Rafael Reif. "Air-bridge microcavities." *Applied Physics Letters* 67, no. 2 (1995): 167-169.
- [4.17] Lalanne, Ph, and Jean Paul Hugonin. "Bloch-wave engineering for high-Q, small-V microcavities." *Quantum Electronics, IEEE Journal of* 39, no. 11 (2003): 1430-1438.
- [4.18] Zain, Ahmad Rifqi Md, Marco Gnan, Harold MH Chong, Marc Sorel, and Richard M. De La Rue. "Tapered photonic crystal microcavities embedded in photonic wire waveguides with large resonance quality-factor and high transmission." *Photonics Technology Letters, IEEE* 20, no. 1 (2008): 6-8.
- [4.19] Zain, Ahmad Rifqi Md, Nigel P. Johnson, and M. Richard. "High-transmission 1D photonic crystal/photonic wire multiple cavity structures based on silicon-on-insulator." In *Photonics Europe*, pp. 69891A-69891A. International Society for Optics and Photonics, (2008).
- [4.20] Friedman, Edward, and John Lester Miller. "Photonics rules of thumb: optics, electro-optics, fiber optics, and lasers." *Photonics rules of thumb: optics, electro-optics, fiber optics, and lasers, 2nd ed., by E. Friedman and JL Miller. SPIE press monograph, PM 132. SPIE Press/McGraw-Hill professional engineering*. New York, NY: McGraw-Hill, 2004 (2004).
- [4.21] Velha, Philippe, Jean-Claude Rodier, Philippe Lalanne, Jean-Paul Hugonin, D. Peyrade, E. Picard, T. Charvolin, and E. Hadji. "Ultra-high-reflectivity photonic-bandgap mirrors in a ridge SOI waveguide." *New Journal of Physics* 8, no. 9 (2006): 204.
- [4.22] Smith, Cameron L., Uwe Bog, Snjezana Tomljenovic-Hanic, Michael W. Lee, Darran K. Wu, Liam O'Faolain, Christelle Monat et al. "Reconfigurable

microfluidic photonic crystal slab cavities." *Optics Express* 16, no. 20 (2008): 15887-15896.

- [4.23] Zain, Ahmad Rifqi Md, Nigel P. Johnson, Marc Sorel, and Richard M. De La Rue. "High quality-factor 1-D-suspended photonic crystal/photonic wire silicon waveguide micro-cavities." *Photonics Technology Letters, IEEE* 21, no. 24 (2009): 1789-1791.
- [4.24] O'Faolain, Liam, Xiaodong Yuan, Douglas McIntyre, Stephen Thoms, Harold Chong, R. M. De La Rue, and Thomas F. Krauss. "Low-loss propagation in photonic crystal waveguides." *Electronics Letters* 42, no. 25 (2006): 1.
- [4.25] Noda, Susumu, Masayuki Fujita, and Takashi Asano. "Spontaneous-emission control by photonic crystals and nanocavities." *Nature Photonics* 1, no. 8 (2007): 449-458.

# Chapter 5: Microfluidic Channel System

- 5.1 Introduction
- 5.2 Optical sensing system
- 5.3 PDMS Microfluidic Channel System
  - 5.3.1 Introduction
  - 5.3.2 Fabrication of Microfluidic Channel
    - 5.3.2.1 PDMS Master Mould*
    - 5.3.2.2 PDMS Microfluidic Channel Chip*
- 5.4 Characterizations and System Setup
- 5.5 Conclusion
- References

## 5.1 Introduction

In the previous chapters, the design, fabrication, and some experimental results of the 1D PhC nanocavity devices were reviewed and analysed. In order to make the structures a complete optical sensing device, the design and fabrication of PDMS microfluidic channel system are presented in this chapter. The system setup and characterization of the complete optical sensing system were also discussed.

## 5.2 Optical sensing system

There are many varieties of sensing system using optical, electrical and mechanical approach. Nevertheless, optical sensors are proven able to provide very high sensitivity, capable of measuring a wide dynamic range of wavelengths or frequencies, and have immunity to electrical interference [5.1]. One of the most common optical sensors that available commercially is fibre optic sensors (FOS). FOS is desirable due to their ability for remote sensing, they do not need electrical power and are able to be multiplexed to many sensors. Although FOS is considered small in size, their ability to do sensing at the submicron level is still uncertain.

Photonic devices such as 1D PhC nanocavities are one of the interesting structures to be used as optical sensors. This is due to their submicron features and ability to detect the change of refractive index of the surrounding medium. Moreover, they have the potential to be integrated to a CMOS environment when using the silicon-based material. In this work, the optical sensor a 1D PhC nanocavity device is equipped with a Polydimethylsiloxane (PDMS)-based microfluidic channel system as the analyte transportation media.

## 5.3 PDMS Microfluidic Channel System

### 5.3.1 Introduction

Microfluidics channels provide a powerful platform for biological and chemical sensing. In a microfluidic channel, small volumes sample, solvents and reagents or analytes are moved through micron scaled channel/s embedded in a chip. There are many methods to propagate analytes through the device. The use of capillary forces, which is a passive fluid control technique, the channel transports the analytes to desired location. Although there are other methods to channel the analytes such as using control pumps [5.2] or micropumps [5.3], the cost to fabricate the system using these methods is high and controlling the systems can be complicated. In this project, a passive straight channel-in approach was used for microfluidic channel system. The microfluidic channel chip is made from PDMS (Sylgard 184: two component base polymer and curing agent) commercially available from Dow Corning [5.4].

Miniaturized versions of PDMS microfluidic channels offer many advantages, including small volumes of analytes and easy fabrication. For valuable samples and high-throughput screening, a small volume of analytes is crucial. Fabricated PDMS channels are capable of flowing analytes in a sub 60 *nm* cross-section channel [5.5]. In addition, the PDMS microfluidic channels are portable, low cost, versatile in design and most importantly are biocompatible. Once the master mould is made, it is generally fast and reliable to reproduce the microfluidic channels. Nonetheless, the small dimension of microfluidic channel system has the potential for integration with other miniaturized devices [5.6 – 5.7]. Furthermore, the PDMS microfluidic system is optically transparent down to 300 *nm* in wavelengths; hence it can be applied in the telecommunication wavelength range [5.8]. Finally, further integration with other photonic devices and using CMOS technology is possible [5.9]. The work aim to deliver the smallest possible liquid volume interaction with the sensing area.

### 5.3.2 Fabrication of Microfluidic Channel

In this section, the fabrication of the microfluidic channel is divided into two subsections. First described is the fabrication of the master mould and latter it discussed is the casting of the PDMS chip and bonding it with the silicon PhC waveguides chip.

#### 5.3.2.1 PDMS Master Mould

##### *Inverse Mask for Microfluidic Channel*

The procedures for the fabrication of PDMS structures for microfluidics have been described in detail elsewhere [5.10 – 5.12]. Initially, the mask of straight channels arrays for duplication channels pattern was fabricated. The mask can be used for master mould replication later. The specification of the channel was set to accommodate the 1D PhC nanocavity devices chip cleaved earlier. The microfluidic channel specification consists of two circular of 1 mm diameter wells connected end to end connected with a straight channel of 500  $\mu\text{m}$  width and 10 mm length (Refer Figure 5.1).

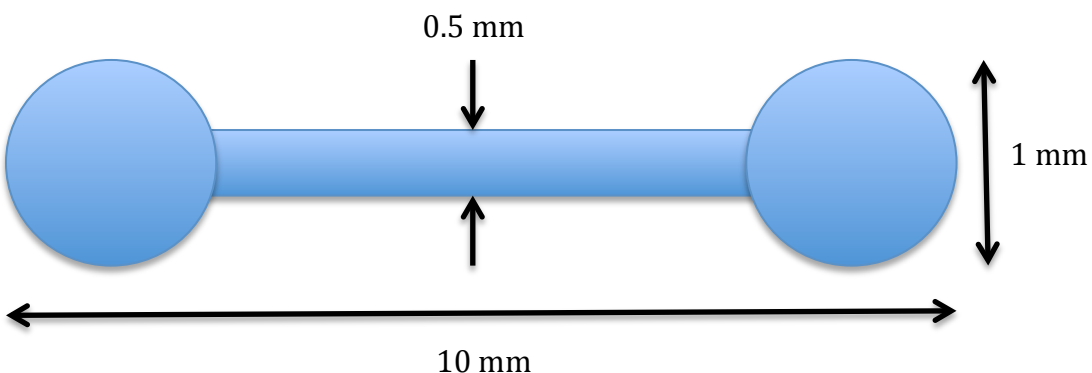


Figure 5.1: Specification of PDMS microfluidic channel

##### *Resist for mould and lithography*

To make the master mould, a cleaved and cleaned silicon wafer chip was prepared (using same procedures described in Section 3.4 in Chapter 3). For the further removal of contamination and good resist adhesion, the silicon wafer chip was placed into an O<sub>2</sub> Plasma Asher for two minutes at 60 W.

Dow Corning SU-8 3050 (SU-8), a negative tone photoresist has been chosen as the mould due to its ability to attain vertical and smooth planar sidewall characteristics and is resilient after it has been hard-baked. A thickness of  $50 \mu\text{m}$  SU-8 resist was spun at 2000 *rpm* for 30 *seconds* onto the silicon wafer chip. The backside of the silicon wafer chip was cleaned to remove resist residues, which is essential to ensure that the chip is lying flat during photolithography exposure. The silicon wafer chip was placed onto a 95 °C hotplate for 45 *minutes*. The chip was then left to attain room temperature and was inspected for the presence of any bubbles or wrinkles. If present, the chip was placed onto the 95 °C hotplate again. The repeated heating up and cooling down procedures helps to remove bubbles and wrinkles in the resist [5.11].

Next, SU-8 resist is exposed to masked UV light using the MA 6 lithography tool to pattern PDMS inverse mould. A post exposure bake procedure was carried out before resist development. The silicon wafer chip was placed onto a 95 °C hotplate for five minutes. The SU-8 resist pattern was developed with EC Microposit solvent for 15 minutes. Subsequently, the wafer was cleaned with a fresh EC Microposit solvent and an IPA for 10 *seconds* each in separate beakers. Later, the chip was placed into 180 °C oven for at least three hours to harden and make it resilient for mould replication. The inverse microfluidic channel made from SU-8 was characterised using a Veeco Dektak, profilometer tool to check the final thickness and was inspected under an optical microscope.

#### *Salinization process*

Finally, 2-3 drops of salinizing agent, Perfluorooctyltriethoxysilane 98 % (Sigma Aldrich) was added onto the master mould. The master mould was placed in separate petri dishes and was put into a vacuum desiccator for two hours. This procedure will change the surface of the master mould to be hydrophilic, and further facilitate the releasing of PDMS chip from the master mould [5.13].

### 5.3.2.2 PDMS Microfluidic Channel Chip

#### *Casting and Releasing the PDMS chip*

PDMS base polymer and the curing agent was mixed in a 10:1 ratio in a plastic cup. The mixture was mixed well until it is milky due to the formation of air bubbles. The mixture was degased in a vacuum desiccator until all bubbles disappeared. This process took about 20 to 30 *minutes* to complete. Next, the vacuum desiccator was vented to pop large bubbles that still appear at the surface. The PDMS mixture was poured onto SU-8 master mould wafer chip that has been fabricated (Refer to section 4.2.2.1). The PDMS was cured for at least two of hours in a 75 °C temperature oven. Subsequently, when the PDMS was hardened, it was cut to 8 mm x 15 mm (width x length) and was peeled off from the master mould chip using a scalpel. Finally, two small holes are drilled into the PDMS chip using a BD Microlance to produce inlets and outlets.

#### *Bonding PDMS chip with Silicon PhC waveguides chip*

The PDMS can bond to itself and to silicon-based substrate with the aid of an O<sub>2</sub> Plasma Asher. The surface treatment for bonding using the O<sub>2</sub> Plasma Asher are carried out with silicon PhC waveguides chip and the PDMS chip (top side down) at a low power of 20 W for 20 *seconds*. In order to increase the interval time before the PDMS chip and silicon PhC waveguides chip permanently bond, a few drops of lubricant such as methanol was used. This procedure was performed to allow more time to allow precise alignment of the sensing area and the channel. The wafer was left for 30 *minutes* to ensure the methanol was evaporated completely.

The replicated PDMS chips that have been fabricated and inspected have good uniformity with the initial batches, and show no signs of degradation. The master mold is considered suitable for further applications.

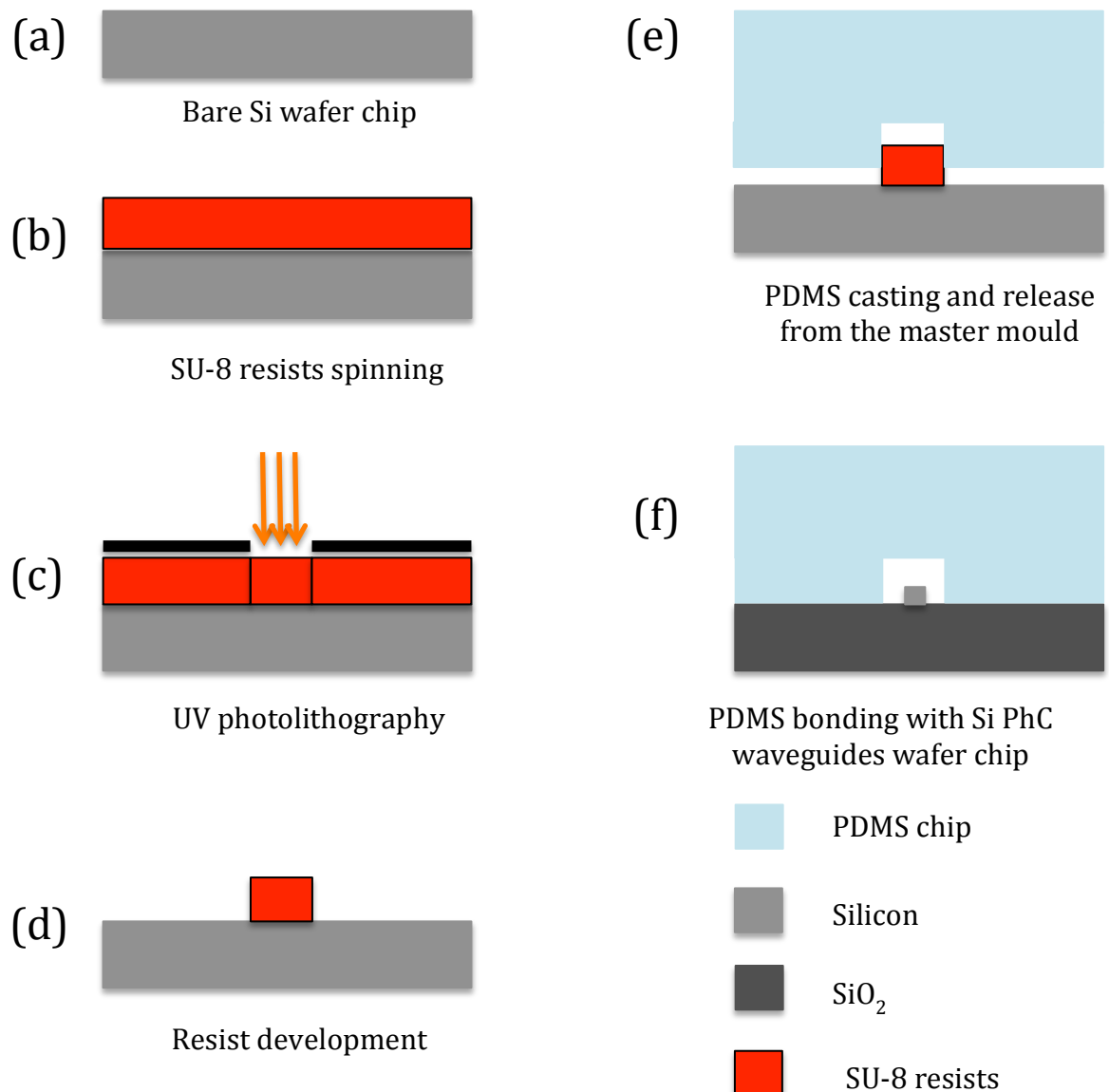


Figure 5.2: Figure illustrating the simplified steps in the fabrication of the PDMS microfluidic channel system, (a)–(d) UV photolithography in SU-8, (e)–(f) PDMS casting and bonding.

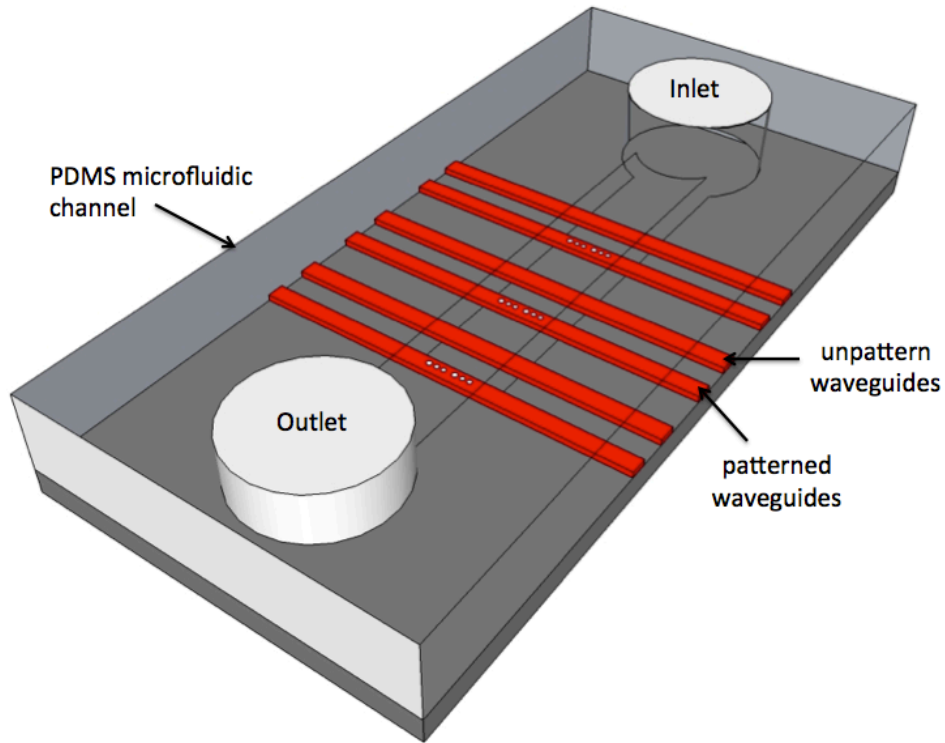


Figure 5.3: Illustration of PDMS microfluidic channel attached to the PhC nanocavity devices chip. The diagram is not to scale.

## 5.4 Characterisation and System Setup

In order to determine the spectroscopic response, the PhC nanocavity devices need to be characterised before they can be used in sensing application. In the previous chapter, the PhC nanocavity devices have been analysed and measured. In this section, the characterisation technique and the system set up are reviewed. It consists of the characterisation set up for PhC nanocavity devices and with the PDMS channel intact.

The most straightforward way to assess the fabricated devices is by using the end-fire type apparatus. It has the capability to test and measure the transmission spectra of the patterned and unpattern waveguide structures in the plane of the sample. Hence, all of the devices considered in this project were measured using this method. In general, the devices, the fibre tip and magnification lenses were placed on a 3-axis translation stage, which was mounted directly on the optical table and manipulated precisely using

micrometer screws. The PhC nanocavity devices were measured using a tuneable laser shown in Figure 5.4 that source covering the wavelength range from 1460 to 1580 nm, 1520 to 1620 nm and 1263 to 1330 nm. The first two covers devices based on 1550 nm wavelengths and 1310 nm for the latter. The devices were end-fired coupled to the optical waveguides with TE polarised light using a fibre tip and 40 X magnification objective lenses for the input and output respectively. The transmitted optical signal was modulated by a chopper at the frequency of 317 Hz and was detected using a germanium photodiode (photo-detector). Two polarizers were used in the set up. The first one, a rotatory polarizer was connected between the fibre tip and the lock-in amplifier and the next one is between the magnification lenses and the optical chopper. The rotatory polarizer is used to select the desired injected polarization, in this case a TE polarized light. An in-house developed system using a LabView program from National Instruments [5.14] was used to synchronise the laser source and the lock-in amplifier. The whole system was control via GPIB ports on a PC. During each measurement, a camera was used to optimise the alignment of the devices in plane with the transmitted output signal.

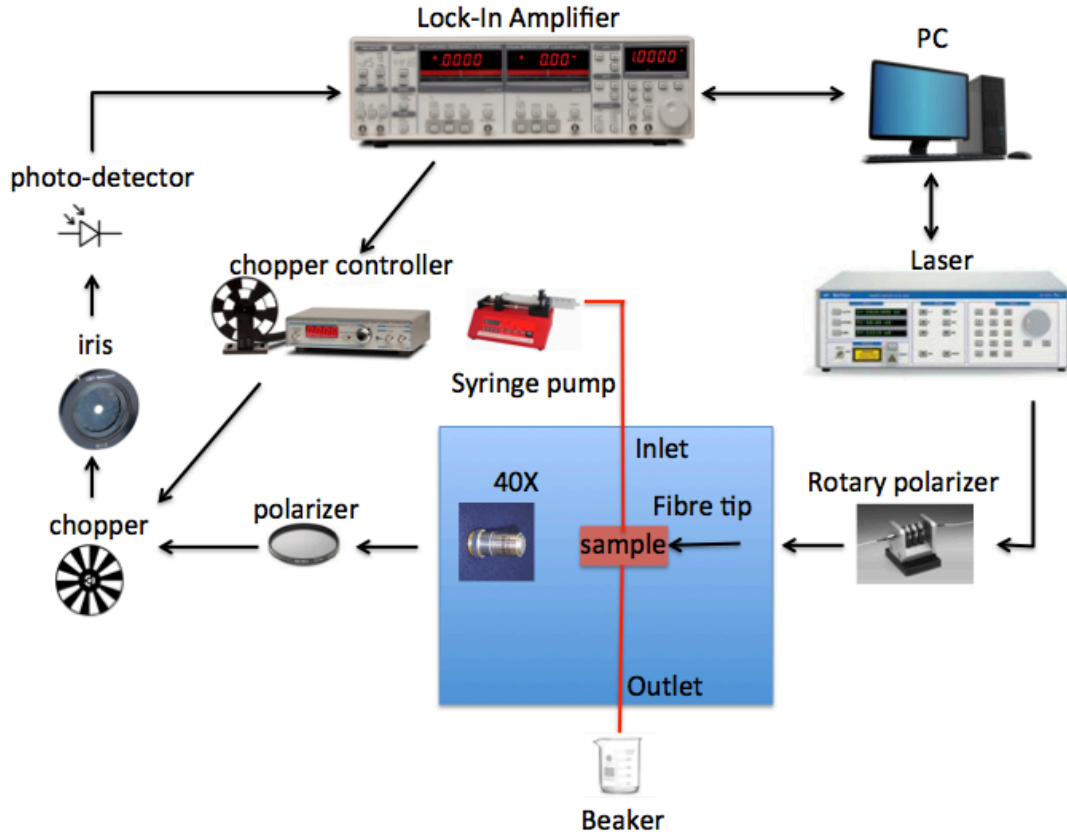


Figure 5.4: Experimental setup used for characterisation of the fabricated devices. The blue square relates to the 40 X magnification lenses, sample and fibre tip in plane on the micro-positioner.

The wavelength range generally used was between 1460 and 1580 nm for most of the experimental measurements. In the other case, the wavelengths range from 1510 to 1640 nm was used using a fast oscilloscope. The tuneable laser is set to a wavelength range between 1510 and 1640 nm. The fast oscilloscope where connected with lock in amplifier and PC to extract the measurement results. This set up is capable of performing the continuous wavelengths sweeps over the entire range. However, some instability in the source power level was present when the tuneable laser approaching to the tuning boundaries. Typically, the input power used during the experimental measurements was set at 1 mW. The input power was set small to avoid any nonlinear effects of silicon such as two-photon absorption and free carrier effects [5.15] from occurring. The experimental measurements performed with a resolution limit by the tuneable laser of 1 pm. This is crucial for the optical sensors in order to detect a submicron change in response of the

system.

The PhC nanocavity waveguides patterns were designed with various cavity lengths. Figure 5.5 shows one of the optical responses of an unpattern waveguide and the patterned waveguides. In some cases, the unpattern waveguides were used as references to analyse the throughput transmission of the PhC nanocavity waveguides. The PhC nanocavity waveguide measured in Figure 5.5 has the cavity length,  $c = 470$  nm, periodic mirror holes,  $N = 2$  and in air environment. The resonance wavelengths, FWHM and Q-factor calculated are 1514. nm, 0.757 nm and  $\sim 2000$  respectively. The waveguide is suitable for sensing due to its high FSR features and the resonance wavelengths is still able to shift (around 30 nm) to the targeted region (at 1550 nm range) when in contact with analyte (DI water as reference) environment.

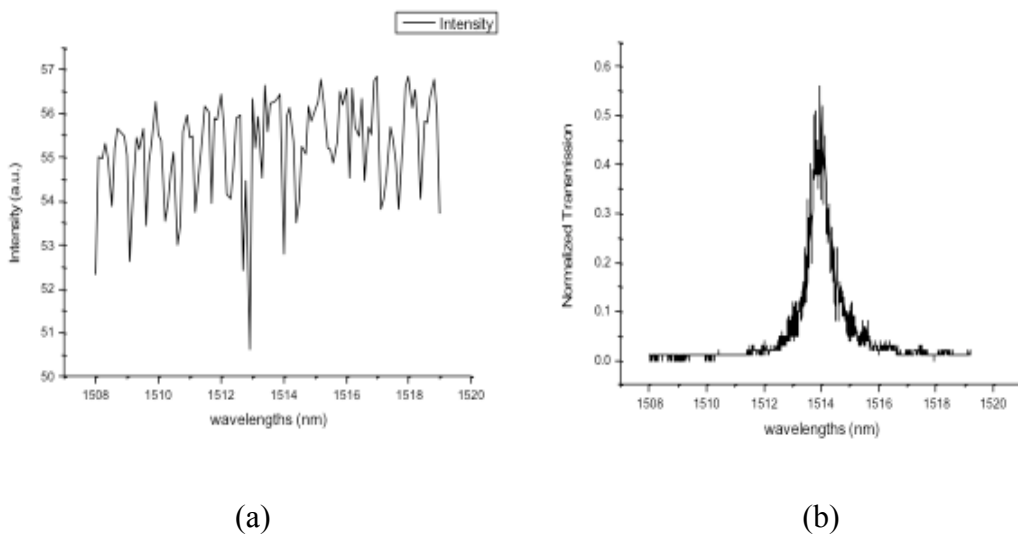


Figure 5.5 Optical response of transmission spectra (a) unpattern waveguides and (b) resonance wavelengths of PhC nanocavity device with the specification of  $N = 2$  and  $c = 470$  nm.

### 5.4.1 System Setup for Optical Sensing

In general, the PhC nanocavity devices were attached with the PDMS microfluidic

system with the inlet and outlet channels connected respectively to the syringe pump and the glass beaker for collection. A 5 or 10 *ml* sterile syringe and a micro pump APL1000 (World Precision Instrument Inc.) were used to transport the analytes into the microfluidic channel. A polytetrafluoroethylene (PTFE) tube of 1 *mm* inside diameter was used as the tubing in the inlet and outlet channel. The schematic arrangements of the system used in the sensing experiments are shown in Figure 5.6 and 5.7.

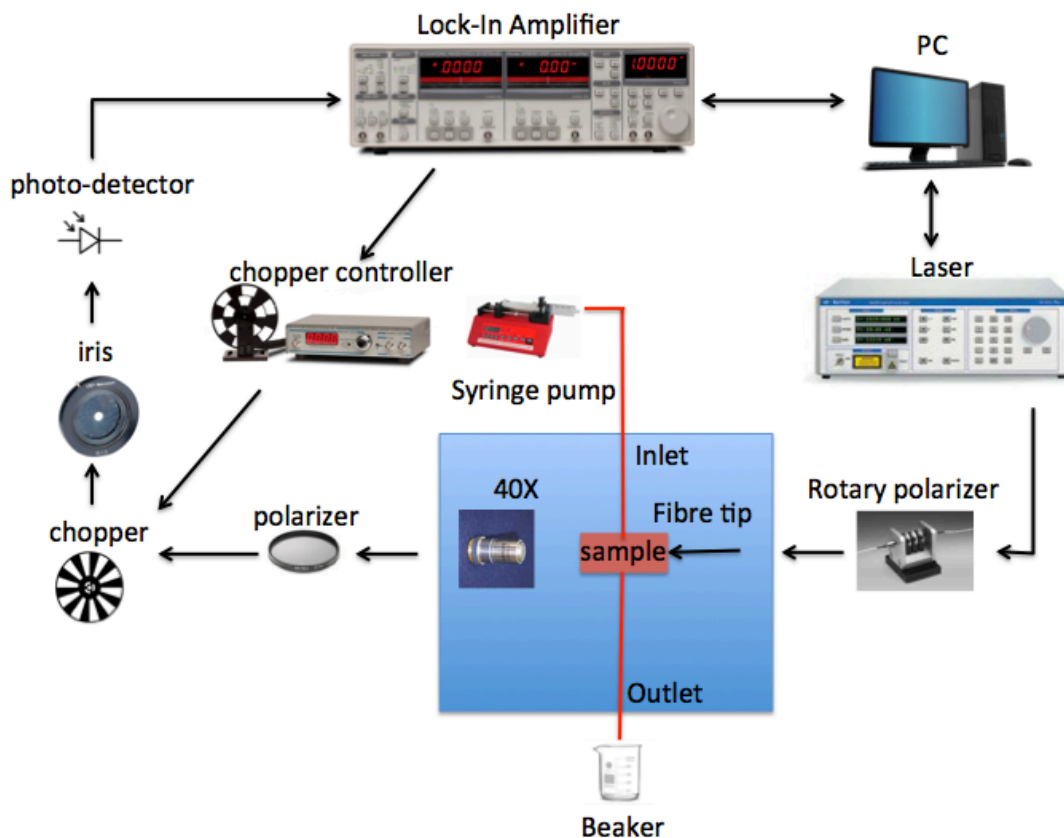


Figure 5.6: Schematic diagram of the partial experimental setup for the sensing applications incorporate with the microfluidic system.

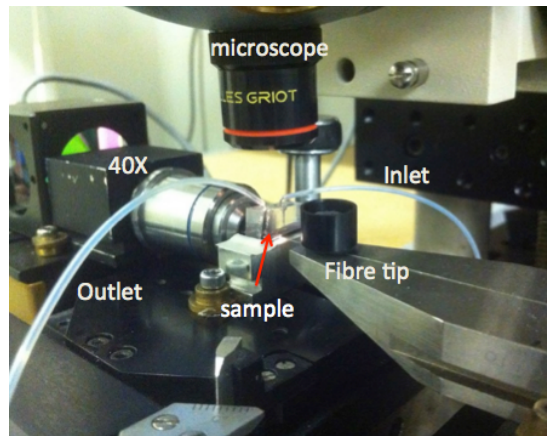


Figure 5.7: Image of the actual experimental setup arrangement on the micro-positioner stage.

## 5.5 Conclusions

In this chapter, the design and the fabrication methods of the PDMS based microfluidic channel were presented. The design is based on the straight passage of input and output channel through the PhC nanocavity devices. The PDMS microfluidic chip can be easily fabricated using the duplication of the master mould. In the second part of the chapter, the characterisation and system setup of the PhC nanocavity devices for the sensing application purposes were reviewed. The characterisation of the devices is important to understand the optical frequency responses of the transmission spectra during the experiments.

## References

- [5.1] Grattan, Kenneth TV, and B. T. Meggitt, eds. *Optical fiber sensor technology*. Vol. 1. London: Chapman & Hall, (1995).
- [5.2] Solovev, Alexander A., Samuel Sanchez, Yongfeng Mei, and Oliver G. Schmidt. "Tunable catalytic tubular micro-pumps operating at low concentrations of hydrogen peroxide." *Physical Chemistry Chemical Physics* 13, no. 21 (2011): 10131-10135.
- [5.3] Abhari, Farideh, Haslina Jaafar, and Nurul Amziah Md Yunus. "A comprehensive study of micropumps technologies." *Int. J. Electrochem. Sci* 7 (2012): 9765-9780.
- [5.4] Sylgard 184 from Dow Corning (online) <http://www.dowcorning.com/>
- [5.5] Quake, Stephen R., and Axel Scherer. "From micro-to nanofabrication with soft materials." *Science* 290, no. 5496 (2000): 1536-1540.
- [5.6] Nandi, Pradyot, David E. Scott, Dhara Desai, and Susan M. Lunte. "Development and optimization of an integrated PDMS based-microdialysis microchip electrophoresis device with on-chip derivatization for continuous monitoring of primary amines." *Electrophoresis* 34, no. 6 (2013): 895-902.
- [5.7] Huang, Kuo-Wei, Yi-Chien Wu, Ji-Ann Lee, and Pei-Yu Chiou. "Microfluidic integrated optoelectronic tweezers for single-cell preparation and analysis." *Lab on a Chip* 13, no. 18 (2013): 3721-3727.
- [5.8] Cai, D. K., A. Neyer, R. Kuckuk, and H. M. Heise. "Optical absorption in transparent PDMS materials applied for multimode waveguides fabrication." *Optical materials* 30, no. 7 (2008): 1157-1161.
- [5.9] Fleger, Markus, and Andreas Neyer. "PDMS microfluidic chip with integrated

- waveguides for optical detection." *Microelectronic engineering* 83, no. 4 (2006): 1291-1293.
- [5.10] Anderson, Janelle R., Daniel T. Chiu, Hongkai Wu, O. J. Schueller, and George M. Whitesides. "Fabrication of microfluidic systems in poly (dimethylsiloxane)." *Electrophoresis* 21, no. 1 (2000): 27-40.
- [5.11] Duffy, David C., J. Cooper McDonald, Olivier JA Schueller, and George M. Whitesides. "Rapid prototyping of microfluidic systems in poly (dimethylsiloxane)." *Analytical chemistry* 70, no. 23 (1998): 4974-4984.
- [5.12] Stroock, Abraham D., and George M. Whitesides. "Components for integrated poly (dimethylsiloxane) microfluidic systems." *Electrophoresis* 23, no. 20 (2002): 3461-3473.
- [5.13] Oh, Bo-Ram, Nien-Tsu Huang, Weiqiang Chen, Jungwhan Seo, Jianping Fu, and Katsuo Kurabayashi. "Localized surface plasmon resonance (LSPR) optofluidic biosensor for label-free cellular immunophenotyping." In *17th International Conference on Miniaturized Systems for Chemistry and Life Sciences, MicroTAS 2013*. Chemical and Biological Microsystems Society, (2013).
- [5.14] LabVIEW System Design Software (online) <http://www.ni.com/labview/>
- [5.15] Bristow, Alan D., Nir Rotenberg, and Henry M. Van Driel. "Two-photon absorption and Kerr coefficients of silicon for 850–2200 nm." *Applied Physics Letters*, no. 19 (2007): 191104.

# Chapter 6: Optical Guided-Wave Sensing

6.1 Introduction

6.2 Optical Sensing Experiments

    6.2.1 Introduction

    6.2.2 Material & Method

    6.2.3 Evaluating aqueous flow rate stability in the system

*6.2.3.1 Results and Discussion*

    6.2.4 Reusability of the Sensor System

*6.2.4.1 Results and Discussion*

    6.2.5 Refractive index sensing

*6.2.5.1 Results and Discussion*

    6.2.6 Glucose Solution Sensing Array

*6.2.6.1 Results and Discussion*

    6.2.7 Protein BSA Sensing

*6.2.7.1 Results & Discussion*

6.3 Temperature dependence

6.4 Conclusion

References

## 6.1 Introduction

This chapter consists of a series of optical sensing experiments: including the determination of flow rate stability and device repeatability of the system; application of different chemical solutions that have different refractive index; the use of glucose solution on different cavity lengths; and BSA protein sensing. Finally, experiments on the system thermal response to temperature variations are presented and discussed. The chapter ends with conclusions from the work.

## 6.2 Optical Sensing Experiments

### 6.2.1 Introduction

As described previously, optical sensing techniques have been used because of their advantages over electro/electrical and mechanical systems. Optical sensors are immune to electromagnetic interference, and do not conduct electricity and are useful in many applications. One of the emerging areas for optical sensors application is the chemical and bio-sensing. The sensor system in this work is capable of detecting small volumes of analyte. In the following sub-section, a series of experiments have been undertaken to test the sensor system potential.

### 6.3.2 Material & Method

When waveguides with an internal photonic crystal cavity operate in an aqueous environment, the resonance wavelength detected in the output signal is affected by the analyte. This is because of the analyte that acts as the cladding layer of the waveguide and consequently modifies the effective index on the sensing area. This results in the shifting of the resonance wavelength peak when various effective indices are introduced.

One of the methods to detect changes in refractive index is to vary the

concentration in bulk solution of the analyte. In this work, different cavity lengths with different concentration of diluted glucose solutions were used to investigate the stability of the system, Q factor and sensitivity relationship. In addition, different known refractive index chemicals such Isopropyl alcohol (IPA) ( $n = 1.3738$ ) and Methanol ( $n = 1.3284$ ) have also been used. Lastly, to determine if the system is capable of sensing bulk biological elements, different concentration of proteins from bovine serum albumin (BSA) were introduced. The experiment setup was described earlier in section 5.4.1 in Chapter 5 and was presented again in Figure 6.1. The resonance wavelengths were detected in the output signal.

*Note: All analytes were stored in the same room as the sensor system 1 hour prior to the experiments were carried out. This is to remove the heat factors and to make sure the analyte and sensor system are at the same room temperature when experiments were carried out. The temperature of the experimental lab were set at  $T = 22^{\circ}\text{C}$ .*

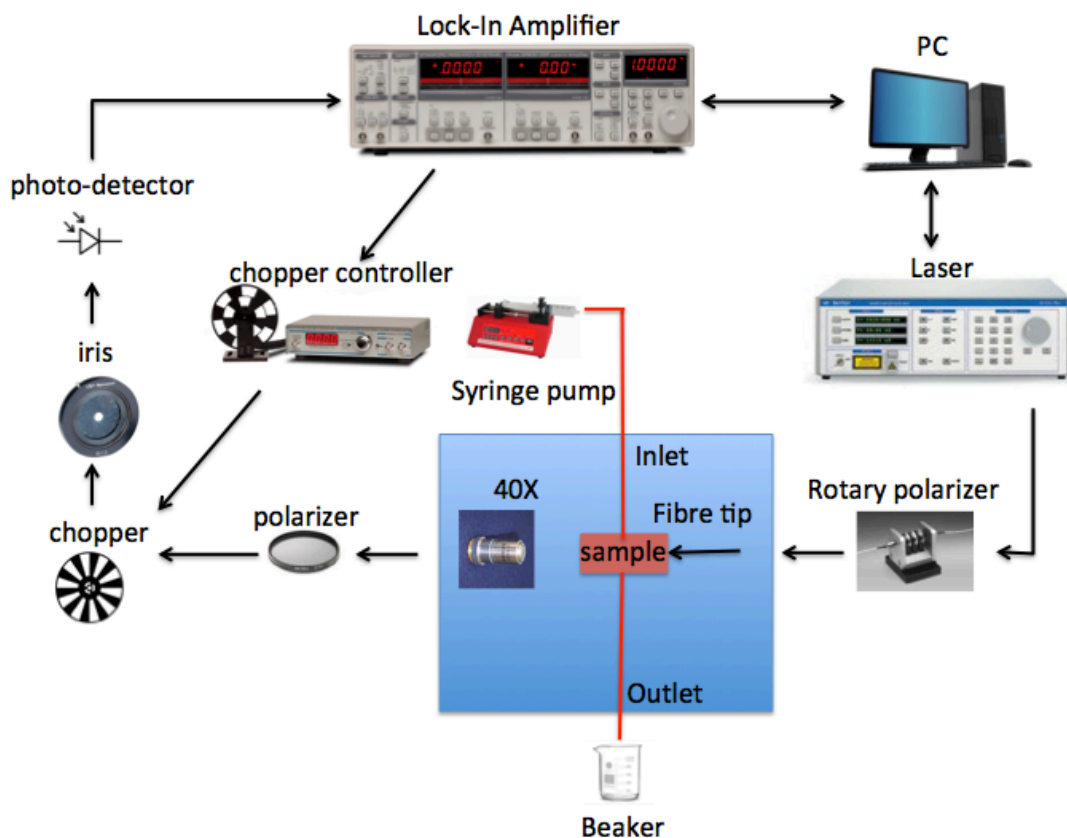


Figure 6.1: The sensor system setup arrangement for optical sensing experiments

### 6.3.3 Evaluating aqueous flow rate stability in the system

Initially, the acceptable flow rate of the analyte pumped into the system needs to be determined. This is to examine the stability of the system and the output signal during the analyte flowing through the device.

The experiment was set up as shown in Figure 6.1. De-ionised (DI) water was pumped into the device through the inlet and outlet of the microfluidic channel. The syringe pump was set to increase from  $5 \mu\text{l}/\text{min}$  (very low flow rate) to  $95 \mu\text{l}/\text{min}$  in each  $180 \text{ s}$  interval. The experiment is important to configure the system's stability and the resonance wavelengths' consistency during continuous analyte flow through the system. All experiments in this section were carried out using PhC microcavity devices consisting of two mirrors with the cavity length of  $470 \text{ nm}$ . The laser resolution during this experiment was set at  $2 \text{ pm}$  range.

#### 6.3.3.1 Results and Discussion

From the observation, during no flow of analyte through the sensor system, the resonance wavelength was detected at  $1545.61 \text{ nm}$ . This was set as the reference point of the experiment. The resonance wavelengths shifts from the reference point were taken and plotted into Figure 6.2.

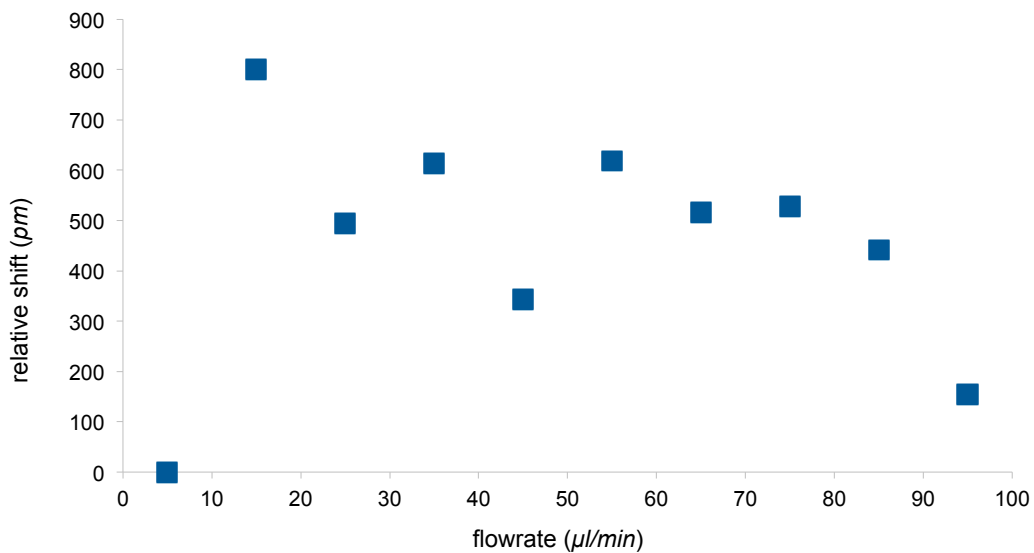


Figure 6.2: The resonance wavelengths shifts with different flow rates continuously flowing through the sensor system

The results indicated that the resonance wavelength was shifted in about 800  $\text{pm}$  between 5 and 15  $\mu\text{l}/\text{min}$  of flow rate. There are relatively small changes (of 150  $\text{pm}$ ) from 25 to 75  $\mu\text{l}/\text{min}$  of flow rate. The flow interval is sufficient due to the changes was seen in resonance wavelengths. The large shift was possibly due to the temperature difference between analyte and the sensor system. Finally, the resonance wavelengths are stable with only slight changes; meaning the temperature in the analyte and the sensor system were in equilibrium. When the local temperature of the sensor system is changed, the density of the DI water was also changed which slightly alters its refractive index. From Figure 6.2, small shifts around 150  $\text{nm}$  was seen between the flow rate of 25 and 75  $\mu\text{l}/\text{min}$ .

The continuous flow of DI water in the sensor system was stopped at 95  $\mu\text{l}/\text{min}$  due to analyte leaking from the channel inlet. The stability of the sensor system is compromised at a higher flow rates (95  $\mu\text{l}/\text{min}$ ). A possible solution is to have a larger channel to flow the analyte through the device. However, a larger channel may generate bubbles in the sensing area and lead to false readings. Nonetheless, the sensor system is able to withstand the continuous flow of the analyte at between 25 and 75  $\mu\text{l}/\text{min}$ . This indicates that the sensor system is suitable to be used to investigate its optical response for further experiments.

### 6.3.4 Reusability of the Sensor System

In general, the sensor system is cleaned thoroughly with DI water after each experiment when different analytes were to be used. As a preliminary step, to evaluate that the sensor system is capable to revert back to its original resonance wavelengths peaks, the different analytes were pumped continuously to observe the changes. The experiment also validates the ability of the sensor system to respond promptly to the changes in refractive index and analytes. In this experiment, the DI water and 5 % of glucose concentration solution were used to evaluate the system while the flow rate of the analyte was kept constant at  $25 \mu\text{l}/\text{min}$ .

#### 6.3.4.1 Results and Discussion

Continuous readings of resonance wavelengths were noted and then were plotted in Figure 6.3. From the observation, the initial DI water resonance wavelengths were noted at  $1545.61 \text{ nm}$ , and it was set as the reference point. At  $350 \text{ s}$  marks, the resonance wavelengths were shifted when the glucose concentrated solutions were pumped into the sensor system. The sensor system begins stabilised between  $700$  and  $800 \text{ s}$  marks and gives resonance wavelengths of  $1546.61 \text{ nm}$ . The stabilisation time of  $700 \text{ s}$  to  $850 \text{ s}$  is when couple of measurements were at the same resonance wavelength location, which is at  $1546.61 \text{ nm}$ . At  $850 \text{ s}$  marks, the sensor system was pumped with DI water rinsing and the resonance wavelengths were shifted and remain stable at  $1000 \text{ s}$  marks and give  $1545.58 \text{ nm}$ . The resonance wavelengths shifts are shown in Figure 6.4 (a) and (b). The slight decrease on the later DI water resonance wavelengths from the reference point is possibly due to the local temperature changes at the sensor area when introducing the different analyte.

The switching time of the sensor system was less than  $180 \text{ s}$ . Nonetheless; this is due to the syringe swap from glucose concentration solution to DI water and back and

the length of the delivery tube. This can be further improved by having two syringe pumps connected to a controllable valve. With this, the switching time can be decreased. Nevertheless, it is shown that the system is capable to investigate optical response in the flowing analyte through the microfluidic channel. In this experiment, the normal tapers of the PhC nanocavity waveguides were used. Hence, the strong oscillation of Fabry-Perot is observed during the measurement results.

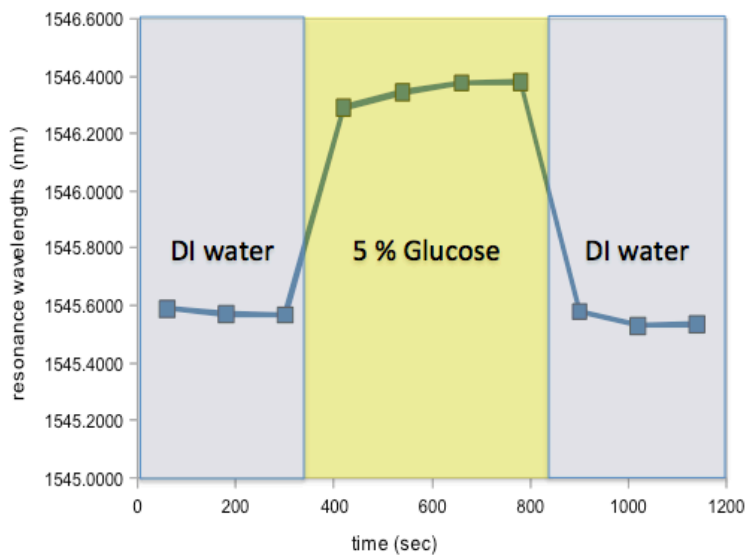


Figure 6.3: The resonance wavelengths peaks ( $nm$ ) according to the time ( $s$ ) at the continuous flow of DI water-Glucose concentration-DI water experiment.

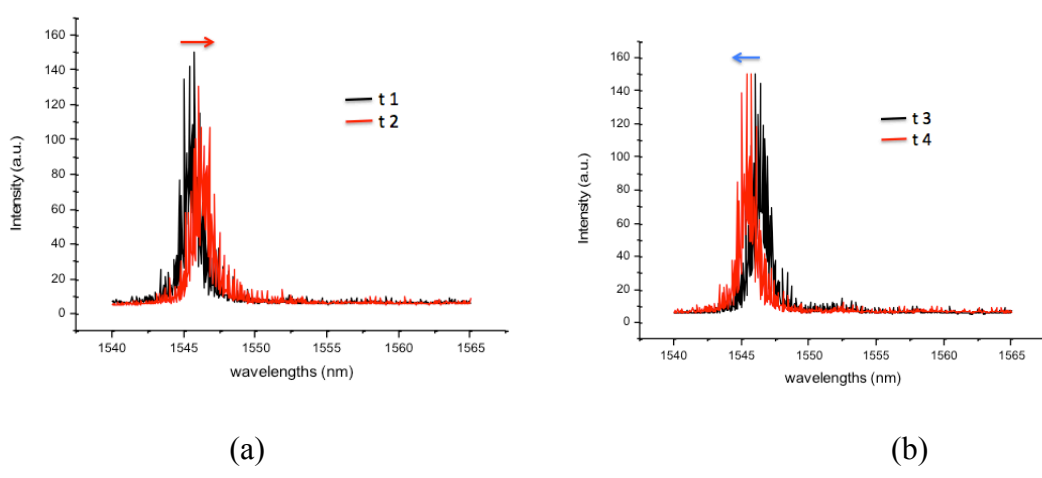


Figure 6.4: Spectral transmission of resonance wavelength shifts from (a) DI water to glucose concentration solution (red shifts) and from (b) Glucose concentration solution to DI water (blue shifts).

### 6.3.5 Refractive index sensing

Refractive index sensing is widely researched for vast number of applications [6.1-6.4]. This is due to the sensing methodology of providing the real-time results without the requirement of fluorescent labelling. Moreover, the preparation of the sample is easy and minimal.

In this experiment, the refractive indexes of the analytes were predetermined from literature [6.4]. In this case, the sensor system was tested on DI water ( $n = 1.333$ ), methanol ( $n = 1.3284$ ) and IPA ( $n = 1.3738$ ). It is noted that some of the solvents may swell the PDMS channel such as acetone [6.5]. Methanol and IPA were used as benchmarks to estimate the sensitivity,  $S$  ( $nmRIU^{-1}$ ) of the system.

$$S = \frac{\Delta\lambda}{\Delta n} \quad (\text{Eq. 6.1})$$

Where  $\Delta\lambda$  is relative resonance wavelengths and  $\Delta n$  is relative refractive index. Meanwhile, the detection limit,  $DL$  of the system was defined based on the ratio of spectral resolution,  $R$  ( $2 pm$ ) and the system sensitivity,  $S$  [6.6].

$$DL = \frac{R}{S} \quad (\text{Eq. 6.2})$$

While the Figure of Merit ( $FoM$ ) of the sensor was given by the ratio of system sensitivity,  $S$  and Full Wave Half Maximum (FWHM) of the resonance wavelengths.

$$FoM = \frac{S}{FWHM} \quad (\text{Eq. 6.3})$$

### 6.3.5.1 Results and Discussion

Firstly, the resonance wavelength of DI water was obtained at  $1546.87\text{ nm}$ . Then, the methanol was pumped through the microfluidic channel using different syringes. The experiment was also repeated by replacing methanol with IPA using the same parameters.

From the observation, when methanol and IPA were introduced, the resonance wavelengths peaks were measured at  $1546.2454\text{ nm}$  (blue shift) and  $1556.8952\text{ nm}$  (red shift) respectively. As a result, the resonance wavelength peaks shifted during methanol and IPA were achieved, from initial DI water is at  $0.6246$  to  $10.0252\text{ nm}$  correspondingly. Based on equation (6.1), the estimated sensitivity of the system for measurement of DI water to methanol is  $135.78\text{ nmRIU}^{-1}$  and between DI water and IPA is  $245.72\text{ nmRIU}^{-1}$ . In addition, the sensitivity of the system based on methanol and IPA measurement is  $234.58\text{ nmRIU}^{-1}$ . Meanwhile, the detection limit,  $DL$  for the sensor system is  $8 \times 10^{-6}\text{ RIU}$  and the  $FoM$  is 307.15.

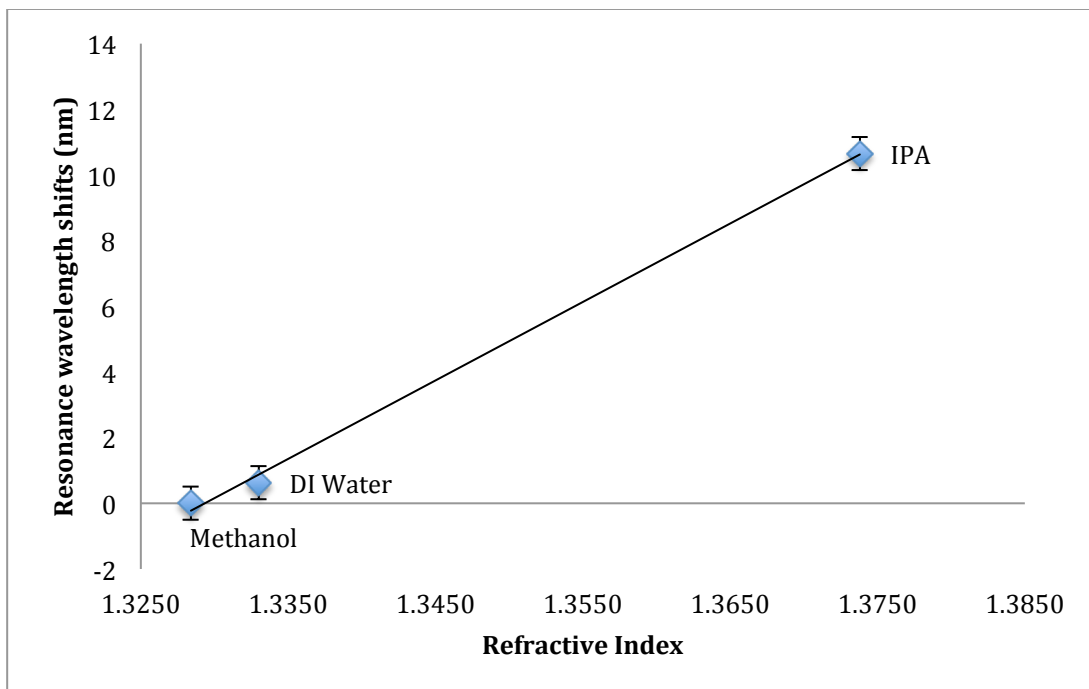


Figure 6.5: Resonance wavelength peak shifts of DI water, Methanol and IPA. Figure 6.5 depicted the difference refractive index solutions such Methanol, DI water and IPA were used for RI sensing. Different refractive indexes behave to different resonance shifts.

Based on the limited results, it was demonstrated that there was a close to linear relationship between the resonance wavelength shifts and the refractive index change of the analytes tested. Hence, it is noted that the 1D PhC nanocavity devices the potential to be used as basic building block of the optical RI sensor. Further enhancement of the sensor detection limit can be achieved by increasing the Q values of the devices, which improves the precision of the resonance wavelength measurements.

### 6.3.6 Glucose Concentration Sensing Array

One of the most common analyte used to investigate the optical sensor capabilities is glucose solution [6.7-6.9]. This is because glucose solution represents the basic characteristics of glucose in blood and it is particularly important in the care of diabetes mellitus. Therefore, to develop a sensor system that can detect small volume of glucose in blood is very demanding.

Nevertheless, in this series of experiments, various concentrations of glucose solutions (0, 10 and 15 % (*by weight*)) were used to study the relationship between the various cavity lengths ( $c = 450, 470, 490, 510 \text{ nm}$ ) and the Q factors. The resonance wavelengths for each cavity lengths with various glucose concentrations were measured. The sensor system was rinsed thoroughly with DI water immediately after each measurement was taken to remove any residual glucose solution.

#### 6.3.6.1 Results and Discussion

The results are summarised in Figure 6.6. From the observation, the resonance wavelengths for each cavity lengths that correspond to varying glucose concentrations are as expected and showed the resonance peaks moved to the longer wavelengths. The change in refractive index of the analytes cladding the sensing area immediately changed the effective index of the sensor system. Changes of the effective index influence further changes of the light phase velocity in the sensor.

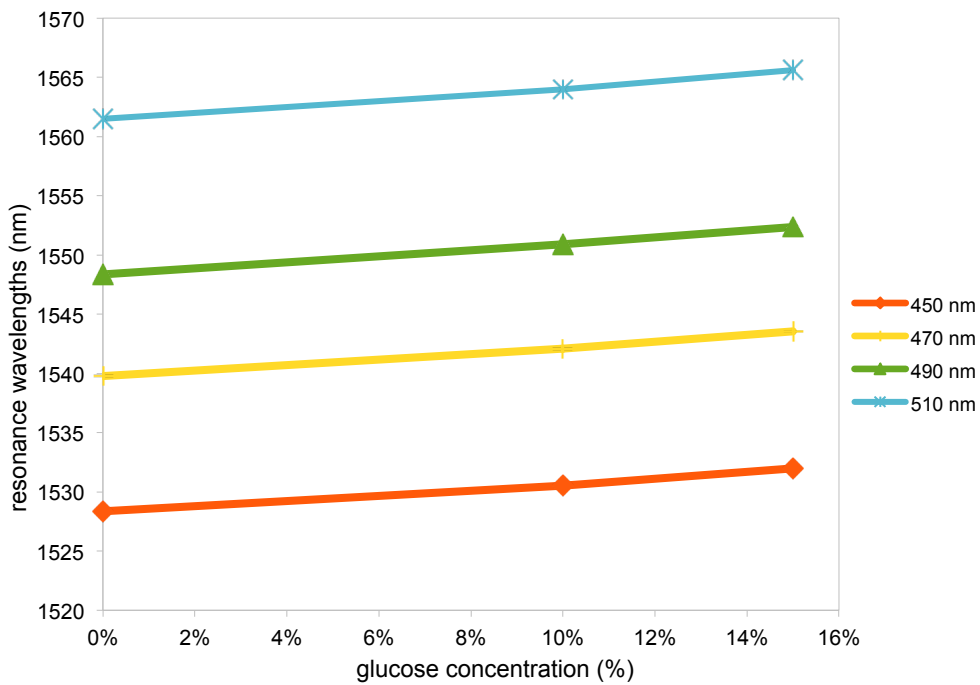


Figure 6.6: Resonance wavelengths of glucose concentration solution at 0, 10 and 15 % correspond with various cavity lengths,  $c$ .

A near linear relationship between the resonance wavelength shifts and all of the cavity lengths were observed with respect to the glucose concentration solutions (see Figure 6.6). However, the effects on the individual devices are different. On the measurement results from 0 to 10 % of the glucose concentration, the devices with the highest Q factor values ( $Q \sim 8000$  at  $c = 450\text{ nm}$ ) realised the least shift while both devices with lower Q factor values ( $Q \sim 500$  and  $600$  for  $c = 490$  and  $510\text{ nm}$  respectively) have the greatest shift. This is due to the cavity mode at this stage that are more sensitive to devices with the longer cavity length. This is shown in Figure 6.7. Moreover, this observation also occurred during the measurement of 10 to 15 % of glucose concentration, when the longer cavity lengths of  $510\text{ nm}$  experience the longest shift compared to the one with shorter cavity length and higher Q factor values. Nonetheless, the resonance wavelength shifts are similar (around  $1.5\text{ nm}$  shifts) for both high and low Q factor values devices ( $Q \sim 2000$  and  $900$  for  $c = 450$  and  $490\text{ nm}$ ). This is shown in Figure 6.8. This indicates that there is a “play off” between the cavity length and Q factor in determining the resonance shifts. Nonetheless, the effects of all resonance shifts are only a slight change from the lowest and highest shifts. This means that the longest and shortest shifts measured are around  $2.5$  and  $2\text{ nm}$  respectively for 0

to 10 % glucose concentration and around 1.6 and 1.4 nm for 10 to 15 % glucose concentration. Hence, this leads to the nearly linear effect on all of the various cavity length devices correspond to the glucose concentration level. Nevertheless, it is noted that the sensor system can be improve if the devices have an ultra high Q factor value features. It is also observed that the higher glucose concentrations have the tendency to reduce the Q factor values of all devices. This may be due to the Bragg mirrors were not working as effectively as before and the cavity mode was scattered hence resulting in the lower Q factor values in higher refractive index medium. The affect of Bragg mirrors were not working is due to the reduction in the mode confinement; hence the coupling strength of the mirrors was weakening.

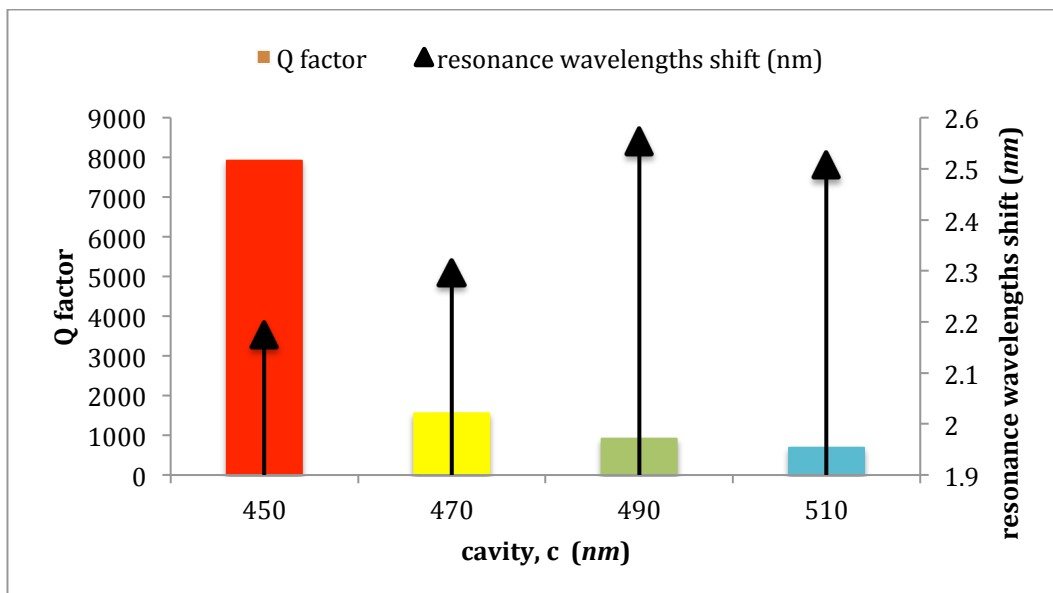


Figure 6.7: Q factor of 0 % of glucose concentration and resonance wavelengths shift from 0 to 10 % of glucose concentration solutions according to various cavity lengths,  $c$  (nm).

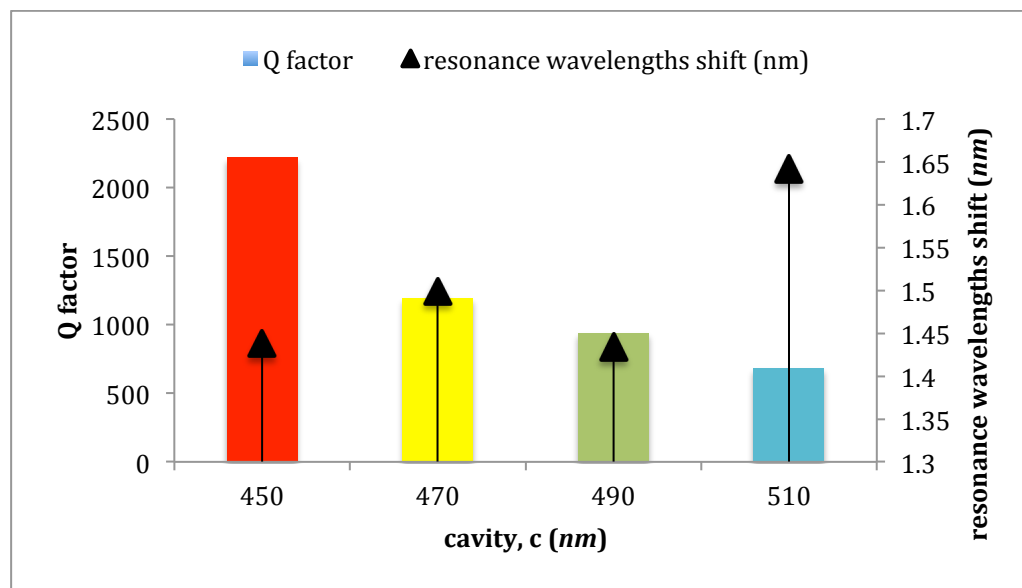


Figure 6.8: Q factor of 10 % of glucose concentration and resonance wavelengths shift from 10 to 15 % of glucose concentration solutions according to various cavity lengths,  $c$  (nm).

### 6.3.7 Protein BSA Sensing

Bovine Serum Albumin (BSA) is a serum protein derived from cows and often used as a standard in the protein detection in biochemical experiments [6.9 - 6.16]. In this work, BSA is chosen because of its stability, it possess intermediate molecular mass, and it is widely used as standard in determination of protein concentration.

Initially, DI water was pumped through the sensor system for 5 minutes for initial reading to mark as the baseline (0 % of protein BSA). Next, the diluted protein BSA concentrations ( $3.125, 6.25, 12.5$   $\mu\text{g/ml}$ ) were pumped for 10 minutes followed by a rinse with DI water again for 15 minutes respectively. This is to remove the analyte coverage area of approximate  $5.5 \text{ mm}^2$  (the size of the microfluidic channel openings). The PhC device specification chosen for this experiment is  $N = 2$  and  $c = 470 \text{ nm}$ .

*Acknowledgment:* The BSA concentration solutions were prepared by Dr Mohd. Faizal Ghazali from College of Medical, Veterinary and Life Sciences, University of Glasgow.

### 6.3.7.1 Results & Discussion

From the experiment performed, the list of measured resonance wavelengths correspond with each protein BSA dilutions were summarised in Figure 6.9. From the results obtained, it is shown that the sensor system are capable of detecting protein BSA as low as  $3.125 \mu\text{g/ml}$  with the resonance wavelength shifts of  $0.1857 \text{ nm}$ . For comparison, the results achieved are superior than the 2D PhC waveguide [6.12] that has a larger estimated sensing area ( $>100 \mu\text{m}^2$ ) and detected  $10 \mu\text{g/ml}$  with a resonance shift of  $0.2 \text{ nm}$ . The sensing area estimated for this work is  $2.35 \mu\text{m}^2$  (consideration include the complete tapering mirror holes inside the cavity). The sensor system is able to detect BSA concentration of  $6.25$  and  $12.5 \mu\text{g/ml}$  with resonance shifts of  $0.2867$  and  $0.6918 \text{ nm}$  respectively. Further comparison with other type of devices is listed in Table 6.1.

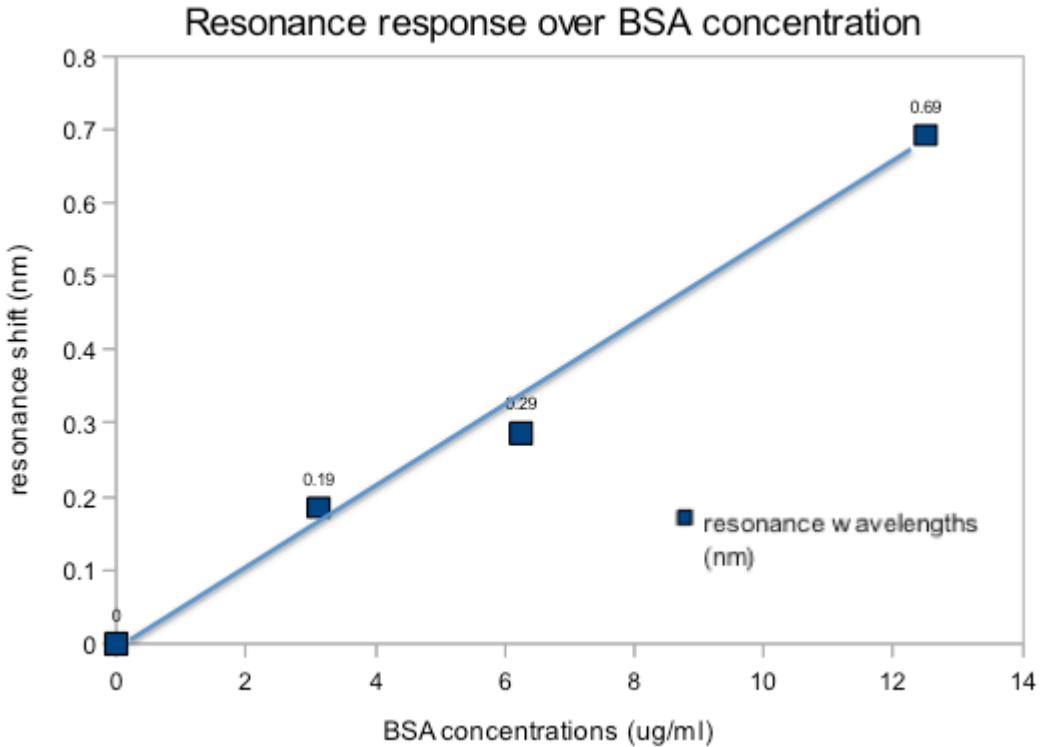


Figure 6.9: Resonance shift versus BSA concentrations

To evaluate the performance of the sensing system, literature review [6.13], suggests quoting the minimum concentration detectable. This is because the figure-of-merit used to estimate the sensing capabilities vary from concentration detected (in terms of *parts per billion*,  $\mu M$ , *particle/L*), the bound mass (in terms of  $pg$ ), or surface density (in terms of  $pg/mm^2$ ) and others. This would make the sensor difficult to assess and compare unless they uses the same merit.

Type of device [references]	Estimated sensing surface ( $\mu m^2$ )	Minimum concentration recorded	Resonance shift, $\Delta\lambda$ recorded (nm)
Slot ring resonator [6.14]	>250	0.042 $\mu g/ml$	2.5 (for 10 $\mu g/ml$ )
Slot ring resonator [6.15]	21.84	17 $\mu g/ml$	0.1
2D PhC waveguides [6.12]	>100	10 $\mu g/ml$	0.2
2D PhC waveguides [6.16]	8.15	< 1 $\mu M$	-
2D PhC waveguides [6.11]	50	2 %	1.7
1D PhC nano cavity [our device]	2.35	3.125 $\mu g/ml$	0.2

Table 6.1: Comparison with other type of devices for BSA protein detection.

### 6.3 Temperature dependence

The silicon material has a thermo-optic coefficient ( $\Delta n / \Delta T$ ) of  $1.87 \times 10^{-4} K^{-1}$  at  $295 K$  ( $22 ^\circ C$ ) in the range of  $1500 nm$  [6.17]. An increase of the temperature,  $\Delta T$  will gives the thermo-optic effect to the original refractive index,  $n$  by the amount of  $\Delta n$ .

$$n' = n + \Delta n \quad (\text{Eq. 6.2})$$

Where  $n'$  is the new refractive index. The changes in refractive index have an effect on the transmission spectrum, which leads to the shift in resonance wavelength peaks.

$$\frac{\Delta\lambda}{\Delta T} = \frac{\lambda_0}{n_{eff}} \frac{\Delta n}{\Delta T}$$

(Eq. 6.3)

To investigate the effect on silicon-based sensor, temperature dependant experiments were carried out. DI water was used as the analyte because water generally has very high specific heat capacity. In order to determine localised effect on the sensor system, various temperatures of the DI water were taken into consideration, from low ( $8^{\circ}\text{C}$ ), room temperature ( $22^{\circ}\text{C}$ ) and high ( $35^{\circ}\text{C}$ ).

Firstly, the resonance wavelengths of the DI water at room temperature were obtained as the reference. It is noted that the thermo-optic response of the resonance wavelengths has a blue (shorter) shift and red (longer) shift for low and high temperature respectively [6.18]. Subsequently, the sensor system was pumped with the low temperature of DI water. The resonance wavelengths of the devices were measured continuously to detect the thermal response of the sensor over the period of 1 hour. Next, the room temperature DI water was pumped again for 1 hour. This is to make sure the state of the sensor system is back at room temperature. Then, the high temperature of DI water was pumped into the sensor system. The resonance wavelengths were obtained continuously for another 1 hour. The shortest and the longest resonance wavelengths for low and high temperature response respectively were taken.

### 6.3.1 Results and Discussion

The results obtained from the experiment are summarised in Figure 6.15. From the observation, the resonance wavelengths for low and high temperature DI water were shifted to shorter and longer wavelengths respectively as expected. This is due to the thermo-optic effect that has direct consequence to the effective index of the sensor system. The thermal response graph profile shown curve at the end was possibly due to the heat dissipation on the PTFE tubing. It is also possible that the local heating from

the DI water was not completely replicated at the sensor system. From here, temperature coefficient for the sensor system is calculated by  $(\Delta\lambda / \Delta T) = 0.398 \text{ nm } ^\circ\text{C}^{-1}$ . It is noted that the temperature of the surrounding sensor system has an effect on the results. Hence, thermal factors need to be considered to ensure stability during the course of the experiment.

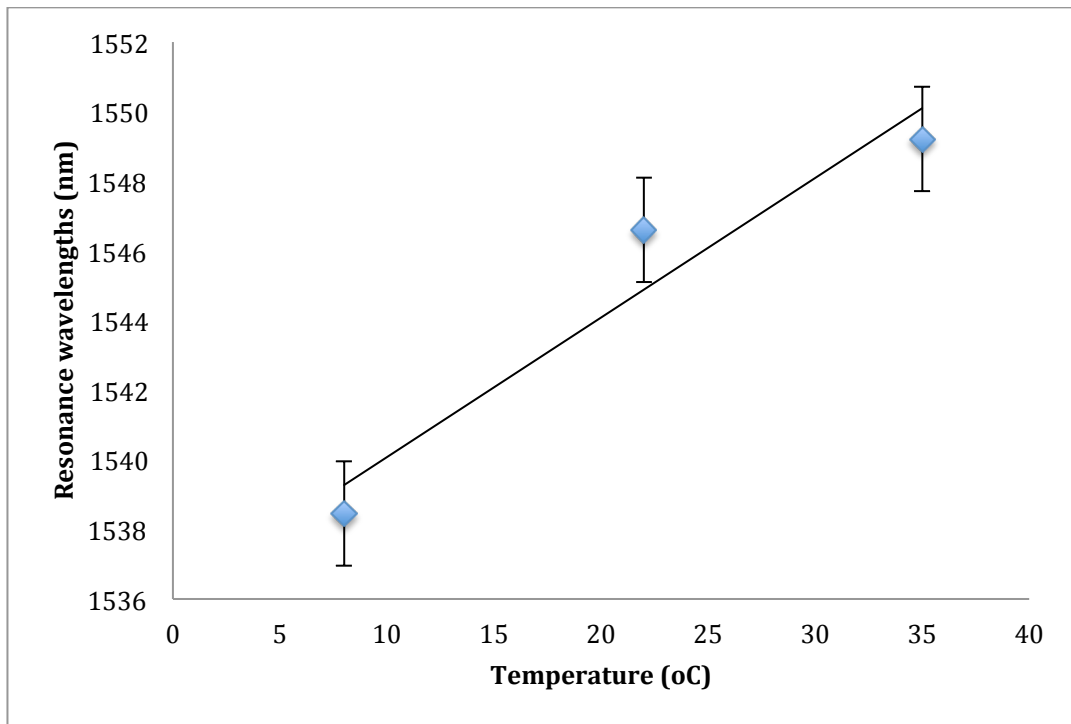


Figure 6.10: Resonance wavelengths response with different temperature medium.

Temperature (°C)	Resonance wavelengths (nm)
8	1538.45
22	1546.60
35	1549.21

Table 6.2: Absolute measurement data of resonance wavelengths correspond to different temperature medium.

## 6.4 Conclusions

In summary, we have tested the sensor system with several experiments that covered the aspects of stability, repeatability of the sensor, refractive sensing using methanol, DI water and IPA. The device relationship between Q and sensitivity using the diluted glucose solutions, BSA protein bulk sensing and temperature effect on the sensor system has also been measured. As most of the experiments carried out are made with materials of different refractive indices, it is crucial to understand that the sensor system is operates with changes in the resonance wavelength peaks. Higher refractive index analytes produce red shift and the lower refractive index analyte produced blue shift. Devices with different cavity lengths have similar sensitivity for various Q factors; however, the sensing system can be improved if the devices have an ultra high Q factor. It is noted that there is a play off between cavity lengths and the Q factor values. Longer cavity lengths may have the advantage of a larger sensing surface, while higher Q factors, in shorter cavities, allows interaction with the analyte as the light makes multiple passes of the cavity. The sensor system is also capable of bio-molecular sensing of non-specific species. The sensor system showed the ability to detect low concentrations of the protein BSA. Finally, in order to inspect the thermal response, the sensor system was locally heated using DI water at various temperatures. It is noted that in the course of the experiments, the thermal effect needs to be carefully considered. Both, the sensor system and the analyte need to be in the same temperature in order to eliminate the thermal transient effects.

## References

- [6.1] Shen, Yang, Jianhua Zhou, Tianran Liu, Yuting Tao, Ruibin Jiang, Mingxuan Liu, Guohui Xiao et al. "Plasmonic gold mushroom arrays with refractive index sensing figures of merit approaching the theoretical limit." *Nature Communications* 4 (2013).
- [6.2] Jágerská, Jana, Hua Zhang, Zhaolu Diao, Nicolas Le Thomas, and Romuald Houdré. "Refractive index sensing with an air-slot photonic crystal nanocavity." *Optics Letters* 35, no. 15 (2010): 2523-2525.
- [6.3] Wu, Di, Tao Zhu, Ming Deng, De-Wen Duan, Lei-Lei Shi, Jun Yao, and Yun-Jiang Rao. "Refractive index sensing based on Mach-Zehnder interferometer formed by three cascaded single-mode fiber tapers." *Applied Optics* 50, no. 11 (2011): 1548-1553.
- [6.4] Moutzouris, Konstantinos, Myrtia Papamichael, Sokratis C. Betsis, Ilias Stavrakas, George Hloupis, and Dimos Triantis. "Refractive, dispersive and thermo-optic properties of twelve organic solvents in the visible and near-infrared." *Applied Physics B* 116, no. 3 (2014): 617-622.
- [6.5] Mukhopadhyay, Rajendrani. "When PDMS isn't the best." *Analytical Chemistry* 79, no. 9 (2007): 3248-3253.
- [6.6] White, Ian M., and Xudong Fan. "On the performance quantification of resonant refractive index sensors." *Optics Express* 16, no. 2 (2008): 1020-1028.
- [6.7] Oliver, N. S., C. Toumazou, A. E. G. Cass, and D. G. Johnston. "Glucose sensors: a review of current and emerging technology." *Diabetic Medicine* 26, no. 3 (2009): 197-210.
- [6.8] Liu, Y., P. Hering, and M. O. Scully. "An integrated optical sensor for measuring glucose concentration." *Applied Physics B* 54, no. 1 (1992): 18-23.

- 
- [6.9] Al-Ali, Ammar, Mohamed K. Diab, Arun Panch, Yassir Abdul-Hafiz, and William Jack MacNeish III. "Multiple wavelength optical sensor." U.S. Patent 8,781,544, issued July 15, (2014).
- [6.10] Vollmer, Frank, D. Braun, A. Libchaber, M. Khoshima, I. Teraoka, and S. Arnold. "Protein detection by optical shift of a resonant microcavity." *Applied Physics Letters* 80, no. 21 (2002): 4057-4059.
- [6.11] Lee, Mindy R., and Philippe M. Fauchet. "Two-dimensional silicon photonic crystal based biosensing platform for protein detection." *Optics Express* 15, no. 8 (2007): 4530-4535.
- [6.12] Skivesen, Nina, Amølie Têtu, Martin Kristensen, Jørgen Kjems, Lars H. Frandsen, and Peter I. Borel. "Photonic-crystal waveguide biosensor." *Optics Express* 15, no. 6 (2007): 3169-3176.
- [6.13] Scullion, Mark G., Thomas F. Krauss, and Andrea Di Falco. "Slotted photonic crystal sensors." *Sensors* 13, no. 3 (2013): 3675-3710.
- [6.14] Barrios, Carlos A., Kristinn B. Gylfason, Benito Sánchez, Amadeu Griol, Hans Sohlström, Miquel Holgado, and Raphael Casquel. "Slot-waveguide biochemical sensor." *Optics Letters* 32, no. 21 (2007): 3080-3082.
- [6.15] De Vos, Katrien, Peter Debackere, Tom Claes, Jordi Girones, Wout De Cort, Etienne Schacht, Roel G. Baets, and Peter Bienstman. "Label-free biosensors on silicon-on-insulator optical chips." *SPIE NanoScience+ Engineering*, pp. 739710-739710. International Society for Optics and Photonics, (2009).
- [6.16] Dorfner, D., Zabel, T., Hürlimann, T., Hauke, N., Frandsen, L., Rant, U., Abstreiter, G. and Finley, J.. Photonic crystal nanostructures for optical biosensing applications. *Biosensors and Bioelectronics*, 24(12), pp.3688-3692 (2009).
- [6.17] Frey, Bradley J., Douglas B. Leviton, and Timothy J. Madison. "Temperature-

dependent refractive index of silicon and germanium." In *SPIE Astronomical Telescopes+ Instrumentation*, pp. 62732J-62732J. International Society for Optics and Photonics, (2006).

- [6.18] Chong, Harold MH, and Richard M. De La Rue. "Tuning of photonic crystal waveguide microcavity by thermo-optic effect." *Photonics Technology Letters, IEEE* 16, no. 6 (2004): 1528-1530.

## **Chapter 7: Conclusion and Future Work**

- 7.1 Introduction
- 7.2 Summary and Conclusion
- 7.3 Future Work
- References

## 7.1 Introduction

This chapter covers the summary of the development of 1D PhC nanocavities and the results derived from optimisation and application of this sensor. In the end, the conclusions are drawn to describe the aim and objectives of this work. Finally, some potential future works for further improvement and impending effort for continuation of this research project are discussed.

## 7.2 Summary and Conclusion

In general, the main objectives of this work were to design, fabricate, characterise and utilise the 1D PhC nanocavities for optical sensor has been achieved. The sensor system were realised and investigated based upon the experimental work using 1D PhC nanocavity devices.

In Chapter 1, a general overview of the photonic devices pertaining to optical sensor technology has been described. This provides the background information relating to basic building block of current transducers of the optical sensing system. Moreover, the concept of PhC has also been reviewed to provide an insight of its potential as an optical sensor.

Chapter 2 begins with an overview of the method to model the photonic devices via solving the Maxwell's Equations on electric and magnetic field, particularly FDTD computation technique using Yee algorithm configurations. This leads to the introduction of commercial software, Lumerical FDTD. Key elements of the modelling the photonic devices have been discussed including the sources and boundary conditions. Conformal mesh techniques enhanced the FDTD calculations accuracy near the structural boundary. Furthermore, the method of extracting Q factor by the slope of decaying mode envelope was reviewed. Finally, the chapter reviewed the 2D and 3D FDTD modelling of 1D PhC nanocavities prior to the fabrication process. The

modelling has been used to gain an overview of the device behaviour.

Chapter 3 reviewed the device fabrication process based on the SOI substrate using the facilities in the JWNC. The optimisation on EBL and dry etching techniques increase the reliability and reproducibility of the devices. The steps of the fabrication process are listed in a sequential manner. In addition, the waveguide coupling of adiabatically tapered waveguides and inverted tapers with block polymer of SU-8 are discussed. The SU-8 block polymer is of lower index than silicon and this coupling method is preferable, as indicated by lower Fabry-Perot oscillations on the measurement data.

In Chapter 4, the design of 1D PhC nanocavity devices is reviewed. The design is discussed in terms of the period, cavity and mode matching. The enhancement of the Q factor can be achieved by tapering mirror holes inside the cavity to reduce the scattering losses. Meanwhile, the outside tapering mirror holes provide smooth transition mode from the unpattern waveguide to the Bragg mirrors. However, transmission becomes critical because the losses correspond to the mode profile mismatch at the taper sections. The Q factor of the devices can be increased by the number of period; nevertheless, it is saturates at 4-5 mirrors.

Chapter 5 starts with an overview of optical sensing system. The sensing system incorporates the microfluidic channel and the transducer devices. This chapter covers the design and the fabrication of PDMS microfluidic channel system. The straight channel system flowing on top of the waveguide devices was adapted to the sensing system. This chapter also reviews the characterisation of the 1D PhC nanocavity devices and overall sensor system that covers the spectral range at  $1550\text{ nm}$ . It is important to understand the optical responses of the transmission spectrum prior to performing the experiments.

In Chapter 6, several experiments were carried out to investigate the sensor performance. The sensitivity of various Q factors that corresponds to the different cavity lengths were studied. It is noted that there is a play off between cavity lengths and the Q factors. Longer cavity lengths may have the advantage of a larger sensing surface, while higher Q factors, in shorter cavities, allows interaction with the analyte as the light

makes multiple passes of the cavity. The sensor system sensitivity,  $S$  was measured via refractive index sensing experiment varying from  $135.78$  to  $245.72 \text{ nmRIU}^{-1}$  with the detection limit,  $DL$  of  $8 \times 10^{-6} \text{ RIU}$ . The sensing area estimated is  $2.35 \mu\text{m}^2$ . Moreover, through the non-specific interaction experiment, bio-molecular proteins BSA protein as low as  $3.125 \mu\text{g/ml}$  concentrations was detected. Finally, the sensor system thermal responses were measured. Better environmental control should be imposed in the future.

## 7.3 Future Work

The motivation to wholly replace the electronic devise with photonic devices is still unclear. Although the development of photonic community have flourished tremendously over the years in many areas, however, the question still lies in to what extent the photonic devices can form an inherent part of the current technology. The replacement would mean there would be a transition period where electronic and photonic devices are embedded in the same apparatus. Integrated optics such as PhC nanocavity based sensors are capable of label-free optical sensors operating as a lab-on-chip. The PhC nanocavity chip is very small; hence the devices can be discarded after each use similar to Genelyte system [7.1]. The cost can be reduced because the devices uses silicon based technology. In this thesis, the work was initiated with modelling the devices via 2D and 3D FDTD computations prior to the fabrication process. It can be further improved by taking the advantage of the embedded code/script features in Lumerical software for multiple resonance wavelengths and Q factor values extraction in a single simulation. Hence, better understanding of the hole tapering technique can be realized in order to reduce the mode profile mismatch. There is also the opportunity to run more modelling via parallel computing. The silicon fabrication has been established for more than a decade. Nonetheless, the fabrication techniques are still improving to provide robustness and reliability of the end results. In this work, the sidewalls of the waveguides roughness can be improved to reduce the scattering losses and have better light propagation. This can be done by the refinement of dry etching techniques and the use of higher contrast resist. The latest trend is for slotted waveguide structures [7.2-7.3] to boost with ultra-high Q factor values and sensitivity. This certainly is beneficial to small optical sensor since it has larger sensing area coverage and temporally

overlapped time with analyte due to the PhC effects.

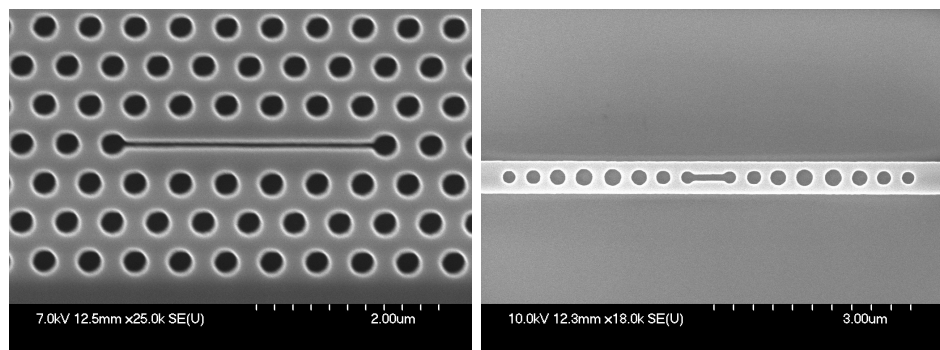


Figure 7.1: Fabricated slotted 2D (left) and 1D (right) PhC nanocavities.

The sensor system set up currently is connected to one syringe pump for analyte transportation. Multiple syringe pumps can be useful to facilitate the experiment by connecting them to the controllable valve/s. Analyte mixing is convenient to further explore the sensor capabilities in biological elements detection. Functionalised devices are accessible to carry out specific interaction binding experiment such as Avidin [7.3], Biotin [7.4] or DNA [7.5] detection. In addition, by preparing the surface treatment with thin layer of hydrophilic poly (ethylene glycol) (PEG) [7.6], both the nonspecific and specific interaction binding can be improved.

## References

- [7.1] Genalyte [online] <http://www.genalyte.com/>
- [7.2] Li, Tingyu, Dingshan Gao, Daming Zhang, and Eric Cassan. "High-and High-Sensitivity One-Dimensional Photonic Crystal Slot Nanobeam Cavity Sensors." *IEEE Photonics Technology Letters* 28, no. 6 (2016): 689-692.
- [7.3] Scullion, M. G., A. Di Falco, and T. F. Krauss. "Slotted photonic crystal cavities with integrated microfluidics for biosensing applications." *Biosensors and Bioelectronics* 27, no. 1 (2011): 101-105.
- [7.4] Zlatanovic, Sanja, Laura W. Mirkarimi, Mihail M. Sigalas, Maggie A. Bynum, Edmond Chow, Karla M. Robotti, Geoffrey W. Burr, Sadik Esener, and Annette Grot. "Photonic crystal microcavity sensor for ultracompact monitoring of reaction kinetics and protein concentration." *Sensors and Actuators B: Chemical* 141, no. 1 (2009): 13-19.
- [7.5] Toccafondo, V., J. García-Rupérez, M. J. Bañuls, A. Griol, J. G. Castelló, S. Peransi-Llopis, and A. Maquieira. "Single-strand DNA detection using a planar photonic-crystal-waveguide-based sensor." *Optics Letters* 35, no. 21 (2010): 3673-3675.
- [7.6] De Vos, Katrien, Peter Debackere, Tom Claes, Jordi Girones, Wout De Cort, Etienne Schacht, Roel G. Baets, and Peter Bienstman. "Label-free biosensors on silicon-on-insulator optical chips." In *SPIE NanoScience+ Engineering*, pp. 739710-739710. International Society for Optics and Photonics, (2009).

## Appendix A

### FDTD Calculation based on Yee mesh cell

The following six scalar (x,y and z) of partial differential equations are derived from Maxwell's equation to form the basic of FDTD calculation;

$$\frac{\partial H_x}{\partial t} = \frac{1}{\mu} \left[ \frac{\partial E_y}{\partial z} - \frac{\partial E_z}{\partial y} - (M \text{ source } x + \sigma * H_x) \right] \quad (\text{Eq. 2.5})$$

$$\frac{\partial H_y}{\partial t} = \frac{1}{\mu} \left[ \frac{\partial E_y}{\partial x} - \frac{\partial E_x}{\partial z} - (M \text{ source } y + \sigma * H_y) \right] \quad (\text{Eq. 2.6})$$

$$\frac{\partial H_z}{\partial t} = \frac{1}{\mu} \left[ \frac{\partial E_x}{\partial y} - \frac{\partial E_y}{\partial x} - (M \text{ source } z + \sigma * H_z) \right] \quad (\text{Eq. 2.7})$$

$$\frac{\partial E_x}{\partial t} = \frac{1}{\epsilon} \left[ \frac{\partial H_z}{\partial y} - \frac{\partial H_y}{\partial z} - (J \text{ source } x + \sigma E_x) \right] \quad (\text{Eq. 2.8})$$

$$\frac{\partial E_y}{\partial t} = \frac{1}{\epsilon} \left[ \frac{\partial H_x}{\partial z} - \frac{\partial H_z}{\partial x} - (J \text{ source } y + \sigma E_y) \right] \quad (\text{Eq. 2.9})$$

$$\frac{\partial E_z}{\partial t} = \frac{1}{\epsilon} \left[ \frac{\partial H_y}{\partial x} - \frac{\partial H_x}{\partial y} - (J \text{ source } z + \sigma E_z) \right] \quad (\text{Eq. 2.10})$$

Where  $\sigma$  and  $\sigma^*$  are electric conductivity (*siemens/m*) and total magnetic loss (*ohms/m*)